USE OF RHEO-NMR T_2 RELAXATION TIMES TO ESTIMATE TEMPERATURES IN A STANDARD NEWTONIAN OIL UNDER SHEAR FLOW

by

Yijin Su

Submitted in partial fulfilment of the requirements

for the degree of Master of Applied Science

at

Dalhousie University

Halifax, Nova Scotia

March 2018

TABLE OF CONTENTS

LIST OF TABLES

LIST OF FIGURES

ABSTRACT

Viscous heating is significant in materials processed at high shear rates. The objectives of this thesis were to a) determine how the NMR relaxation time T_2 of a Newtonian standard changes with temperature; b) use the T_2 measured under shear to estimate the temperature; and c) compare these estimates to those from a thermo-rheometric model (TRM). Experiments under static conditions in a Rheo-NMR mini-Couette system provided data successfully used to develop a function for the increase of T_2 with temperature. Rheo-NMR T_2 measurements were then conducted under shear rates from 2 to 1200 s^{-1}. The function between temperature and T_2 was applied to predict the temperatures under shear. The estimated temperatures increased at high shear rates but not at low shear rates, as estimated by the TRM. At high shear rates, the magnitudes of the temperatures estimated from both methods diverged, showing that the methods require further refinement.

LIST OF ABBREVIATIONS AND SYMBOLS USED

CPMG	Carr-Purcell-Meiboom-Gill
CWFP	continuous wave free precision
FT	Fourier Transforms
FID	free induction decay
FOT	fiber optic temperature sensor
MRI	magnetic resonance imaging
NMR	nuclear magnetic resonance
PFG	pulsed field gradient
RF	radio frequency
SF	solid fraction
TD-NMR	time domain nuclear magnetic resonance
TRM	thermo-rheometric model
XRD	x-ray Diffraction
A_o	the heat transfer area between the sample and the wall
A_{ig}	the heat transfer area between the wall and the Galden
A2/(A2+A1)	the ratio between Ampl_1 and the sum of Ampl_1 and Ampl_2
A_s	the effective shaft-fluid contact area
B_0	external magnetic field
B_1	oscillating magnetic field
C_p	specific heat of the sample
C_{pg}	the specific heat of the Galden
M_0	equilibrium magnetization

M_z	the longitudinal magnetization
M_{xy}	the transverse magnetization
N_{Br}	non-dimensional Brinkmann number
P_w	the power delivered to the sample
T	local dimensional temperature
T_0	reference temperature
T_{wo}	the temperature of the sample at the wall
T_{wg}	the temperature of the Galden at the inner wall
T_{gi}/Ti	the inlet temperature of the Galden
T_{go}/To	the outlet temperature of the Galden
T_{iso}	the sample temperature from the isothermal measurement
Tm	the sample temperature from the model measurement
T_{thm}	the temperature from the thermometer
T_{thmi}	the temperature from the thermistor
T_s	the temperature of the sample
$\overline{T}_g$	the bulk temperature of the Galden
T_{shaft_in}	the sample temperature predicted from the shaft-in experimental model
T_{shaft_out}	the sample temperature predicted from the shaft-out experimental model
T_s'	the sample temperature estimated only from the correlations
T_1	spin-lattice relaxation time
T_2	spin-spin relaxation time
T_{2_1}	the relaxation times of component 1
T_{2_2}	the relaxation times of component 2

W_{T2_1}	the weight of T_{2_1}
W_{T2_2}	the weight of T_{2_2}
W_A	the weight of A2/(A2+A1)
ν	resonance/rotational frequency
ω	Larmor frequency
h	Planck's constant
τ	a time constant
k	thermal conductivity of the sample
k_0	thermal conductivity at the reference temperature
$\dot{\gamma}$	local shear rate
$\dot{\gamma}_n$	non-dimensional shear rate
$\dot{q}_\nu$	local heat produced per unit volume
r_i/r_s	radius of the inner rotating cylinder or shaft
r_o	radius of the outer static cylinder
u	non-dimensional velocity
$\dot{u}$	derivative of the non-dimensional velocity
$\ddot{u}$	second derivative of the non-dimensional velocity
ρ	density of the sample
η	viscosity of the sample or the local viscosity
η_0	viscosity at the reference temperature
τ_s	torque at the shaft or the measured torque
$\dot{\omega}$	angular velocity

κ	characteristic geometric ratio
x	non-dimensional radial position
θ	non-dimensional temperature or angular position in the cell
$\dot{\theta}$	derivative of the non-dimensional temperature
$\ddot{\theta}$	second derivative of the non-dimensional temperature
σ	the shear stress
$\dot{q}$	the heat transferred between the sample and the wall
k_x	the thermal conductivity of the wall
r_{ig}	the radius of the Galden tube outside the static cylinder
h_g	the heat transfer coefficient of the Galden
$\dot{m}_g$	the mass flow rate of the Galden
$\dot{q}_{env}$	the heat gained from the environment
$a_m/b_m/c_m$	the viscosity parameters of the Andrade equation of the standard oil
c_L	length cylinder part
α	the angle of the cone part of the shaft
rps	revolutions per second
a_r	the ratio between Ampl_1 and the sum of Ampl_1 and Ampl_2
$\bar{\theta}$	the average non-dimensional temperature

ACKNOWLEDGEMENTS

I would like to express my thanks of gratitude to various people who have been journeyed me in recent years as I have worked on this thesis. Firstly, I would like to gratefully acknowledge my supervisor Dr. Gianfranco Mazzanti as well as my advisory team Dr. Amyl Ghanem and Dr. James Rioux, for their guidance, encouragement, suggestion, and very constructive criticism. Secondly, I want to thank my research colleagues and friends, Tianguang Jia, Omar ALQatami, Yujing Wang, Wei Xia, Yannan Huang, and Ya Li, who have been a constant source of joy through the struggles and trials of this thesis. I am also grateful to Ray Dube for the assistance of experimental setup and Dr. Fan Wang (University of Guelph) for all the related work she has done.

Special thanks to my parents and boyfriend, who support me a lot in the completion of this thesis and always stand by my side. Words cannot express how much I love you all.

My appreciation also goes to other friends for their kindness and generous support. One page is not enough to name you all.

CHAPTER 1 INTRODUCTION

With the development of modern materials science, researchers have never lost their interest in finding the relationship between the details of molecular organization and dynamics and the mechanical properties of complex fluids. Complex fluids include liquid crystals, gels, emulsions, particulate solid suspensions, and so on. All of them are related to materials in many fields, such as petrochemical engineering and food technology. To analyze the mechanics of complex fluids, a benchtop rheometer is utilized as the basic device, where the strain is measured under controlled stress conditions and vice versa. Different geometries, such as cone-and-plate, parallel plates, and concentric cylindrical Couette cells are usually employed to contain samples of the materials tested. These geometries are attached to the driving-sensing device.

To find the relationship between complex fluid rheology and the microscopic structure or dynamics, recent studies have explored various new experimental approaches in which both rheological and spectroscopic methods are utilized. For example, Rheo-NMR and Rheo-XRD have been set up to study the crystallization process of triglyceride blends (Mazzanti and Mudge 2008, Mazzanti, Mudge et al. 2008, Mudge and Mazzanti 2009).

The concentric cylindrical Couette cell, in which the fluid is kept in the annulus between two cylinders, is commonly employed to study the rheology of the fluids. A cylindrical Couette flow is easily achieved by rotating the inner cylinder and retaining the outer one fixed.

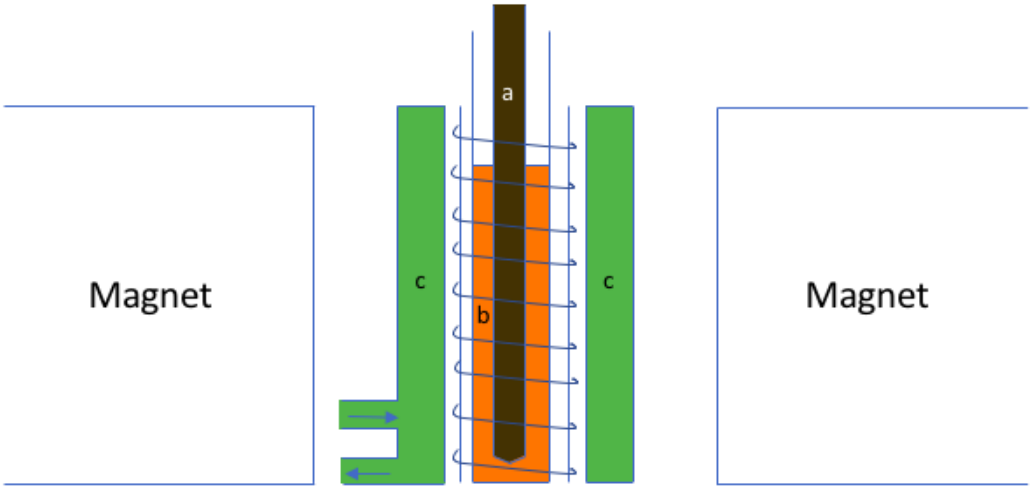

Figure 1 - 1 Conceptual sketch of the combined device to conduct simultaneous rheological and NMR measurements on a fluid under shear flow. A mini-Couette cell, driven by a rheometer, is inserted into a temperature-controlled environment between the poles of an NMR magnet. A coil, tuned to 20 MHz (radiofrequency range) sequentially excites and senses the protons magnetic behavior. a is the rheometer shaft, b is the fluid being tested, and c is the thermal control unit.

However, the shearing of a fluid always produces heat, due to viscous dissipation of energy. This viscous heating can be negligible for fluids with low viscosity or for very low shear rates, if a good thermal control unit is used to contain the sample of the material. However, at high shear rates, the viscous generated heat needs a large temperature gradient in order to be removed. This ends up creating a temperature in the sample that is larger than the temperature specified for the control unit.

This work is the first step of a new approach to estimate the temperature of complex fluids under shear, in the narrow gap of our Rheo-NMR cell. We usually study time changing suspensions such as crystallizing paraffin wax or triglyceride blends. The sample temperature, raised above that of the cooling fluid due to viscous heat, is not known. Since the spin-spin relaxation time T_2, measured in NMR experiments on liquids, is affected by temperature, it was proposed as a candidate to estimate the actual temperature of the

material. Experiments to quantify the effect of temperature on T_2 were first conducted under static conditions, in a mini-Couette system using a standard Newtonian oil. T_2 was measured using a CPMG sequence, a built-in procedure by Bruker for their 20 MHz mq20 benchtop instrument. The application of this intrinsic thermometric method offers, for the first time in the field of crystallization of fats and waxes under shear flow, the possibility of having a close estimate of the actual temperature of the process that we are observing.

1.1 Objectives

The aim of this study is to develop a methodology to estimate the temperature in complex fluids under shear flow, when significant viscous heat is generated.

To do this, rheological measurements were performed simultaneously with NMR measurements of spin-spin relaxation times T_2 in a model liquid. As far as we are aware, no comprehensive study has been carried out on this subject. Thus,

The specific objectives of this study are:

- To study how T_2 relaxation time of a standard Newtonian oil changes under static conditions as the temperature changes.
- To investigate how T_2 relaxation time of a standard Newtonian oil changes under shear conditions, as a function of inlet temperature and shear.
- To set up the correlations between T_2 relaxation time and the temperature of the standard Newtonian oil obtained from the static experiments; then apply it to predict the temperature of the oil, using the T_2 measured in the shear experiments.

- To compare these NMR experimental results with the predictions of a thermo-rheological mathematical model (TRM), at different shear rates and temperatures. The TRM was developed to describe the energy generation and transport due to viscous heating of a Newtonian fluid.

CHAPTER 2 LITERATURE REVIEW

2.1 Nuclear Magnetic Resonance (NMR) Technology

Nuclear magnetic resonance (NMR) is a non-invasive spectroscopic technique which applies the phenomenon of NMR to detect molecular structures and intermolecular interactions. In recent years, the research for NMR is mainly focused on two nuclei: ^{1}H and ^{13}C (Balcı 2005). NMR has become an essential technique for natural sciences research as well as many other fields of study.

One widely used application of NMR is the measurement of solid fraction (SF) in natural and processed fats. The SF is computed as the proportional difference between the solid and liquid phase signals obtained from the sample. The signal usually detected in NMR is caused by the transitions between the high and low magnetic momentum states of hydrogen protons. The electromagnetic energy emitted while the protons make a synchronous transition from the high-energy spin-state to the low-energy spin-state is picked up by a resonator working like an antenna (Li 2011). The measurements conducted by NMR are rapid and precise which makes it a powerful technology for many manufacturers, such as pharmacy and food industry.

NMR can be used to measure the spin-spin relaxation time and the spin-lattice relaxation time, known as T_2 and T_1 respectively, for a sample. Measurements of these characteristics times are used in many fields of study, *e.g.* to calculate the oil saturation of a tight oil reservoir (Kuang, Sun et al. 2016), or to study the effect of a superplasticizer on

cement paste (Sun, Pang et al. 2011). In the experiments for this thesis, T_2 was measured from a fluid under different temperature and shearing conditions.

2.1.1 Principles of NMR

In most high-field modern instruments the magnet for NMR is usually a low-temperature superconductive one. The way of observing the atoms in NMR is to put the sample into a strong static magnetic field first, and then expose the sample to a superimposed oscillating magnetic field. By applying the second magnetic field at a frequency that resonates with the magnetic momenta of the nuclei, the nuclei start to align themselves synchronously with the oscillating field. Thus, the effect of the environment surrounding the nuclei can be probed separately from the effect of the external magnetic field. The return of the aligned nuclei to their base state delivers a signal which is strong enough to be detected by NMR.

Nuclear spin is a basic property of nature possessed by protons and neutrons, and it is quantified as the multiples of ±½. This property makes the protons align colinearly to an external magnetic field of sufficient intensity. However, not all the nuclei have their spin aligned parallel to the magnet's magnetic field direction. Close to half of the protons will align in an anti-parallel direction, effectively cancelling the observable manifestations of spin. This is because spins with opposite signs cancel out their external net effects. The remaining unpaired protons possess spin of ½. To be clearer, suppose that one proton is considered as a small magnet with north and south poles. When it's placed in an external magnetic field (B_0), the proton will align itself with that magnetic field and maintain an equilibrium state. So, if a group of nuclei is placed in the applied magnetic field (B_0), each

of the nuclei is supposed to align in one of two directions: parallel or anti-parallel to the magnetic field direction. The nuclei aligned parallel to the field are in a low energy state, whereas those aligned antiparallel are in a high energy state. The number of nuclei in the high state is slightly different from the number in the low state, and the tiny excess aligned parallel creates an equilibrium magnetization (M_0) in the sample (Li 2011).

The small fraction of unpaired nuclear spins are the protons significant in NMR (Hornak 1997).

The fraction of unpaired protons, of a given nucleus type, depends on the intensity of the magnetic field and the temperature. The expression to estimate the ratio of protons of both kinds is

$$\frac{N_{high}}{N_{low}} = e^{-\gamma B_o h / k_B T} \quad (1)$$

γ	2.68×10^{8}	rad/(T·s)	^{1}H Hydrogen gyromagnetic ratio (42.58 MHz/T)
B_o	0.47	T	External field
H	6.63×10^{-34}	J·s	Planck's constant
k_B	1.38×10^{-23}	J/K	Boltzmann's constant

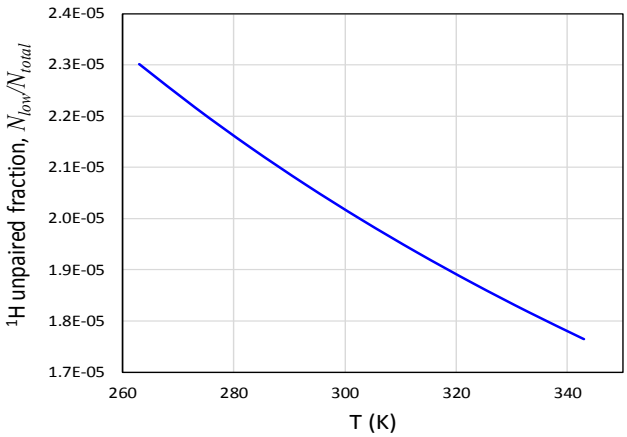

Figure 2 - 1 Unpaired ratio of magnetic spins of ^{1}H in the range of temperatures and the magnetic field relevant to this thesis.

The resonance frequency of the ^{1}H in this magnet is $\gamma \cdot B_0$, which is 20 MHz. Thus, the frequency of the oscillatory superimposed field will have to be 20 MHz. The coil in the probe has been designed to resonate at that frequency.

The equilibrium magnetization is hard to be detected because the sample's magnetization is too small compared to the external magnetic field. To break this equilibrium, an oscillating magnetic field (B_1) is applied *perpendicular* to the magnetic field (B_0). The pulsed B_1 field is created by the Radio Frequency (RF) coils twined around the glass tube of the probe. If a pulse of a proper duration is applied (90.22 μs in our case), the magnetization (M_0) will be rotated by 90º which makes the precession perpendicular to the external field. This is called, obviously, a 90º pulse. Same as the 90º pulse, the direction of M_0 is reversed by 180º when applying a 180º pulse (18.4 μs duration). They are illustrated in **Figure 2 - 2**.

To observe the phenomenon of NMR, two fundamental conditions are required. Firstly, the external resonance frequency (ν) should be equal to the Larmor frequency (ω). Secondly, the energy absorbed by the nuclei must be exactly equivalent to the energy difference between the low-energy state and the high-energy state, which can be expressed by the equations below.

$$\mathrm{N} = \gamma B_1 \tag{2}$$

$$\omega = \gamma B_0 \tag{3}$$

$$\Delta \mathrm{E} = \mathrm{h}\nu \tag{4}$$

where γ is the gyromagnetic ratio of the nuclei, and h is Planck's constant (6.626×10^{-34}J·s, as was indicated earlier).

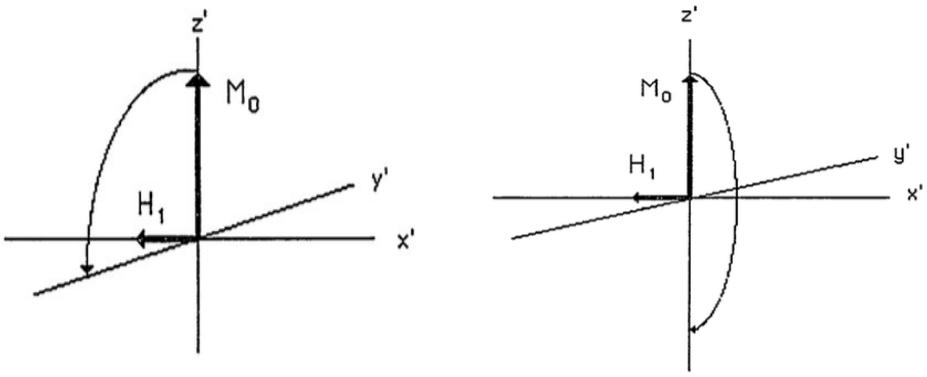

Figure 2 - 2 A 90º and a 180º pulse in the rotating frame (Zega 1991)

2.1.2 Time Domain Nuclear Magnetic Resonance Technology

Low-field, time domain nuclear magnetic resonance (TD-NMR) is the main technology used for this research. It is widely applied to food industries for QC/QA applications (Todt, Guthausen et al. 2006). Unlike frequency domain NMR, it can only be used to deal with time domain NMR signals, and is not capable of offering magnetic resonance imaging (MRI) or spectroscopy, due to the weak pulse sequences and lack of spectral resolution (Li 2011). The weak pulse sequences sufficient for TD-NMR allow the use of instruments that are commonly small, with low-resolution, and with a low magnetic field. The magnetic field employed usually corresponds to Larmor frequencies in the range of 10 to 60 MHz for ^{1}H, i.e. 0.24 to 1.41 T.

Typically, analytical spectrometers operate at several hundred MHz, and then the time domain information is converted to the frequency domain by Fourier Transforms (FT) (**Figure 2 - 3**). The same thing can be done with a low-field instrument, but it's not able to get a well-resolved spectrum (Thomas Elder 2007), because the TD-NMR instruments

usually use a much lower magnetic field. In fact, the procedures used in these TD_NMR machines are often called low-field NMR applications.

The technique, however, is used successfully in many industries, such as food, cosmetics, pharmaceuticals and polymers, in which materials containing hydrogen nuclei (or fluorine ^{19}F, which has similar resonance frequency), need to be evaluated during their production.

The application of TD-NMR started about 47 years ago with the cooperation of Bruker Physik Analytik GmbH (Germany) and Unilever Research (The Netherlands), who aimed at building a small table-top TD-NMR analyzer to study the solid fraction of fat materials (Todt, Guthausen et al. 2006). Since then, TD-NMR has been used throughout many areas of industries and research, especially food science and technology.

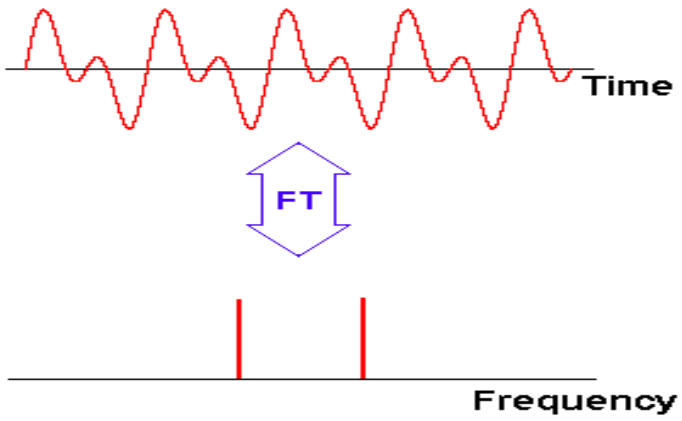

Figure 2 - 3 Schematic representation of the relationship between time domain and frequency domain, represented by a wave composed of two defined frequencies. (Hornak 1997)

2.1.2.1 T_1 & T_2 Relaxation Time

When the nuclei absorb energy from the oscillating magnetic field, they become excited (high-energy state). If the oscillatory field is removed, the nuclei start to emit the energy, so that they can return to the equilibrium state. The time required for the nuclei to return to their original configuration, after excitation, is called "relaxation time". The characteristic time for the energy to be dissipated to the surrounding field is called spin-lattice relaxation time T_1, also known as longitudinal relaxation time. If the energy is instead dissipated to the neighboring nuclei, the characteristic time is called spin-spin relaxation time T_2, or transverse relaxation time. The equations governing these behaviors as a function of time are exponential,

$$M_z(t) = M_0 - [M_0 - M_z(0)]e^{-t/T_1} \quad (5)$$

$$M_{xy}(t) = M_{xy}(0)e^{-t/T_2} \quad (6)$$

where M_z is the longitudinal magnetization, and M_{xy} is the transverse magnetization.

The duration of the T_1 relaxation generally depends on the NMR frequency, and therefore it varies when the external magnetic field strength is changed. On the other hand, T_2 is usually much less dependent on the magnetic field intensity. T_2 is always less than or equal to T_1, because on top of the magnetic field, there are additional local factors that make the loss of transverse magnetization progress faster.

According to the literature graph shown in **Figure 2 - 4**, T_2 relaxation time increases with the increase of temperature. Slow motion can correspond to a low temperature range, whereas fast motion corresponds to a high temperature range.

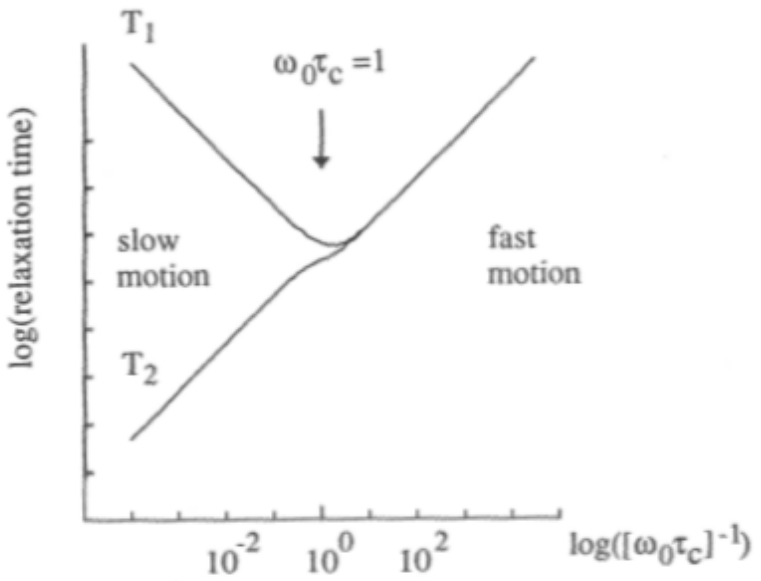

Figure 2 - 4 The T_1 and T_2 relaxation times are plotted as a function of rotational correlation time, τ_c, at a fixed Larmor frequency (Callaghan 1993).

A time domain signal can be induced by several methods. Four commonly used pulse sequences are presented here, each of which is a set of RF pulses applied to a sample to produce a specific form of NMR signal (Bernstein, King et al. 2004). They are: free induction decay (FID), inversion recovery, spin-echo sequence, and Carr-Purcell-Meiboom-Gill (CPMG) sequence.

2.1.2.1.1 Free Induction Decay (FID)

FID is the simplest form of the signal in NMR and MRI. The RF coils in an NMR spectrometer or an MRI scanner pick up the electromagnetic energy released by the previously excited nuclei. This creates an induced current, that is measured. The strength of the signal gradually decays to zero because of the relaxation process of the nuclei. The intensity of the signal as a function of time is referred to as an FID signal.

An example using a 90-FID pulse sequence is illustrated by the timing diagram shown in **Figure 2 - 5 (a)**.

2.1.2.1.2 Inversion Recovery

The Inversion recovery pulse sequence can be used for T_1 relaxation time measurements. The sequence starts with a 180º pulse, and then a 90º pulse is applied, before the nuclei get back to equilibrium. Eventually, an FID is acquired. The timing diagram is shown in **Figure 2 - 5 (b)** and T_1 can be deduced from the following exponential equation:

$$M_z(t) = M_0[1 - 2e^{-t/T_1}] \quad (7)$$

where t is the time between the 180º and 90º pulses.

2.1.2.1.3 Spin-echo Sequence

The spin-echo sequence takes advantage of the very fast flipping of spins that can be accomplished with a 180º pulse. The sequence starts with a 90º pulse. After it is finished, the transverse magnetization begins to dephase. A short time later, a 180º pulse is applied to flip the spins, so that their direction of dephasing is reversed, while keeping their rate of dephasing. As faster dephasing spins catch up to the slower ones, they all eventually superimpose, producing a partially refocused magnetization, which generates a signal called echo. The timing diagram is shown in **Figure 2 - 5 (c)**.

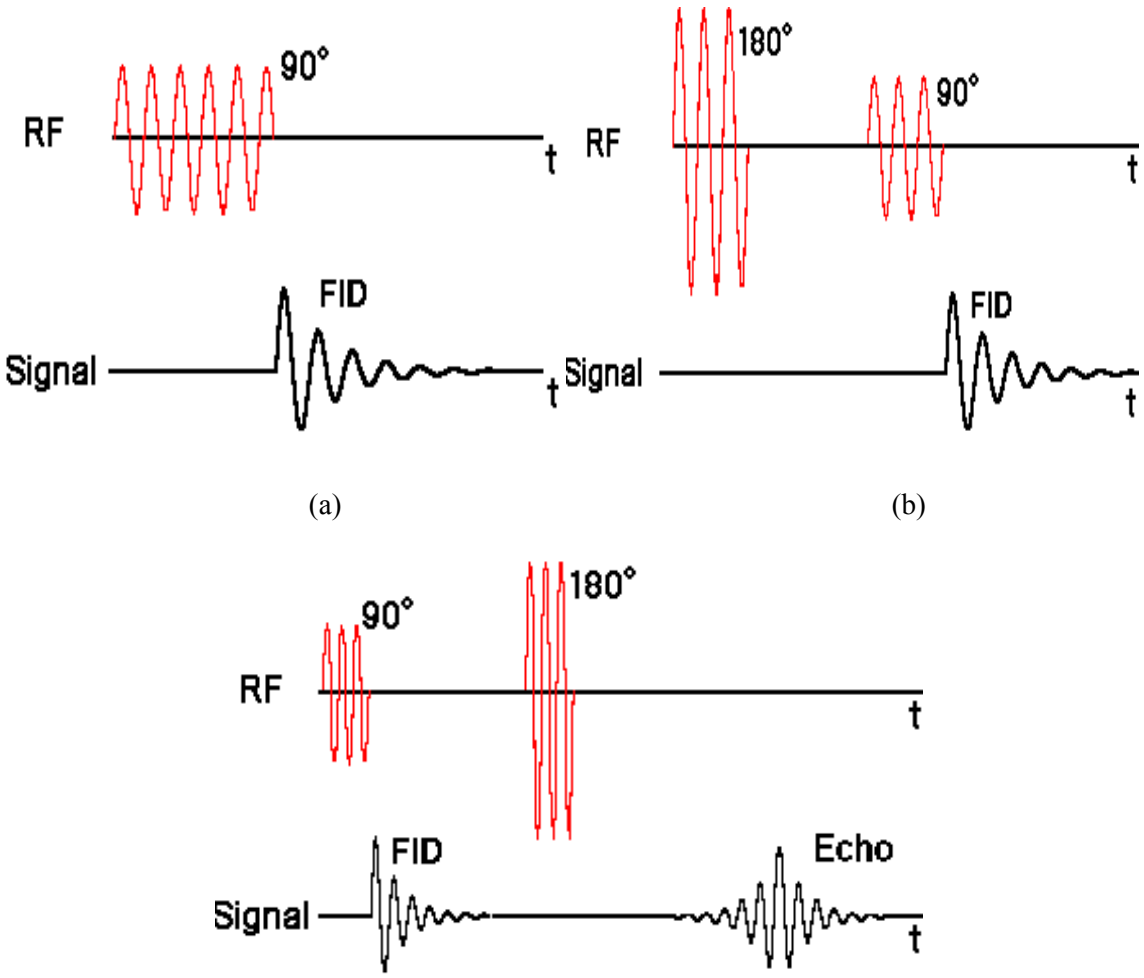

Figure 2 - 5 The timing diagrams representing the relative positions of the RF pulse(s) and the signal (Farrar and Becker 1971), (a) is for 90-FID sequence, (b) is for inversion recovery and, (c) is for spin-echo sequence.

2.1.2.1.4 Carr-Purcell-Meiboom-Gill (CPMG) Sequence

Carr and Purcell first demonstrated, in 1954, that a complete T_2 relaxation data set could be obtained by measuring each resulting echo appearing between successive $180°_x$ pulses within a single experiment. Four years later, this approach was improved by Meiboon and Gill. They introduced a simple modification, which used better electronics to

generate coherent pulses with the initial 90^{o}_{x} pulse, compensating for imperfections in the 180^{o} pulses by generating them in the "y" direction, i.e. 180^{o}_{y} normal to the 90^{o}_{x} pulses (Roberts 2013). Nowadays, the CPMG pulse sequence is usually implemented by applying a 90^{o}_{x} pulse followed by several 180^{o}_{y} pulses, which are equally spaced by a short time constant (τ), to densely record the relaxation process, and to avoid relaxation processes that are due to diffusion (Ronczka and Muller-Petke 2012). The timing and amplitude diagrams are shown in **Figure 2 - 6**.

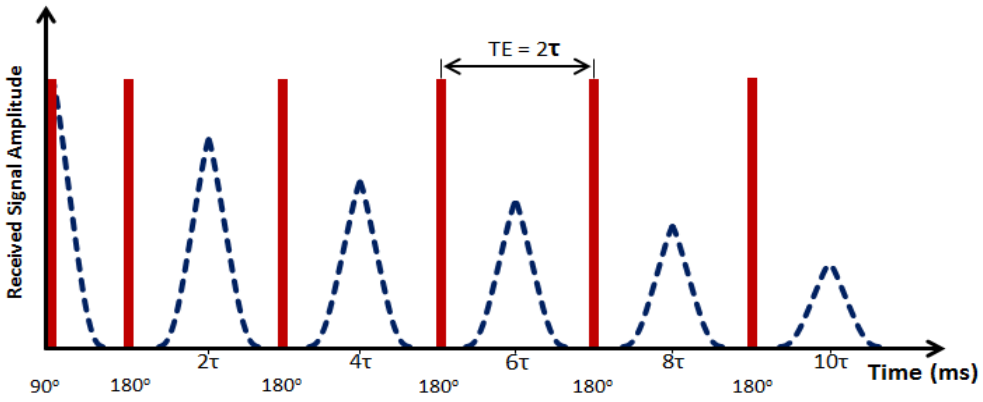

(a)

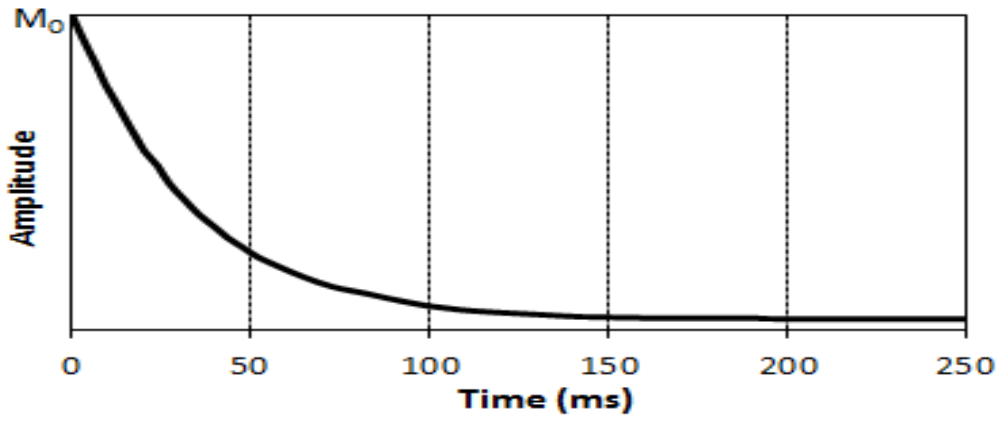

(b)

Figure 2 - 6 (a) is the CPMG pulse sequence timing diagram, (b) is the amplitude of the decaying spin echoes yield an exponentially decaying curve with time constraint T_2 (Kantzas, Bryan et al.).

2.1.2.2 Applications

As indicated before, TD-NMR technology has been applied to many fields of study. The classic application in food science and industry is to determine the concentration or the amount of a specific component in the products with a dominating proportion of water or fat (Guthausen, Todt et al. 2006). In those fields, the classical approach for fat content determination in wet food is to implement a pre-drying step before running NMR, but it's time-consuming and inefficient. In recent years, more developed methods have been created. The first one is to run pulsed field gradient (PFG) experiments, which is referred as the PFG-NMR approach. Different PFG sequences should be applied based on the relaxation and diffusion properties of the product. The way to determine the fat content is to extrapolate the fat signal to zero gradient strength. Because the diffusion coefficients of water and oil are quite different, the difference causes only the fat signal left at larger gradients. The second approach is a combined relaxation analysis, which aims at determining the magnetization at a given time by both T_1 and T_2. It can be realized whether through a steady state dynamic equilibrium method (Guthausen, Zimmer et al. 1998) or by using the longitudinal recovery of magnetization and measuring the transverse magnetization of the T_1 curve by CPMG method (Tinsley, Taicher et al. 2004).

However, the application of TD-NMR is not limited to the areas shown above. The magnetization relaxation depends not only on the components but also on other parameters, such as temperature. Recently (Carosio, Bernardes et al. 2016) conducted a study on the correlation between magnetization relaxation and temperature. They recorded the oil temperature in seeds, and measured T_2 by CPMG and continuous wave free precision (CWFP) pulse sequences (Azeredo, Colnago et al. 2000, Venancio, Engelsberg et al. 2005,

Venancio, Engelsberg et al. 2006, Carosio, Bernardes et al. 2016). The correlation between T_2 and the oil temperatures was summarized by fitting an equation to the data pairs. A similar research about the relationship between T_2 and temperature was conducted by MRI by (Yuhua Peng, Honghong Dong et al. 2010). They found a cubic relationship, shown in equation (8). Despite dissipated surface heat and inaccurate measurements, the authors believe this method can provide in the future efficient temperature monitoring clinical cancer hyperthermia.

$$T_2 = 0.001942T^3 - 0.2007T^2 + 7.14T - 68.63 \quad (8)$$

Here T is the internal temperature of the material.

Studies on the correlation between T_2 and temperature are still insufficient, and the relationship is waiting to be explored thoroughly. Therefore, a purpose of this thesis is to attempt to set up a reliable correlation between T_2 and temperature, so that T_2 can be used as a tool to predict the temperature in a mini-Couette cell. All the experiments have been done in a low-field TD-NMR with a temperature control system. More detailed information is discussed in later sections.

2.2 Viscous Heating under Shear

Viscous heating plays an important role in the dynamics of fluids with highly temperature-dependent viscosity, especially fluids subjected to flow under high shear rates. The heat is produced by the intermolecular friction, and it is can cause a temperature increase, with a consequent decrease of the viscosity, which in turn changes considerably the temperature and velocity profiles (Costa and Macedonio 2003). In a rheometer

experiment, the temperature throughout the sample under high shear rates is usually assumed to remain the same as the temperature commanded to the sample holder. But the truth is that the actual temperature measured directly from the sample is always off compared with the set temperature. This is due to the viscous heat generated, and it is often non-avoidable, even when precise measurements are demanded.

Therefore, quantifying the energy generated and transferred in a fluid being studied under shear is necessary, both from the scientific and practical points of view.

2.2.1 The Study of Viscous Heating

Viscous heating has been widely used in geophysics, which is the branch of geology that uses physics to study the Earth's structure, climate, and oceans. It was previously invoked to explain the rheological behavior of basalts (Shaw 1969) and describe some phenomena in earth science research, such as the mantle instability (Hansen and Yuen 1996, Larsen, Yuen et al. 1997) and magma flows (Costa and Macedonio 2003).

One model has been adopted (Fujii and Uyeda 1974) to simulate the changes of magma flow in volcanic conduits, but it only works for infinitely long tubes. In 2007, an estimation was made to evaluate the effect of viscous heating in capillary rheometry of polymer melts by using numerical simulation (Syrjälä and Aho 2007). In that research, the equations of continuity, momentum, and energy were solved along with the viscosity model and boundary conditions using the finite element method. Both models demonstrate the importance of viscous heating in fluid dynamics and how it can produce substantial temperature gradients within the sample.

2.2.1.1 Viscous Heating in Couette Flow

Maurice Couette published his work of experiments on the flow between a fixed (inner part) and a rotating (outer part) concentric cylinder in 1890. In honor of him, the steady flow of a viscous fluid in the relative motion of two parallel plates is referred as Couette flow. Seventy years later, a person named G. I. Taylor firstly showed the theoretical explanation of an instability that causes the laminar flow to the vortex flow by making the inner cylinder rotating within the stationary outer one (Burton 2000).

Couette flow was probably treated for the first time (without the name) in the classical book 'Principia Mathematica' by Sir Isaac Newton (1867, Book II, section IX) and is discussed in almost every fluid mechanics book. It is well known that heat is generated when one body is moving relatively along another body. The heat generated by friction between the fluid particles is called viscous heating or dissipation. For instance, when viscous heating was considered in White's book (White 2006), viscosity and thermal conductivity were assumed to be constant for convenience, which is not true in most cases. A recent study has set up a mathematical model which takes the variation of viscosity and thermal conductivity into account with different fluid properties (Pantokratoras 2007). It is a very impressive work which could make the estimation of viscous dissipation more accurate for both research and industry.

The investigation of viscous heating has also been extended to the field of micro-mechanics of small devices. In 2005, a study has presented a continuum model to solve the problem of liquid and gas flow in micro-channels, and then the estimations of the theoretical data were compared with the experimental data obtained from the last decade (Hetsroni, Mosyak et al. 2005). Similar work has been done on the viscous heating in micro-

channels with non-adiabatic walls (Mossaz, Colombet et al. 2015) and in nano-channels associated with shear driven liquid flows (Kim, Beskok et al. 2010).

2.2.1.2 Viscous Heating in Crystallization Process

In crystallization processes under shear flow, the formation of crystals causes the increase in viscosity, with the consequent increase in viscous heat generation (Wang, Johnson et al. 2012). The heat generated can increase the flow temperature, which obviously imposes a limitation to the crystallization temperature. In other words, the number of solids that can be crystallized under shear flow tends to be limited due to the viscous heat generation, in some specific cases of crystallization of fats under shear flow. Therefore, viscous heating under shear flow is particularly important for the study of crystallization of lipids and host of other materials.

2.2.1.2.1 Crystallization under Shear

Shearing is an ubiquitous and important process in the food industry, especially if fat crystallization is needed during the manufacturing process. Proper shearing conditions are necessary to obtain the quality of the lipid-based foods, for instance (Mazzanti 2005). Therefore, understanding the relationship between crystallization kinetics and shear would help design the equipment and optimize the manufacturing process.

The usual function of shear is to increase the rate of heat transfer, as well as to get a homogeneous and stable final product in the classic manufacturing process of fats, which has been discovered many years ago (Li 2011). Early in 1962, it was showed that

mechanical work would affect the solid-to-solid transformation to a more stable polymorphic form (Feuge, Mitcham et al. 1962); although some studies have been made on the various forms of fats and materials, the knowledge about how shear rates affect the crystallization behaviour and the crystal structures is still very scarce and limited (Mazzanti, Marangoni et al. 2005).

In recent studies, devices have been designed and set up to better understand the crystallization process of triglyceride blends using Rheo-NMR and Rheo-XRD (Mazzanti and Mudge 2008, Mazzanti, Mudge et al. 2008, Mudge and Mazzanti 2009). The gap between the poles of the magnet of the low field NMR is very small, so the radii of devices are designed small enough to fit in that gap. Moreover, the viscous heat generated at high shear rates is considerably large which requires the heat dissipation of the devices working properly. The NMR signal strength can be improved if the gap between the shaft and the tube is increased, but a smaller gap is necessary when an ideal shear rate profile is demanded (Mudge and Mazzanti 2009). To solve this issue, a compromise is reached where the gap is large enough to produce good signal, while not distorting too much the flow pattern.

2.2.2 The Methodology Used in the Research

The methodology used in this thesis is an extension of the work reported by (Wang, Johnson et al. 2012), which aimed at developing a methodology that could be applied to predict energy generation and transport in a fluid in a mini-Couette cell. The calculations are applied to cases under various temperatures and shear rates in a small device.

There are several published papers relevant to the estimation of the properties of the fluid used in this study. A Rheo-MRI system was conducted to obtain the nonlinear isothermal velocity profile in the gap of a cylindrical Couette cell using a strong field magnet (Britton, Callaghan et al. 1998, Britton and Callaghan 2000). One study was published in 2000 to analyze the thermodynamics of thermomechanical coupling and the temperature distribution in the gap of a Couette cell for a Newtonian fluid with temperature independent viscosity and thermal conductivity (Demirel 2000). Another two models (Gavis and Laurence 1968, Papathanasiou 1998), which use a polynomial to predict both the viscosity and the thermal conductivity of the fluid, can also be imposed to estimate the viscous heating in a plane or a circular flow between moving surfaces with the inner cylinder fixed and the outer one rotating.

In Wang's work (Wang, Johnson et al. 2012), a mathematical model has been developed based on the isothermal wall conditions around an adiabatic shaft in a Couette flow (Papathanasiou 1998) to estimate the viscous heating in a cylindrical Couette cell with the inner cylinder rotating and outer one fixed. Ideally, the temperature profile should be measured directly by a device inserted in the fluid; however, the gap between the rotating shaft and the tube is very small and the immersed measuring device would distort the flow, which makes it difficult to measure the temperature profile directly from the fluid. A method needs to be figured out to estimate the fluid temperatures, which is one of the goals for this thesis. The temperatures can be estimated by measuring T_2, so long as the correlation between those two parameters is known. The estimated temperatures and the temperatures from the model will be compared to evaluate the reliability of the model. The results and discussion will be presented later.

2.2.2.1 Development of the thermo-rheological model

The basic transport equations used for the model are found in *Transport Phenomena* (Bird, R.B. et al. 1998), and the equations can be written as

$$\frac{\partial(\rho u)}{\partial t} = \nabla \cdot \left(-\frac{\eta}{\rho} \nabla(\rho u) \right) \tag{9}$$

$$\frac{\partial T}{\partial t} = \nabla \cdot \left(-\frac{k}{\rho \cdot C_p} \nabla T \right) + \frac{\tau_s : \nabla u}{\rho \cdot C_p} \tag{10}$$

where the two equations are to describe momentum transfer, and heat transfer and generation respectively.

Two assumptions have been made to simplify the model. Firstly, the sample is under steady state without axial or angular changes of flow lines, and only heat conduction inside the sample was considered (Wang, Johnson et al. 2012). Secondly, the slight temperature change due to the vertical flow of the heat-exchanging medium can be neglected. Based on the assumptions, the non-dimensional momentum transfer equation (11) and the heat transfer and generation equation (12) were derived (Papathanasiou 1998).

$$\frac{1}{x^2} \left\{ \frac{\partial}{\partial x} \left[\frac{\eta}{\eta_0} x^3 \frac{\partial}{\partial x} \left(\frac{u}{x} \right) \right] \right\} = 0 \tag{11}$$

$$\frac{1}{x} \frac{\partial}{\partial x} \left[\frac{k}{k_0} x \frac{\partial \theta}{\partial x} \right] + N_{Br} \frac{\eta}{\eta_0} \left[x \frac{\partial}{\partial x} \left(\frac{u}{x} \right) \right]^2 = 0 \tag{12}$$

where $x = \frac{r}{r_o}$, $u = \frac{u_\theta}{\dot{\omega} \cdot r_i}$, $\theta = \frac{T - T_0}{T_0}$, $\dot{\omega} = 2\pi\nu$, and $N_{Br} = \frac{\eta_0}{k_0} \frac{(\dot{\omega} \cdot r_i)^2}{T_0}$.

The thermal conductivity term $\frac{k}{k_0}$ is the ratio between the thermal conductivity k at the temperature at any non-dimensional position x and the thermal conductivity k_0 at the reference temperature T_0. The viscosity term $\frac{\eta}{\eta_0}$ is the ratio between the viscosity η at the temperature at the point x and the viscosity η_0 at the reference temperature. The non-

dimensional position x is the ratio between radius r and radius at the wall r_o. The non-dimensional velocity u is the ratio between the local velocity u_θ and the tangential velocity $u_{\theta s}$ at the shaft. The non-dimensional temperature θ is defined as the ratio of the difference between the temperature T at point x and the reference temperature T_0 over the reference temperature. The non-dimensional Brinkmann number N_{Br} evaluates the relationship between the reference values of the fluid properties, the temperature, and the tangential velocity of the shaft.

Equation (11) is derived from the Navier-Stokes relationships, with no axial flow and no axial temperature gradients. Equation (12) is derived from Fourier's equation, in which the first term is the heat transferred at the point x and the second term is the heat generated at x. The second term is derived from the friction heat generated per unit volume of the fluid, which can be written as (Bird, R.B. et al. 1998):

$$\dot{q}_v = \tau : \nabla u \tag{13}$$

In the case of the simplified conditions assumed, it becomes

$$\dot{q}_v = \eta \cdot \dot{\gamma}^2 \tag{14}$$

The non-dimensional Dirichlet boundary conditions are:

$$\text{for } r = r_i;\ x = \kappa \text{ and } u_x = 1 \quad \text{with } \kappa = \frac{r_i}{r_o}$$

$$\text{for } r = r_o;\ x = 1 \text{ and } u_x = 0$$

where r_i is the radius of the shaft, r_o is the radius at the wall.

In the model, the general form of the velocity (15) and temperature (16) have been rewritten in equation (11) and (12) respectively for the convenience of numerical solutions (Wang, Johnson et al. 2012). The equations are given below.

$$\ddot{u} = \frac{Ax+1-B\cdot\dot{\gamma}_n}{1+B\cdot\dot{\gamma}_n}\left(-\frac{\dot{\gamma}_n}{x}\right) \tag{15}$$

$$\ddot{\theta} = -\left[\frac{\dot{\theta}}{x} + \frac{T_0}{k}\frac{\partial k}{\partial T}\dot{\theta}^2 + \frac{{r_o}^2}{T_0}\frac{\eta}{k}{\dot{\gamma}_n}^2\right] \quad (16)$$

where $\dot{u} = \frac{\partial u}{\partial x}$, $\ddot{u} = \frac{\partial \dot{u}}{\partial x}$, $A = \frac{T_0}{\eta}\frac{\partial \eta}{\partial T} \cdot \dot{\theta}$, $\dot{\theta} = \frac{\partial \theta}{\partial x}$, $\ddot{\theta} = \frac{\partial \dot{\theta}}{\partial x}$, $B = \frac{1}{\eta}\frac{\partial \eta}{\partial \dot{\gamma}_n}$, and $\dot{\gamma}_n = \left(\dot{u} - \frac{u}{x}\right)$.

For an isothermal system, the term *A* will be zero, so equation (15) becomes

$$\ddot{u} = \frac{1 - B \cdot \dot{\gamma}_n}{1 + B \cdot \dot{\gamma}_n}\left(-\frac{\dot{\gamma}_n}{x}\right) \quad (17)$$

For a Newtonian fluid with non-isothermal condition, the term *B* will be zero, so equation (15) becomes

$$\ddot{u} = (Ax + 1)\left(-\frac{\dot{\gamma}_n}{x}\right) \quad (18)$$

2.2.2.2 Application of the Model

The model can be applied to three conditions which are the isothermal condition, non-isothermal condition to a constant temperature sink independent of heat flow, and the condition in which heat is transferred to the external fluid through the wall.

2.2.2.2.1 Isothermal Condition

When the shaft is rotating at a low speeds, the system is close to an ideal isothermal condition across the sample gap and along the axis of the cylinder, which means the viscous heat generated and the temperature difference between the sample and the heat exchanging fluid (Galden) are negligible (Wang, Johnson et al. 2012). The equations are given as:

$$\sigma = \eta \cdot \dot{\gamma} \quad \text{or} \quad \sigma = \frac{\tau_s}{r_i \cdot A_s} \quad (19)$$

$$\dot{\gamma} = r\left(\frac{\partial \dot{\omega}}{\partial r}\right) = \frac{\partial u_\theta}{\partial r} - \frac{u_\theta}{r} \quad (20)$$

where η is the local viscosity, σ is the shear stress, $\dot{\gamma}$ is the shear rate, A_s is the effective shaft-fluid contact area, τ_s is the measured torque, and $\dot{\omega}$ is the angular velocity.

The velocity is independent of the magnitude of the viscosity if the system is considered isothermal. And the non-dimensional ratio u_x and corresponding shear rate $\dot{\gamma}_x$, based on the derivation of the isothermal velocity profile from equation (11) (Bird, R.B. et al. 1998), can be expressed as:

$$u_x = \frac{u_\theta}{u_{\theta s}} = \frac{u_\theta}{\dot{\omega} \cdot r_i} = \frac{\kappa(x^2-1)}{x(\kappa^2-1)} \tag{21}$$

$$\dot{\gamma}_x = \frac{u_{\theta s}}{r_o} \frac{\kappa}{(\kappa^2-1)} \frac{2}{x^2} \tag{22}$$

for the volume-weighted average shear rate

$$\dot{\gamma}_{av} = \frac{-4 \cdot \kappa^2 ln(\kappa)}{(1-\kappa^2)^2} \cdot \dot{\omega} \tag{23}$$

for the large radius – small gap situation ($\kappa \approx 1$), the shear rate is

$$\dot{\gamma}_{lrsg} = \frac{\dot{\omega} \cdot r_i}{r_o - r_i} = \frac{\kappa}{1-\kappa} \cdot \dot{\omega} \tag{24}$$

2.2.2.2.2 Non-isothermal Condition

When the heat generated is considerable, usually the case for high shear rates or high viscosity samples, the temperature would increase across the sample gap. Therefore, the change of viscosity and thermal conductivity should be considered due to their strong dependency on temperature. The equations are re-organized for the convenience of solving them with commercial software.

$$\frac{\partial \dot{u}}{\partial x} = \left(1 + x \cdot \frac{T_0}{\eta} \frac{\partial \eta}{\partial T} \cdot \dot{\theta}\right) \cdot \left(-\frac{\dot{\gamma}_n}{x}\right) \tag{25}$$

$$\frac{\partial \dot{\theta}}{\partial x} = -\left[\frac{\dot{\theta}}{x} + \frac{T_0}{k}\frac{\partial k}{\partial T}\dot{\theta}^2 + N_{Br}\frac{k_0}{k}\frac{\eta}{\eta_0}(\dot{\gamma}_n)^2\right] \quad (26)$$

Equation (25) is derived from equations (16), (18) and (20), whereas equation (26) is derived from equations (12) and (16). The derivatives of viscosity and thermal conductivity can be plugged into the equations to solve the differential equations with an additional boundary condition (Neumann boundary condition).

For the non-isothermal condition, the shaft is assumed adiabatic ($\dot{\theta} = 0$). The equations have been solved, for the conditions studied, using Matlab®.

2.2.2.2.3 Heat Transferred to the External Fluid

The difference between the inlet and outlet temperatures of the Galden is caused by the heat transferred from the sample to the external fluid. Hence, the energy transferred should be the same as the viscous heat generated in the sample. It is stated in the model that no instabilities are considered in the laminar flow inside the sample tube (Wang, Johnson et al. 2012). The heat is transferred from the sample fluid through the walls. Finally, the heat will be transferred to the Galden. The equations used to calculate the heat are,

$$\dot{q} = \frac{A_o k_x}{r_o ln\left(\frac{r_{ig}}{r_o}\right)}\left(T_{wo} - T_{wg}\right) \quad (27)$$

$$\dot{q} = \left(T_{wg} - \bar{T}_g\right)A_{ig}h_g \quad (28)$$

where $\dot{q}$ is the heat transferred between the sample and the wall, A_o is the heat transfer area between the sample and the wall, k_x is the thermal conductivity of the wall, r_{ig} is the radius of the Galden tube outside the static cylinder, T_{wo} is the temperature of the sample at the wall, T_{wg} is the temperature of the Galden at the inner wall, $\bar{T}_g$ is the bulk temperature of

the Galden, A_{ig} is the heat transfer area between the wall and the Galden, and h_g is the heat transfer coefficient of the Galden.

The heat gained from the environment, $\dot{q}_{env}$, can also be quantified by the mass flowrate ($\dot{m}_g$) of the Galden, its specific heat (C_{pg}) and the inlet and outlet temperature (T_{gi} and T_{go} respectively).

$$\dot{q}_{env} = \dot{m}_g C_{pg}\left(T_{go} - T_{gi}\right) - \dot{q} \tag{29}$$

2.3 Rheological Properties of the Fluid in a Couette Cell

Rheological properties can be measured by a rheometer under various external conditions, such as stress, strain, and temperature. These properties impact all stages of the processing and use of substances. Therefore, knowledge of these properties is very useful in many industries, since they determine characteristics ranging from crystallization processing to food stability.

A large number of experimental and theoretical studies have been done on fluids containing suspended solids in circular Couette flow since 1888 (Mallock 1888, Mallock 1896). Most of these studies have looked at the shear impact on suspensions of hard spheres during a crystallization process in a circular Couette system (Li 2011). Interestingly, two contrary conclusions were made from those studies; part of the researchers held the idea that the nucleation rate would enhance a shear-induced order (Ackerson 1990, Haw, Poon et al. 1998), whereas others argued that shear would suppress crystallization (Palberg, Mönch et al. 1995, Okubo and shiki 1999). A possible solution to this issue was proposed by (Blaak, Auer et al. 2004), who tried to explain the contrary observations by noting that

the shear may not only induce layering in the fluid, facilitating nucleation, but also could remove matter from small crystals, which would cause the birth of crystals to be suppressed.

The rheological properties can also be applied to fat crystal suspensions during crystallization, but the observed phenomena were different from those of suspensions of hard spheres. One study showed that the measured torques of the liquid oil, which were low before crystallization, encountered a sudden increase at the crystallization point. That was because the sample of confectionery coating fat behaved as non-Newtonian fluid when partially crystallized (Garbolino, Ziegler et al. 2000).

It has been commonly accepted that the studies of rheological properties are of importance to both industry and research. The rheological data can be used to infer the shear impact on crystallization through the change of viscosity or measured torque, as well as to study the shear effect on the acceleration of the phase transformation at various temperature conditions (Li 2011).

CHAPTER 3 EXPERIMENTAL METHODS AND MATERIALS

3.1 Materials

The sample used for this work was a standard Newtonian oil, Cannon N1000 (Cannon Industries Inc., Rochester, NY, US) which was prepared by Cannon, an ISO 9001:2000-registered and A2LA-accredited laboratory. Density and viscosity of this oil at many temperatures, ranging from 20 to 100 °C, were provided by the manufacturer.

Table 3 - 1 The viscosity and density of Cannon N1000 oil, at temperatures ranging from 20 to 100 °C (data from manufacturer: Cannon™ 9727C52)

Temperature (℃)	Viscosity (mPa·s)	Density (g/mL)
20.0	2860.00	0.8499
25.0	2010.00	0.8469
40.0	786.80	0.8380
50.0	459.20	0.8321
60.0	283.50	0.8262
80.0	124.70	0.8144
100.0	63.83	0.8027

The viscosity at other temperatures cannot be obtained from the table above, so a viscosity constitutive equation (Andrade 1930) was used to interpolate values for the N1000 standard oil.

$$\eta = exp\left(a_m + \frac{b_m}{T+c_m}\right) \tag{30}$$

Here a_m, b_m, and c_m are the viscosity parameters of the Andrade equation of the standard

oil.

The three parameters were obtained by minimization (using Excel Solver) of the squared differences between the viscosities from equation (30), and those of **Table 3 - 1**. The estimated parameters are shown below:

$$a_m = -2.7403$$

$$b_m = 1551.5$$

$$c_m = 124.97$$

Shown in **Figure 3 - 1** is a plot of the calculated viscosities together with the theoretical ones at their corresponding temperatures, ranging from 0 to 100 °C. It is apparent that the calculated ones are perfectly following the trend of the values provided by the manufacturer. Therefore, the calculated a_m, b_m, and c_m are reliable to predict the viscosity of the standard oil N1000.

The density correlation derived from **Table 3 - 1** is shown below:

$$\rho = -5.900\times10^{-4}\cdot T + 0.8616 \quad (31)$$

The other important fluid used was the heat exchanging liquid. In this work it was a liquid perfluorinated hydrocarbon (Galden HT 135, Solvay Solexis, West Deptford, NJ, US), commercially known as Galden, as it will be called in the later sections. The fluid is invisible to the NMR instrument because there's no hydrogen in the fluid (Wang, Johnson et al. 2012), which is the most important reason for choosing it as the heat exchanging fluid. Moreover, it has a relatively low viscosity and a wide operating temperature range, from -50 to 125 °C, with a boiling point at 135 °C. These properties allow its use as a heat transfer fluid in the temperature span of this research (0 - 70 °C).

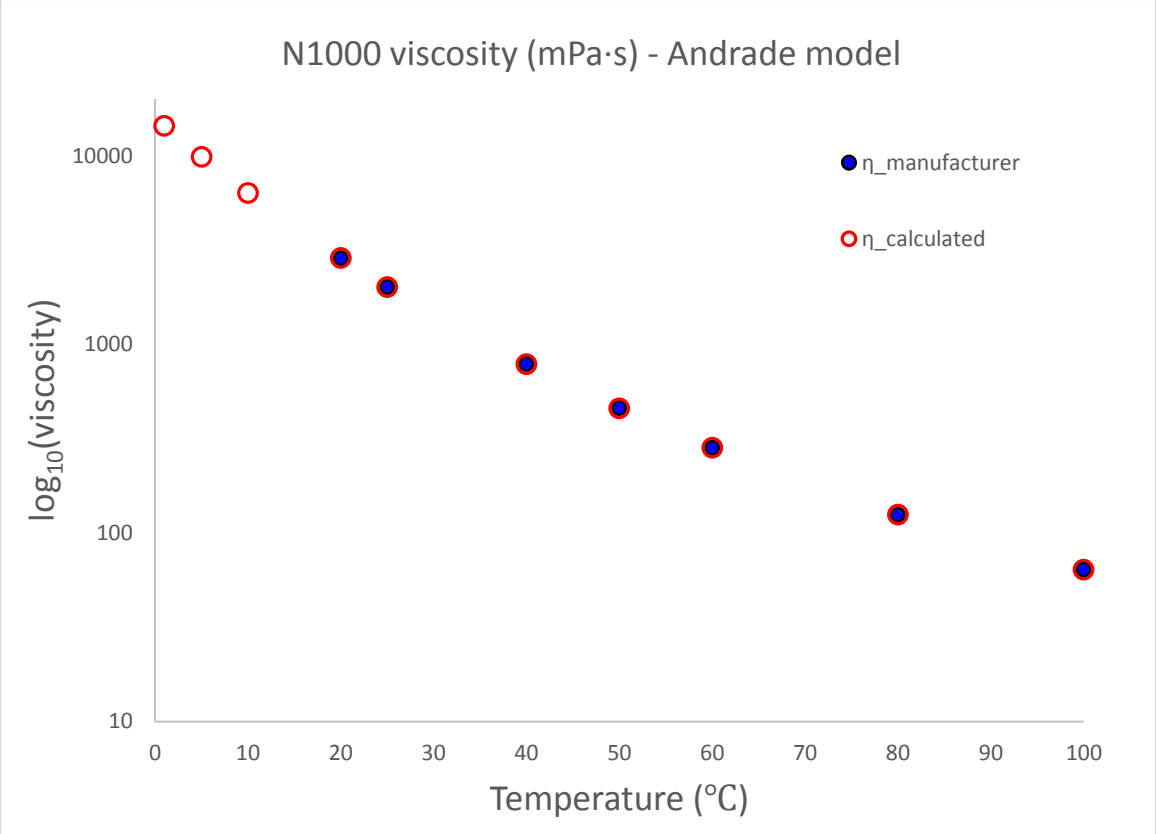

Figure 3 - 1 Logarithmically scaled viscosities from manufacturer and calculation, as a function of temperature.

3.2 In-House Experimental Setup

Some preliminary work was needed before the main experiments were carried out. The three most important preliminary steps are described in this section. The first one was to calibrate the temperature measuring devices, since several different contrivances were used to measure temperatures. Due to instrumental errors unique to each device, the temperature readings were slightly different. Secondly, a thermal unit, which was placed inside the NMR and around the glass tube-holder of the probe, was designed so that the heat exchanging fluid could flow through it, to cool or heat the sample. Thirdly, a

temperature control system was set up to control the temperature of the sample. More details are provided in their corresponding sections.

3.2.1 Fiber Optic Temperature Sensor & Thermistor Calibration

Three fiber optic temperature sensors (FOT, ReFlex 2 Ch, 1 Ch, with T1 fiber optic sensor, Neoptix Inc., Montreal, QC, Canada) and a thermistor (TR67-170, 15kOhm, Oven Industries Inc., Camp Hill, PA, US) were used to measure the temperatures simultaneously. One FOT was placed directly into the sample tube for the static measurements. The FOT was carefully checked to make sure that its tip was submerged in the sample fluid. The other two FOTs were located at the two flow channels of the thermal unit, to measure the entrance and the exit temperature of the Galden. The thermistor was used to measure the inlet temperature of the Galden as well, but it was placed outside the NMR and right after the active heat exchanger described later. All the temperatures were read and recorded by a custom-made interface developed in LabVIEW software (Version 14.1.3, National Instruments Inc., Austin, TX, US). The readings of FOTs were additionally recorded by a custom modification to the Bruker software (the minispec, Bruker Optics Inc., Billerica, MA, US) by reading serial ports. The FOTs and the thermistor were calibrated using a standard thermometer (NIST traceable, Fisher Scientific, temperature range: -10 to 40 °C) under various temperatures. The calibration test was conducted by immersing the devices in the temperature controlled cup of the advanced rheometer AR2000 (TA instruments, Newcastle, DE, US). The set point values were inputted to the rheometer software (Rheology Advantage Instrument Control AR, TA Instruments, Newcastle, DE, US) which

commands the cup sample holder to heat or cool the sample. Pictures of the calibration system are presented in **Figure 3 - 2**.

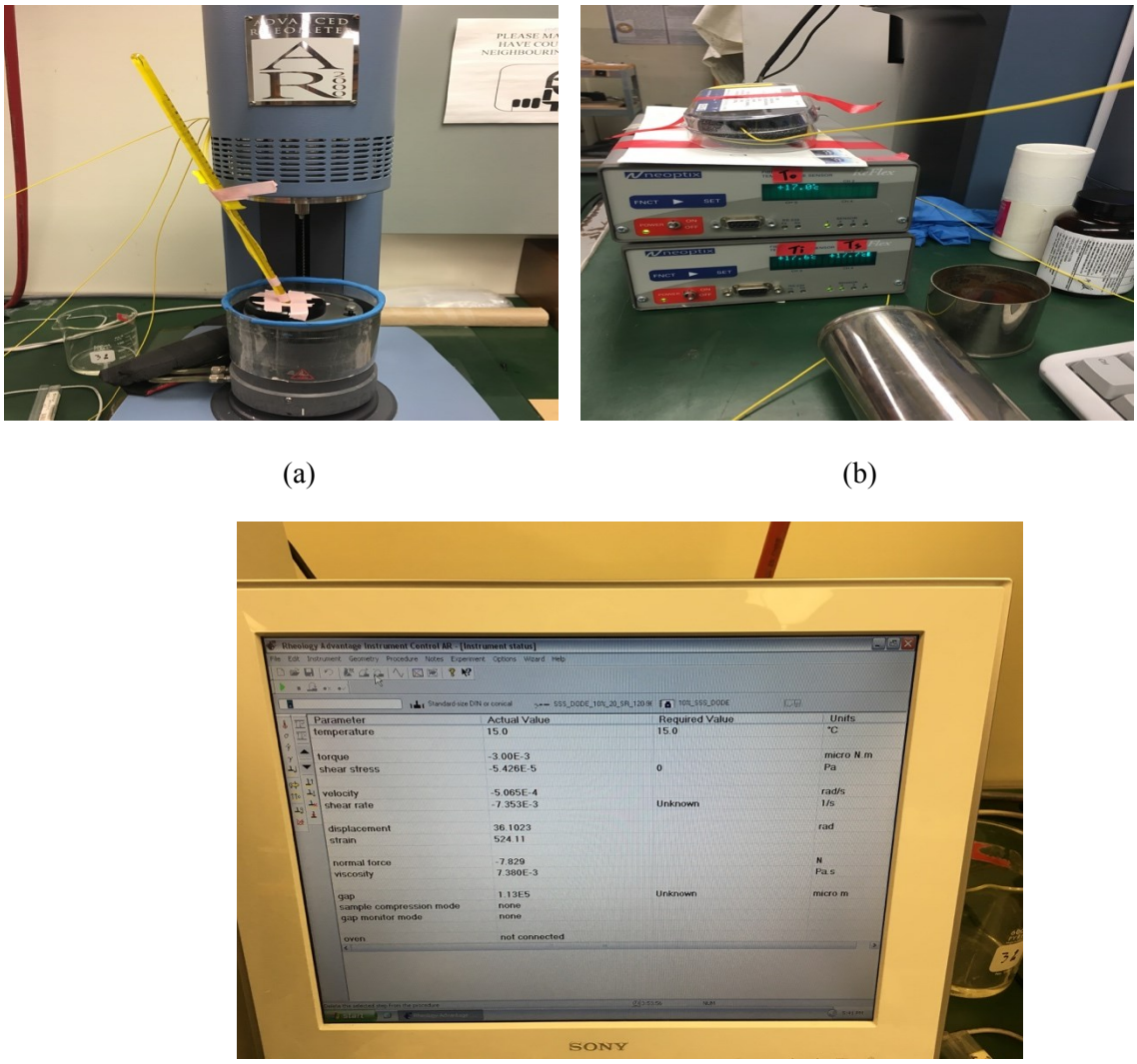

(a) (b)

(c)

Figure 3 - 2 Pictures of the calibration system, (a) is the rheometer itself with three FOTs and the standard thermometer inside the sample holder; (b) is the two Neoptix ReFlex reading boxes, the top of which was used to read the outlet temperature of the Galden, whereas the bottom one was reading the inlet temperature and the temperature of the sample; (c) shows the control interface of the rheometer software.

Household baby mineral oil (Johnson's) was used as the homogeneous fluid for the calibration. All the temperature readings were calibrated against the reading from the standard thermometer, at many oil temperature set-points. At each set point, 30 minutes

were allowed to stabilize the readings of all the devices, before taking measurements. The data recorded are listed in **Table 3 - 2** & **3 - 3.** Two calibration tests were conducted, but the readings of the thermistor were only recorded in the first test. The second test was run to check the reliability of the first test. However, the thermistor had already been installed in the temperature control system at that moment, so the second calibration test wasn't conducted for it. The correlation coefficients for the FOTs compared with the first and second tests were very close, therefore both tests were deemed reliable. The data from the second test were chosen to calibrate the FOTs because the date of the second test was much closer to the date of running the Rheo-NMR experiments.

Table 3 - 2 Collected data points of the thermistor and the standard thermometer from the first test

$T_{control}$ (°C)	T_{thmi} (°C)		T_{thm} (°C)	
trial	1	2	1	2
-5	-5.02	-4.80	-4.15	-4.35
0	0.22	0.21	0.60	0.50
5	5.25	5.21	5.60	5.45
10	10.24	10.23	10.50	10.45
15	15.22	15.21	15.40	15.25
20	20.21	20.22	20.20	20.20
25	25.26	25.21	25.10	25.10
30	30.30	30.23	29.95	30.00

Table 3 - 3 The collected data points of the FOTs and the standard thermometer from the second test

$T_{control}$ (°C)	To (°C)		Ti (°C)		Ts (°C)		T_{thm} (°C)	
trial	1	2	1	2	1	2	1	2
7.5	10.2	-	10.6	-	10.0	-	7.30	-
10.0	12.3	-	12.6	-	12.5	-	10.30	-
11.0	12.9	-	13.5	-	13.3	-	10.90	-
15.0	17.5	17.3	17.8	17.8	17.8	17.7	15.30	15.15
20.0	22.1	22.7	22.8	22.8	22.9	22.9	20.25	20.15
25.0	27.3	27.7	27.5	27.6	27.9	27.9	25.15	25.05
30.0	32.5	32.7	32.4	32.5	33.1	33.1	30.00	30.00

The calibration coefficients were obtained from linear trend lines in a plot of the temperatures from the standard thermometer (T_{thm}) as a function of the temperatures from other devices. The plot and the equations are shown in **Figure 3 - 3**.

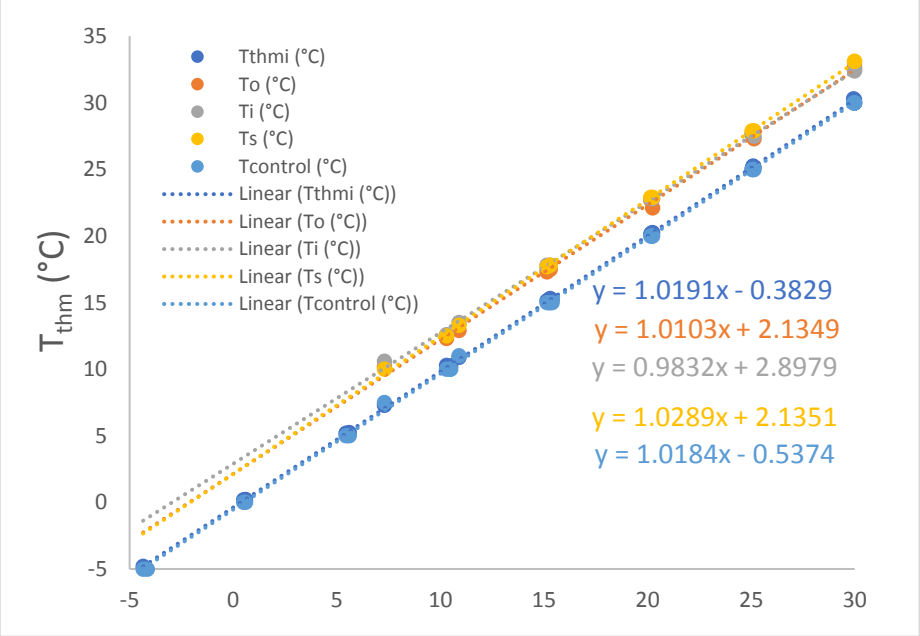

Figure 3 - 3 Temperature readings from the standard thermometer as a function of the readings from other devices. Their linear calibration functions are also shown.

3.2.2 Thermal Unit Configuration

The thermal unit, placed inside the NMR and around the glass tube-holder of the probe, was designed as part of the temperature control system. It was designed by Dr. Mazzanti and Tianguang Jia and printed out by Formlabs Incorporated.

The thermal unit was made of a standard resin. Although it's not heat resistant, it can still withstand temperatures of about 80 °C. **Figure 3 - 4** shows the configuration of the thermal unit and the picture of it taken when placed in the NMR probe.

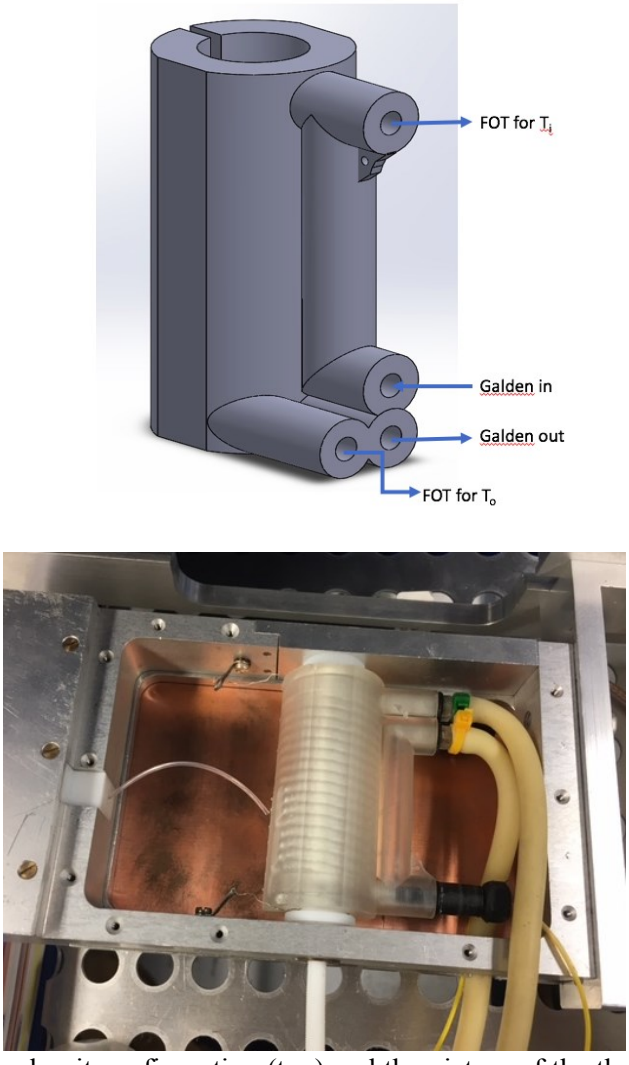

Figure 3 - 4 The thermal unit configuration (top) and the picture of the thermal unit in the NMR probe (bottom).

The big cylinder is hollow in the middle, to accommodate the glass tube-holder of the probe, with the four small cylinders protruding from it. Two small cylinders are for the inlet (yellow clamp) and the outlet (green clamp) of the fluid. The other two are for the measurement of corresponding temperatures using FOTs. There are two anti-parallel fluid channels coiling inside the big cylinder, within the space between the inner and the outside wall. The details can be seen in the pictures above.

3.2.3 Temperature Control System

In the previous work of our lab, a well-designed temperature control system was built for both Rheo-NMR and Rheo-Xray experiments ((Li 2011, Wang, Johnson et al. 2012, Deng 2014), which was first designed and described by Mudge and Mazzanti (2009).

The temperature control system used in this research consists of a temperature controller (5R001, Oven Industries Inc., Camp Hill, PA, US), a water bath (R6L, polystat®, Cole-Parmer®, Montreal, QC, Canada), an active heat exchanger, a Galden reservoir, a peristaltic pump (Cole-Parmer Instrument Company®, Model: 77800-50, Masterflex® Tubing Pump) for Galden fluid, a thermistor (Oven Industries Inc., Camp Hill, PA, US), and three fiber optic temperature sensors (Neoptix® Fiber Optic Temperature Sensor Models T1 and T2).

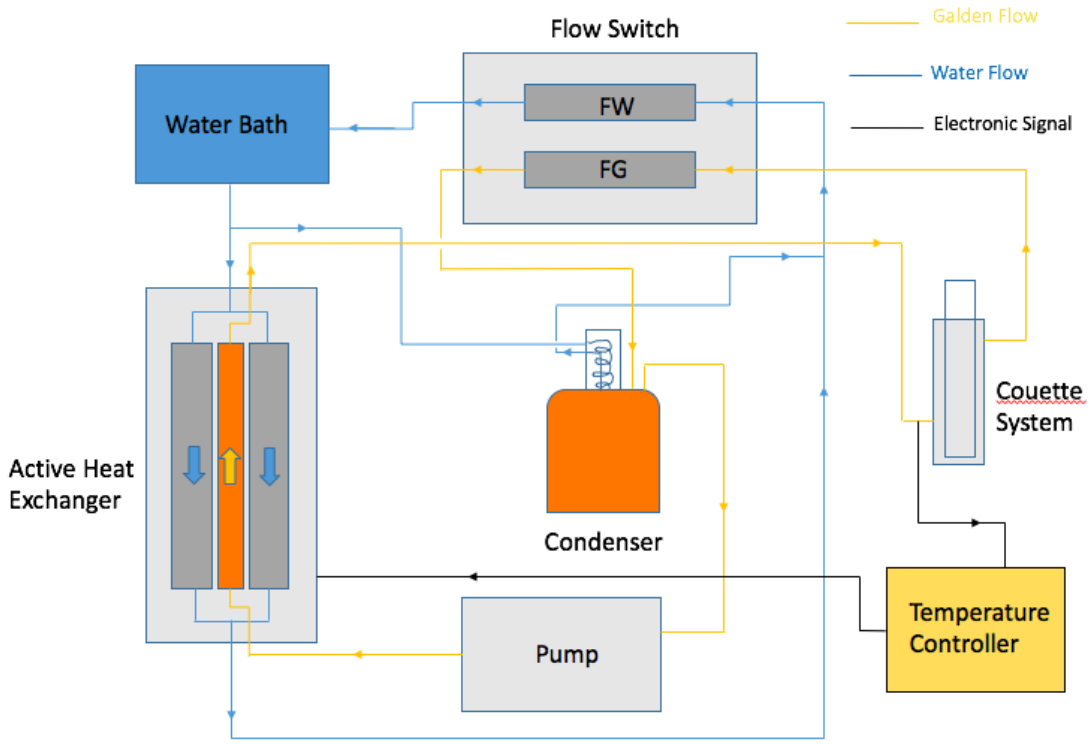

Figure 3 - 5 Schematic of the temperature control system configuration.

Temperature Controller

The temperature controller was connected to a computer so that its proprietary software, "CONTROLLER MR001", could be used to directly control the temperature measured from the thermistor. Additionally, a more complicated LabView program was composed to control the other temperatures, such as the sample temperature, the inlet Galden temperature, and the outlet Galden temperature. The temperature controller was not able to control the temperature very accurately; however, the controlled temperature was precise, and close to the set point when the system stabilized.

Water Bath

The water fluid was connected to the heat exchanger to act as a heat sink or source for the active heat exchanger. The temperature of the water bath was set to 5 °C to provide a heat sink to control low temperatures. The water used in this work was pure water to prevent corrosion.

Active Heat Exchanger

The active heat exchanger was connected to the temperature controller. It was built in-house, with three thermoelectric elements (Model: HT8-12-F2-4040-TA-RTW6, Laird Technologies, Cleveland, OH, US) used to precisely control temperature, by transferring heat between the Galden and water fluids. These thermoelectric elements are assembled with Bismuth Telluride semiconductor material and thermally conductive Aluminum Oxide ceramics (Wright, Hartel et al. 2000). In this work, they were connected in parallel to a 24 V modulated power supply. Depending on the direction of the DC current applied, the thermoelectric elements can transfer heat in both directions, by cooling one of their sides and warming up the opposite. The magnitude of the current is a function of the applied voltage, which is controlled by the modulated power supply using a PID algorithm.

Galden Heat Transfer Fluid System

The Galden fluid was kept in a stainless-steel thermos, with a glass condenser mounted on top to avoid evaporation of the Galden or pressurization of the system. The Galden fluid, which was pumped with a peristaltic pump at a constant flow rate of 160 mL/min, started from the container, then went through the heat exchanger and finally reached the thermal unit. After the thermal unit, it went back to the thermos container again

for recirculation. The tubing between the heat exchanger and the thermal unit was insulated to avoid energy losses to the environment. The thermistor was located right after the exit of the Galden fluid from the heat exchanger, to measure the Galden temperature by providing its signal to the temperature controller.

Fiber Optic Temperature Sensor

The fiber optic temperature sensors were chosen as the temperature measuring devices simply for three reasons. Firstly, there's no metal part in the sensor which means there's no electrical power running through it, either fed or induced. This is necessary inside of the NMR probe, where the strong magnetic field, and especially the RF field, would strongly interact with any metal parts. Secondly, since they are small in size, they could be connected to the thermal unit and installed in the NMR probe. Also, the measured data could be recorded directly in the computer by converting the received signal to temperature (0 - 100 °C). Two types of electronic devices were used in this research to read the FOTs. The only difference between them was the number of channels and their analog outputs. One sent a voltage signal (0 - 10 V) to the computer interface, whereas the other sent a current signal (4 - 20 mA).

Couette Cell System

Both static and dynamic experiments were done in a Couette system. It consists of the thermal unit and a glass tube with inside and outside diameters measured at 11.4 mm and 13 mm respectively. The Galden fluid went through the thermal unit to cool or heat the sample fluid, as needed. The shaft of the measuring head, which is driven by the rheometer

motor, rotated to provide a uniform shear to the sample fluid in the gap between the shaft and the glass tube.

3.3 Nuclear Magnetic Resonance Measurement

The current Rheo-NMR system, which was firstly designed by Dr. Mazzanti and used by Mengyu Li, was built up for this research and the ones in the future at Dalhousie University. A modified IBM-Bruker mq20 NMR Analyzer (the minispec), with a 30 mm magnet gap, was used to run automatic measurements. This NMR device works at 20 MHz (0.47 T corresponds to the resonance of ^{1}H at 20 MHz), and it analyzes the sample by beaming programmable radiofrequency pulses to the material, examining the resulting NMR signal in the sample, and displaying the calculated quantity of interest to the user.

3.3.1 Rheo-NMR System Configuration

The Rheo-NMR system consists of the low-field table-top NMR instrument and a rheometer on top of the NMR. By setting up this system, the spin-spin relaxation times (T_2) of the sample and the rheological information of the sample could be measured simultaneously during the experiments. Pictures of the Rheo-NMR system are shown in **Figure 3 - 6**.

As seen in the pictures below, an absolute probe was fixed between two magnets with a hole in the middle to hold the sample tube. A 13-mm glass tube was put into that hole with the Galden fluid flowing through the surroundings of the probe.

Figure 3 - 6 Pictures of the NMR device taken before installing the rheometer (top) and the picture of the Rheo-NMR system used for this work (bottom).

The schematic diagram of the Couette system in Rheo-NMR is shown in **Figure 3 - 7**.

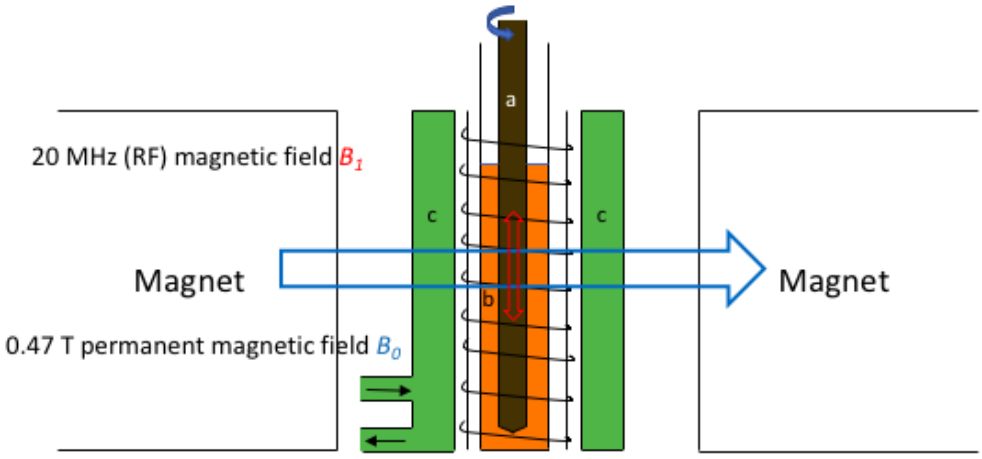

Figure 3 - 7 The schematic diagram of the Couette system in the Rheo-NMR system that was presented in the introduction. **a** is the rheometer shaft, **b** is the sample N1000 and **c** is the thermal unit through which the Galden fluid flows for temperature control.

Before moving the shaft to the proper place in the glass tube, it's important to make sure that the shaft and the glass tube are concentric, or at least they are parallel to each other. Otherwise, the shaft is likely to hit the wall of the glass tube which would result in the break of the glass tube or, even worse, the break of the NMR probe while moving the shaft into the glass tube or running at high shear rates. The shaft was connected to the measuring head, keeping the compressed air open all the time, to center it and make it rotate. The measuring head was sitting on trestles and controlled by three motors which could move the whole structure vertically by a software called Zaber Console (Zaber Technologies Inc., Vancouver, BC, Canada), as shown in **Figure 3 - 8**, and horizontally by hand or a portable computer (TANDY 102, Tandy Radio Shack, Fort Worth, Texas, US). Hence, the position of the measuring head can be adjusted precisely by this three-dimension stage.

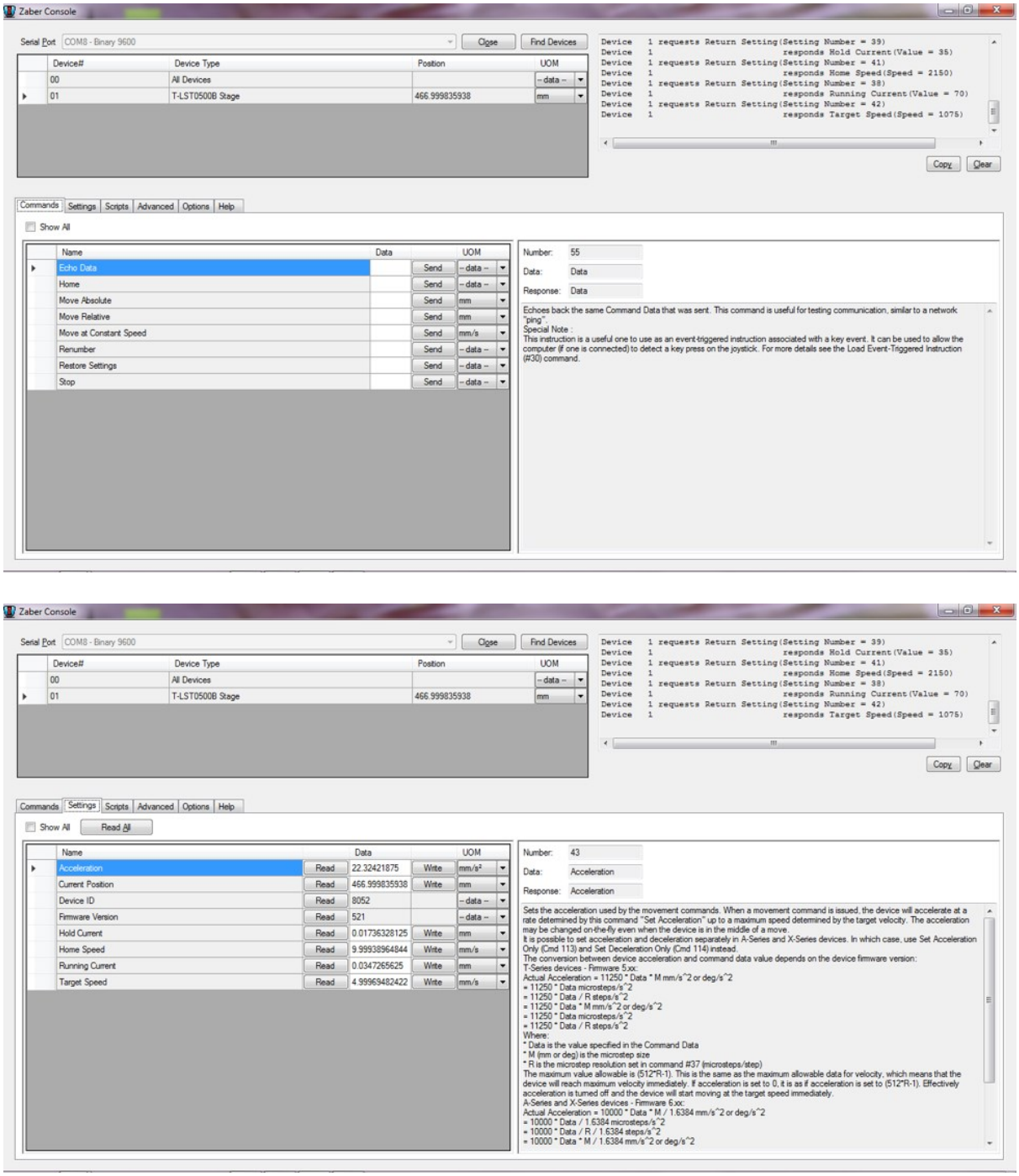

Figure 3 - 8 The pictures of the control panel of Zaber Console.

The ‘current position’ shown in the second picture was the relative position compared to the home one. The home position is the highest place the measuring head can reach, and it reads zero at that position. Both ‘move absolute’ and ‘move relative’ are used

as the commands to control the measuring head up or down, but a negative number is not allowed. The best position of the shaft was tested to be at 467 mm where the shaft was very close (less than 1 mm) to the bottom of the glass tube. It was implemented as the position of the shaft for all the experiments.

3.3.2 Rheo-NMR Calibrations

There are several calibrations that need to be done before running any sample. The calibration of the temperature control devices has been discussed in the previous section. NMR calibration is necessary when the probe is changed or different samples are used. To get a reasonable range of signal strength, the device should be properly adjusted. Also, the rheometer needs to be calibrated to obtain accurate data.

3.3.2.1 NMR Calibration

Two types of calibrations are performed for the NMR instrument. The first one is called the ‘instrument calibration’ which is specific for different probes. It can be carried out by clicking ‘Update Settings’ command, after that all the updated settings will be saved in the instrument table.

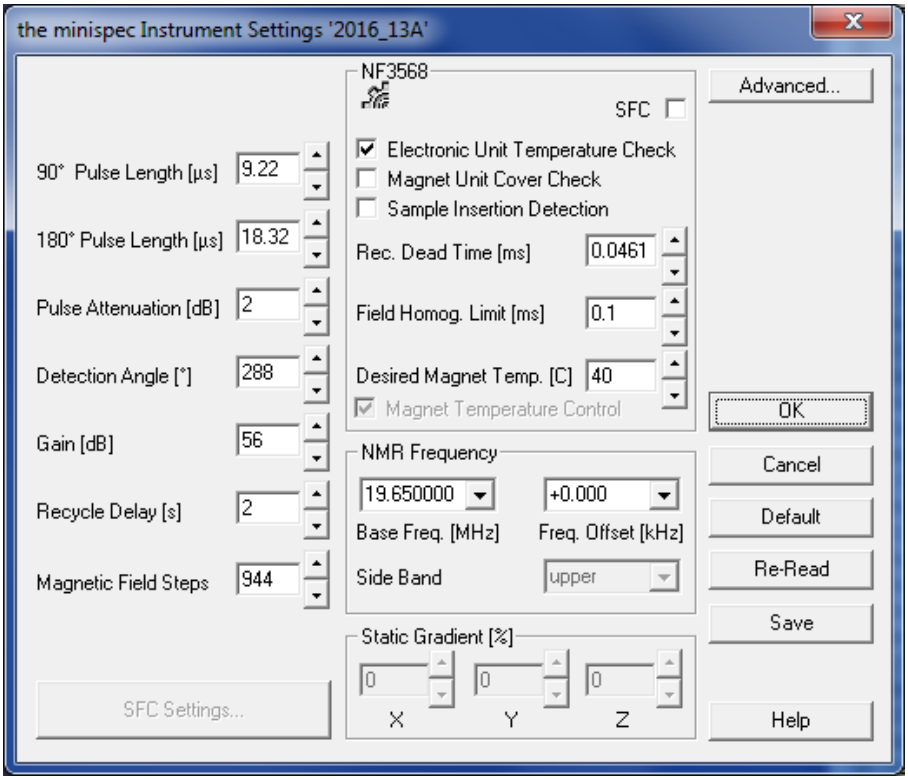

Figure 3 - 9 The table of the minispec instrument settings for the absolute probe used in this research.

Another calibration should be carried out if different samples are used. This calibration aims at changing the measurement parameters to obtain a signal strength in a reasonable range. To do so, the temperature of the sample should be kept close to the magnet temperature, which is around 40 °C, and then the parameters can be adjusted to make the signal intensity reach approximately 80% of its range.

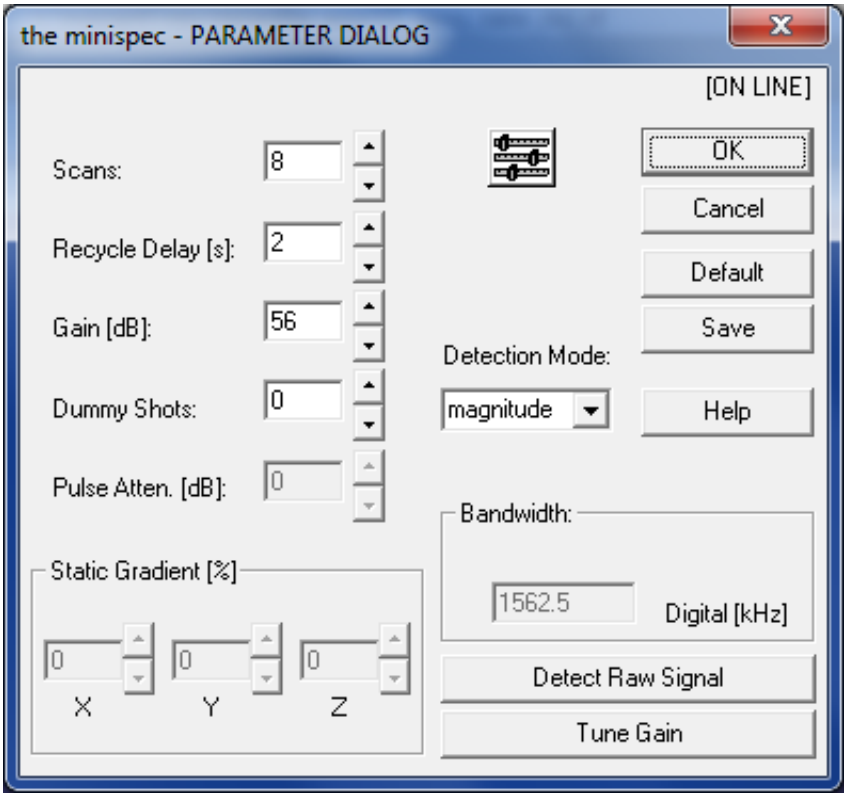

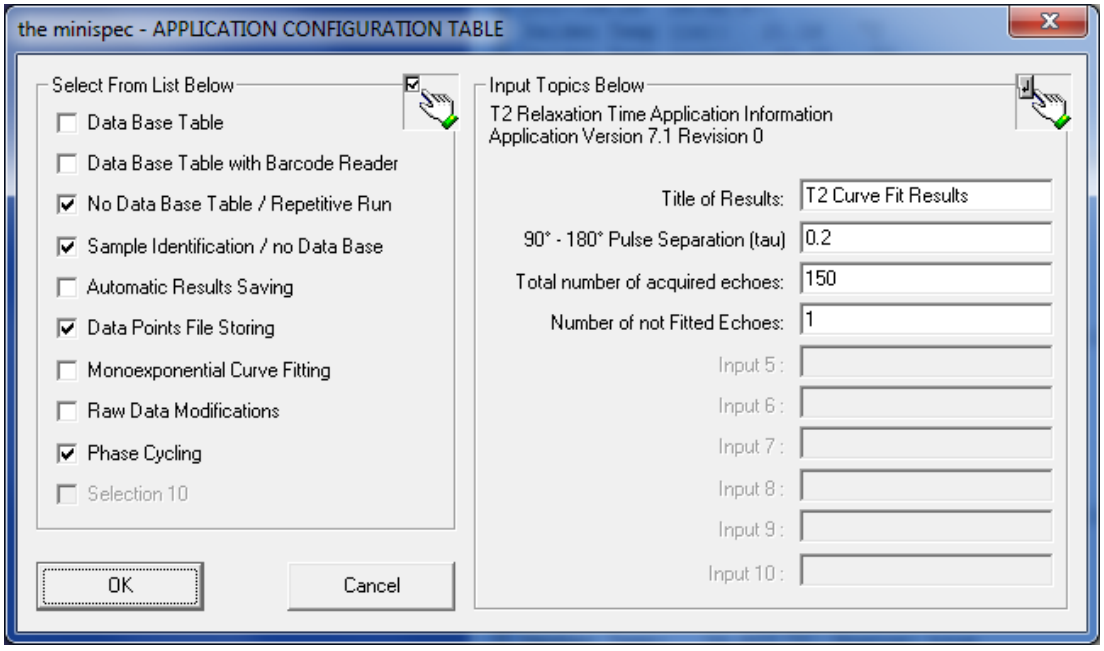

Figure 3 - 10 The minispec parameter dialog table (the first picture) and the application configuration table (the second picture).

All these settings were kept constant for all the experiments done within this research. However, some settings were adjusted after the relationship between T_2 and temperatures was confirmed. 'Scans' is the number of repetitive scans within a single run, and 'Recycle Delay' is the time interval between two scans. Since T_2 relaxation times and amplitudes measured by NMR are the averages of the values from each scan, a delay time is necessary to make sure all the nuclear spins return to the original equilibrium. Both parameters are very important and play a vital role in obtaining accurate results. A proper setting of gain is also necessary because it will affect the amplitude intensity. If gain is set too high, the signal will overload the analog-to-digital converter, and data clipping will occur. These three parameters can be tuned to optimize the time needed for a single run, and the precision of the results.

It should be mentioned that the initial 90° - 180° pulse separation (0.2 ms) cannot be adjusted if the relationship between T_2 and temperatures obtained in this work is to be used to predict temperatures in other NMR instruments. That is because it was observed that T_2 increased with the increase of the 90° - 180° pulse separation. This obviously requires further investigation, since measurements of T_2 should be relatively independent of variations in τ.

The interface of the minispec software is shown in **Figure 3 - 11**. The window at the left is the amplitude intensity graph, the window in the middle is to collect data, and the window at the right is the status box which is used to check if everything's all right to run experiments.

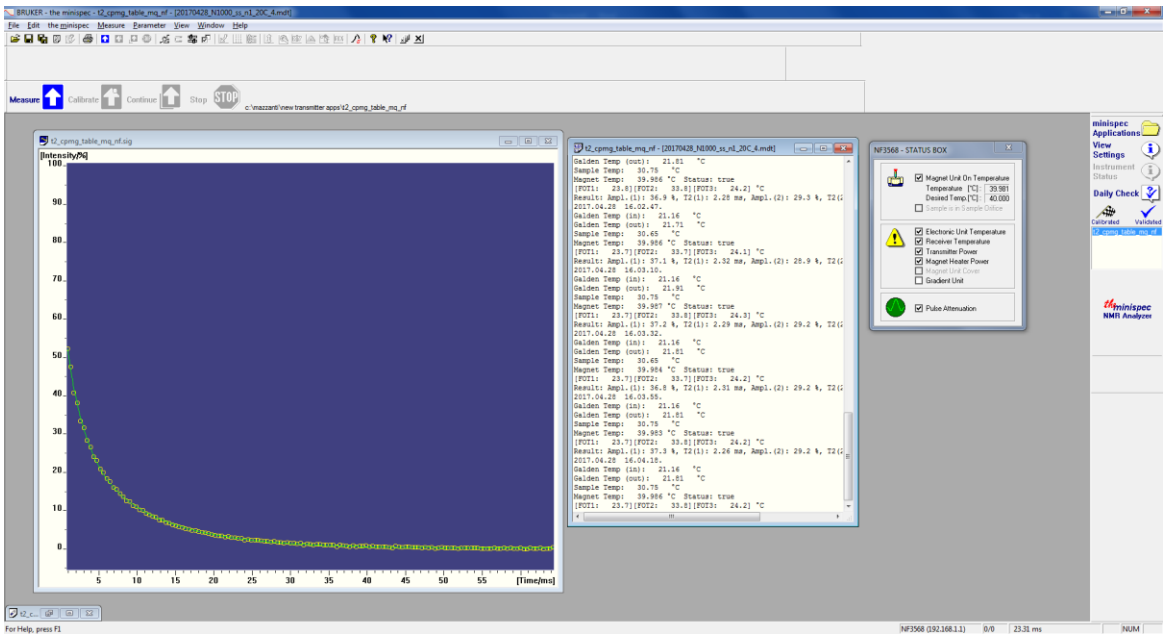

Figure 3 - 11 The interface of the minispec software.

3.3.2.2 Rheometer Calibration

The rheometer is controlled by the software RheoPlus (Anton Paar, Ashland, VA, US), that was a setup option 'Change Measuring System' as shown in **Figure 3 - 12**. In this research, RH-NMR-SN004 was chosen as the measuring system, and the Mooney-Ewart geometry for a cylinder was used to calculate the C_{ss} and C_{sr} values. These values are used to convert the torque into shear stress, and the rotational speed into shear rate. Several parameters were required by the system to calculate the values, such as Length Cylinder Part, Ra, and Ri. Length Cylinder Part is the height of the sample in the tube with the shaft in it (69.81 mm), Ra is the inner radius of the 13-mm glass (r_i = 5.7 mm) tube and Ri is the radius of the shaft (r_s = 4.5 mm). The three values mentioned above were carefully measured by a caliper and placed in the corresponding software entries.

To understand how the system works, the equation used to calculate C_{ss} was investigated. The problem was that the equation for C_{ss} in the system couldn't be found anywhere, either in the manual or from the manufacturer. So, the Mooney-Ewart equation accounting for end effect (Rao 2014) was applied to this case.

$$C_{ss} = \frac{1}{2\pi r_{eq}^2 (c_L + \frac{req}{3\sin\alpha})} \tag{32}$$

$$r_{eq}^2 = \frac{2r_i^2 r_s^2}{r_i^2 + r_s^2} \tag{33}$$

where c_L is the length cylinder part and α is the angle of the cone part of the shaft, which was 45°.

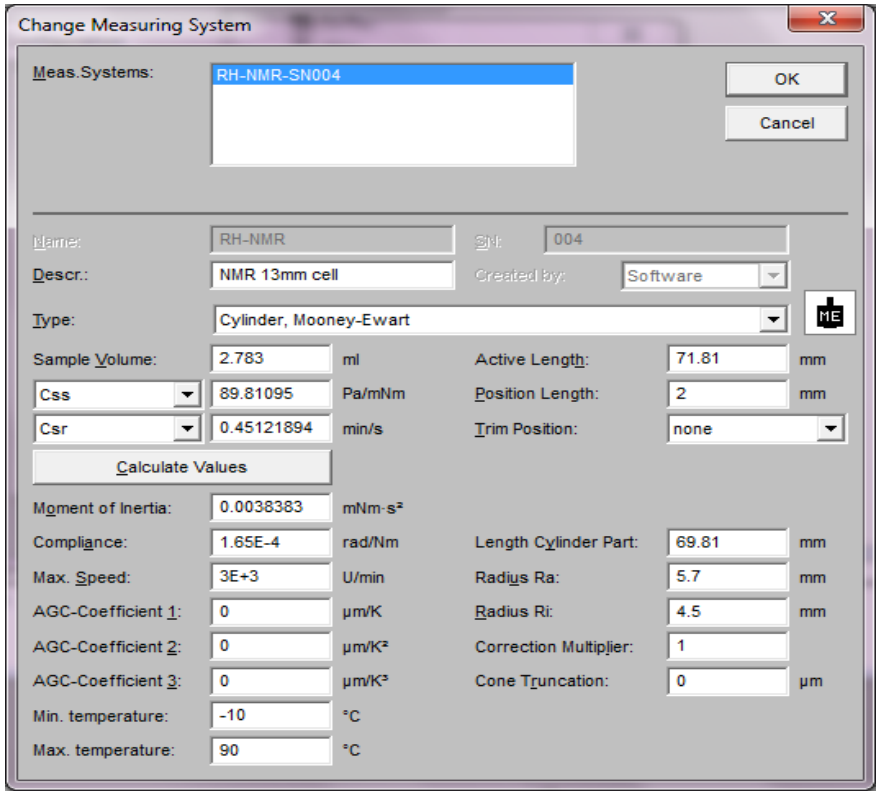

Figure 3 - 12 User interface for RheoPlus 'Change Measuring System' displaying the calculation parameters.

The C_{SS} value calculated from equation (32) and (33), using the same parameters as shown in **Figure 3 - 12**, was 88.39442. Compared with the value 89.81095 from the system, the error was within 1.58%. Therefore, the equations above were assumed to be close enough to the ones used in RheoPlus and were kept for future calculations.

3.3.3 Experimental Procedure

The experiments were divided into two sections. One was done under static conditions, which means the sample was kept at a relatively stable temperature without shear applied to it. The sample temperatures and T_2 relaxation times could be measured and recorded simultaneously by the FOT placed in the sample and the NMR minispec software respectively. By running the experiments at various temperatures, it could be observed how T_2 of the sample changed with the sample temperature. Then, a correlation between T_2 and the sample temperature was built, to predict the sample temperature under shear conditions. The second section was to run the experiments at different rotational speeds and to use measured T_2 to estimate the sample temperature in the glass tube. The hypothesis was that, because of viscous heat generated, a temperature increase would be observed, compared to the temperature measured under static conditions. Additionally, the experimental data could be compared with the quantitative theoretical temperature calculated from Wang's model.

3.3.3.1 Static Experiments

To study if the shaft affects the results, two types of static experiments were carried out. The first one was done by running the static experiments without the shaft inside the glass tube. The other static experiment was done by placing the shaft at the same position (467 mm) as in the shear experiments. Hence, two 13-mm glass tubes with different heights of sample, the heights of which were 71.8 mm and 28.3 mm respectively, were prepared for each type of experiments. Regardless of the sample height, other procedures were the same for both shaft-in and shaft-out experiments.

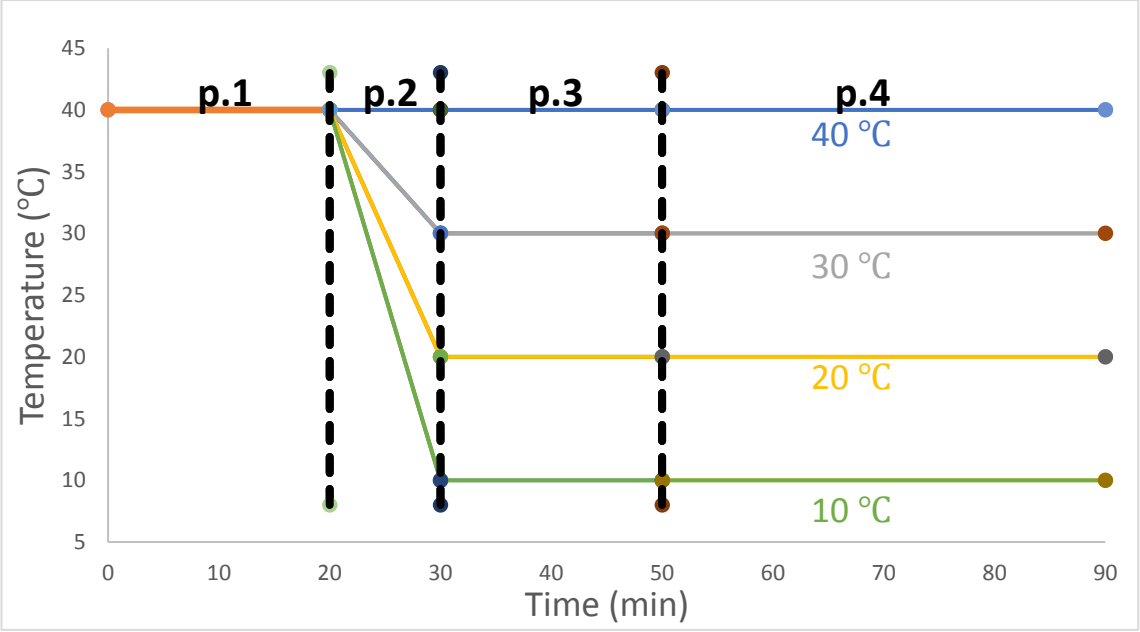

Figure 3 - 13 The procedure diagram of the static experiments at the sample temperatures of ~10, 20, 30, and 40 °C.

As shown above, the sample was initially kept at the magnet temperature 40 °C for 20 min to make the sample temperature homogeneous inside the glass tube (p.1). The sample was then cooled down by the temperature control system and was kept at around

10, 20, 30, and 40 °C (p.2). When the sample temperature was stable for 20 min, the NMR minispec software started to measure T_2 (p.3). Each run took about 20 seconds and the time interval (delay) between two repetitive measurements was set to be 2 seconds. In total 100 runs were measured at each temperature (p.4). Each experiment was repeated twice to assess the variability between trials.

3.3.3.2 Shear Experiments

It was expected that the viscous heat generated during the shear experiments would increase as the rotational frequency was raised, or as the Galden temperature was reduced. The rotational speeds applied were 0.1, 1, 10, 30, and 50 revolutions per second (rps). The nominal inlet temperature of the Galden was set to be 20, 30 and 40 °C for this research. The room temperature was between 23 °C and 28 °C when carrying out the experiments. The NMR signals and the rheological data were collected at the same time and recorded by the minispec software and the RheoPlus software respectively. Since one of the purposes of this work is to compare the temperature difference under static and shear conditions which is caused by viscous heat generated, the experiments were implemented following a static-shear-static-shear sequence, as shown in **Figure 3 - 14**. The detailed procedures are listed below:

1. Let the inlet temperature of the Galden fluid stabilize at a specific temperature range for 20 min, and then start collecting 20 sets of data.
2. Start shearing for 20 mins, and then collect 20 sets of data again.
3. Stop the shear and repeat the first step.

4. Repeat the second step.

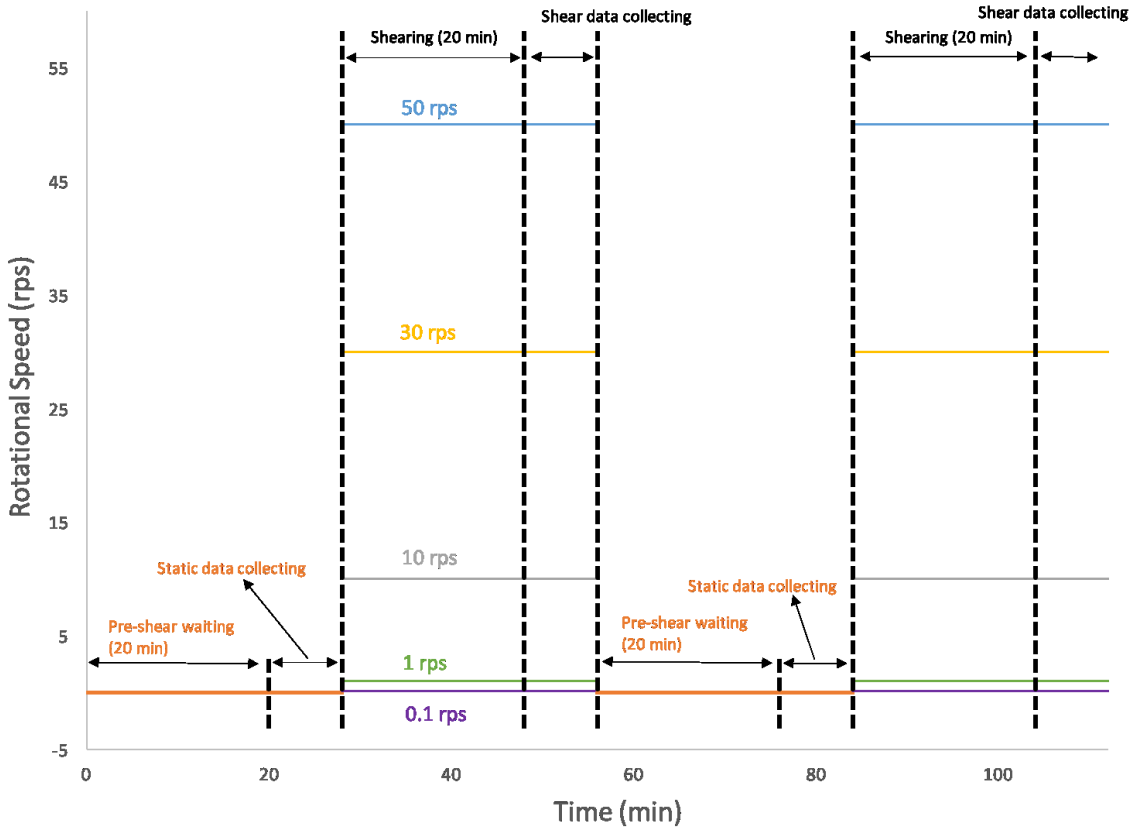

Figure 3 - 14 The procedure diagram of the shear experiments at the inlet temperatures of ~20, 30, and 40 °C.

3.3.4 Data Collection

The original data sets of NMR signals and temperature profiles were saved by the minispec software as text files. The rheological data were saved, in a proprietary format, by the RheoPlus software, which controls the measuring head. The data recorded in RheoPlus were: the interval time in unit s and the viscosity in unit mPa·s. All the data were then imported into Microsoft Office Excel, where further analysis was carried out.

CHAPTER 4 RESULTS AND DISCUSSION — I — EXPERIMENTS UNDER STATIC CONDITIONS

4.1 Correlation between T_2 and the Sample Temperature with the Shaft inside the Glass Tube

These experiments were done with the shaft inside the glass tube. The intensities of every data point for each run were saved by the minispec software. Then, they were imported into the Excel and plotted as a function of time.

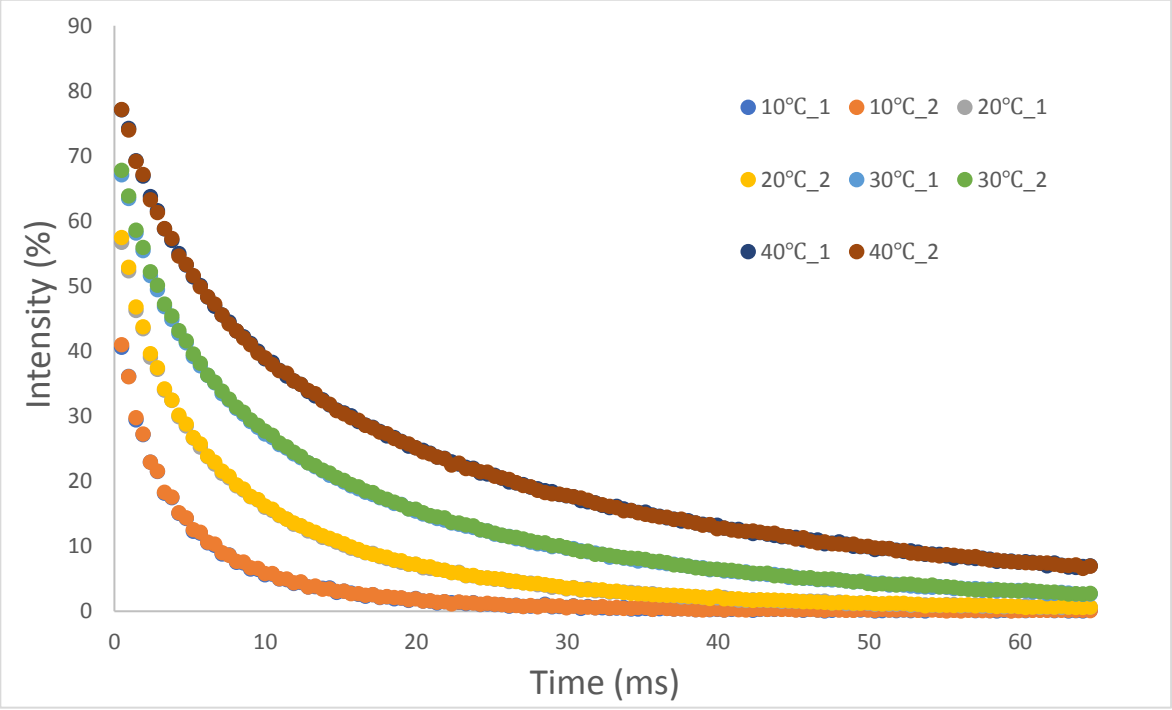

Figure 4 - 1 Intensity of NMR echoes vs. time, at different setpoint temperatures: 10, 20, 30, and 40 °C. The experiments were done twice for each temperature, with the shaft inside.

The temperatures shown in **Figure 4 - 1** are the set points, which refer to the target temperatures for the sample in the static experiments. It is apparent that the intensity is dimmed with the decrease of the temperature.

In order to obtain the T_2 relaxation times and their amplitudes, an extension of the mono-exponential equation (6) was fitted to the data shown in **Figure 4 - 1**. This bi-exponential decay function provided and excellent fit to the echo-decay data, whereas the single exponential function did not. The equation is shown below,

$$M_{xy}(t) = M_{xy\_1}(0)e^{-t/T_{2\_1}} + M_{xy\_2}(0)e^{-t/T_{2\_2}} \quad (34)$$

where $M_{xy\_1}(0)$ and $M_{xy\_2}(0)$, expressed in this thesis as Ampl_1 and Ampl_2 respectively, are the amplitudes of component 1 and 2 at time zero, whereas T_{2_1} and T_{2_2} are the relaxation times of component 1 and 2. The meaning of the two T_2 values of is discussed later.

The equation was programmed in the minispec software. When running at different set points, the T_2 relaxation times, the amplitudes, as well as the sample temperature were recorded for each run by the modified minispec software and analyzed in Excel. **Figure 4 - 2** shows the plot with all the data points and their corresponding polynomial trendlines.

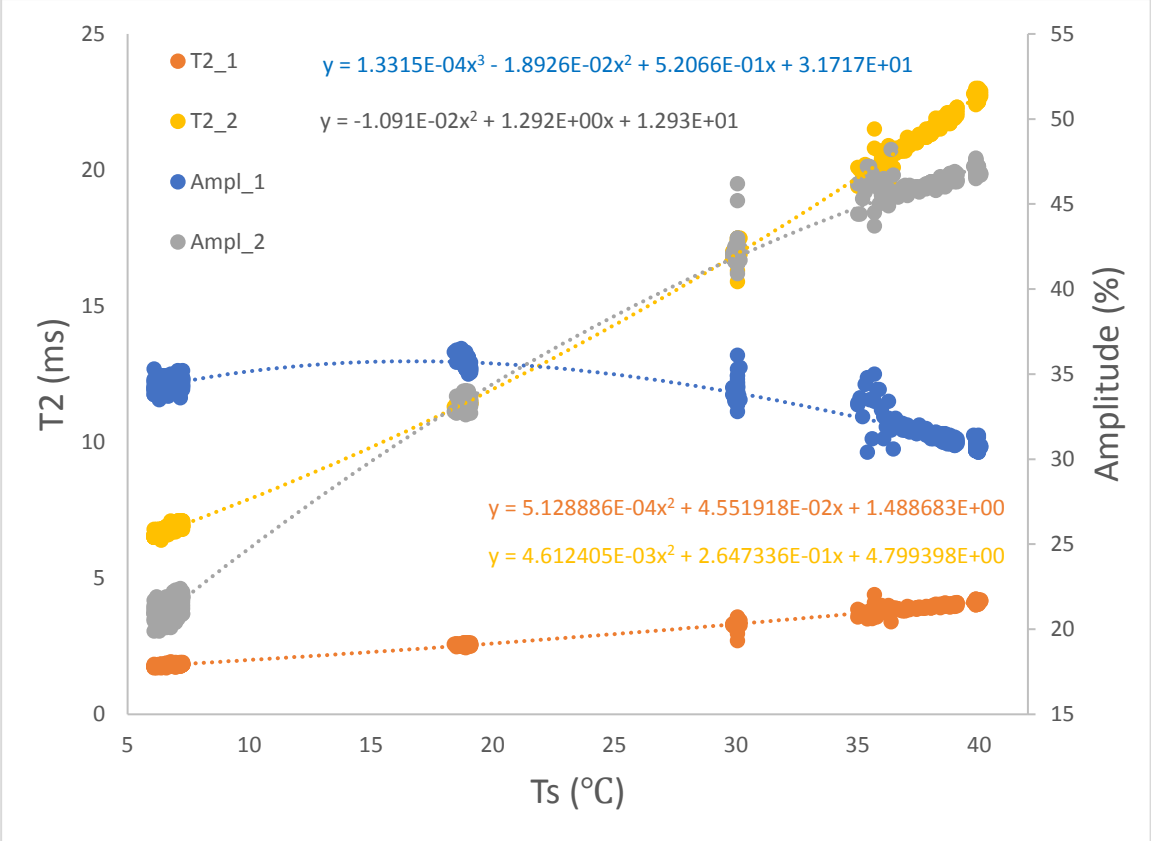

Figure 4 - 2 The measured T_2 relaxation times and amplitudes* as a function of the sample temperature with shaft inside, together with the corresponding trendlines. Ampl_1 and Ampl_2 are the amplitudes of component 1 and 2 at time zero, whereas T_{2_1} and T_{2_2} are the relaxation times of component 1 and 2. (Note: the amplitudes are proportional to the amplitude of the reference that was used to calibrate the NMR)

Both T_{2_1} and T_{2_2} followed almost linear trends, increasing with the temperature, as expected. The positive trend was expected, since at high temperatures the correlation times decrease, and thus T_2 increases, as presented in the literature review (Callaghan 1993). Polynomial trendlines were used to obtain more precise results.

The data points measured for amplitudes are more scattered than the data for T_{2_1} and T_{2_2}. The total amplitude increased with temperature, as shown in **Figure 4 - 3**. However, the number of unpaired protons decreases with temperature, from 2.18 to 1.82

aligned protons for each 10^5 total protons. That would mean a reduction in signal to 89% of the signal at 5 °C when heating to 40 °C.

$$\frac{N_{high}}{N_{low}} = e^{-\gamma B_o h / k_B T} \quad (1)$$

γ	2.68×10^{8}	rad/(T·s)	Hydrogen gyromagnetic ratio
B_o	0.47	T	External field
h	6.63×10^{-34}	J·s	Planck's constant
k_B	1.38×10^{-23}	J/K	Boltzmann's constant

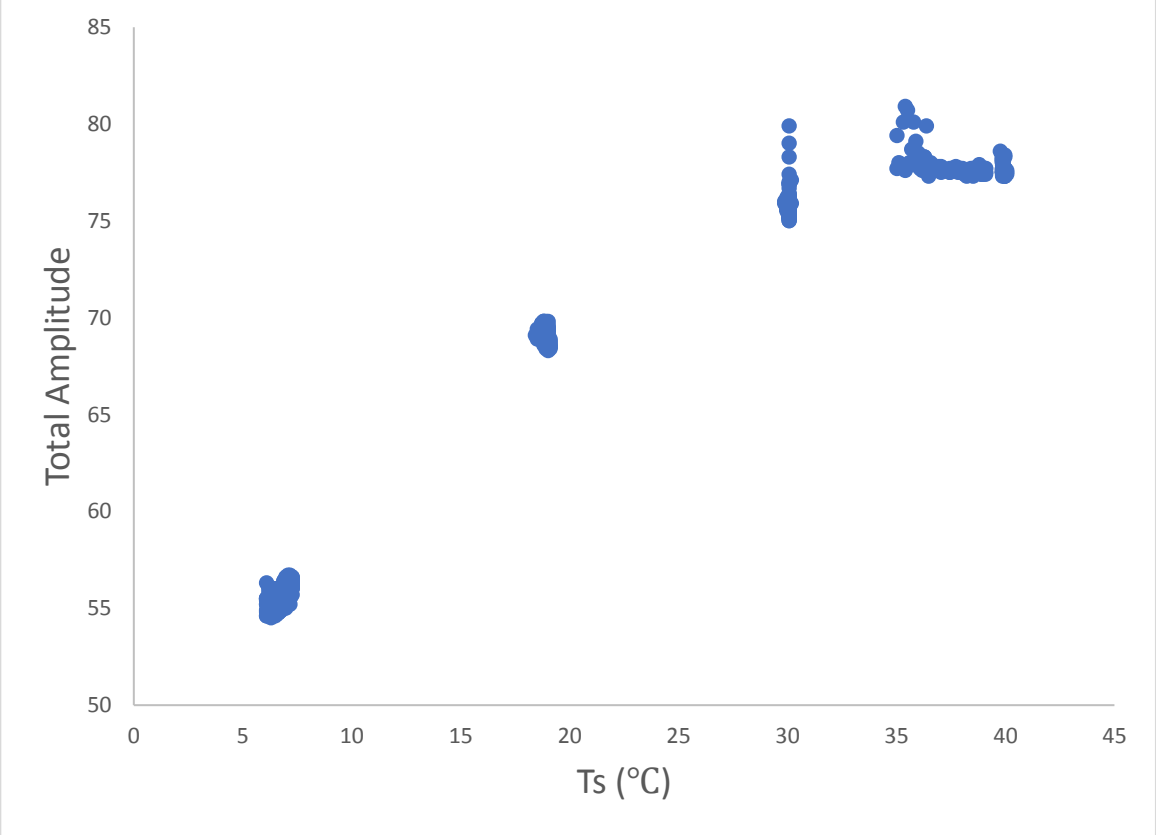

Figure 4 - 3 The total amplitude as a function of the sample temperature with shaft inside.

On top of that, the density decreases slightly with increasing temperature, thus the total number of protons of the sample in the measuring volume decreases as well. The combined effect of the distribution function and the density would reduce the intensity at

40 °C to 87% of the signal received at 5 °C. Yet the total intensity decreases as temperature decreases, so that at 5 °C the intensity is 75% of the intensity measured at 40 °C. That means that another effect, much stronger than the density and distribution function together, is causing the decrease in signal. This effect on the total amplitude very likely comes from the temperature of the coil, since it is placed inside of the cooling system. At a lower temperature, the resistance of the coil and its effective length decrease slightly. The RLC circuit will therefore have its resonant frequency shifted from the precisely calibrated one at 40 °C (19.94 MHz). This will cause the coil to pick up less intensity. For future work, the coil can be tuned at the temperature of the cooling system.

The distribution of the total amplitude was not simple, however. Amplitude Amp_1 did not show a monotonic growth. It slowly increased until the sample temperature approaches 19 °C, and then began to drop. A third order polynomial was fitted to the Amp_1 data. Amp_2 was increasing, and was described by a second order polynomial.

The four correlations could be used to estimate the T_2 relaxation times and amplitudes at a specific sample temperature, and vice versa. However, amplitudes are not only related to the temperatures, but also the sample volume, gain value and even temperature of the coil. That means these quantities are not directly applicable to other experiments unless they use the identical parameters and sample volumes as the ones in this research. To solve this problem, the ratio between Ampl_2 and the sum of Ampl_1 and Ampl_2, which was presented as A2/(A2+A1), was introduced in this method. The ratio between the two amplitudes is independent of the sample volume and the gain value. This is because the proportion of components 1 and 2 is fixed for the sample at a given temperature. The calculated results are shown in **Table 4 - 1**. A1 and A2 were calculated from the correlations in **Figure 4 - 2**, for temperatures from 0 °C to 45 °C.

Then the calculated A2/(A2+A1) data points were plotted versus the sample temperature to obtain the correlation equation of them, as shown in **Figure 4 - 4**. The experimental data were also plotted in that graph to see if there's a discrepancy between the two data sets. Obviously, the experimental data are highly following the same trend of the calculated ones with most of the data points located on or close to the trendline.

Table 4 - 1 The values of A1, A2, and A2/(A2+A1) determined from the correlations (with shaft).

T (℃)	T (K)	A1	A2	Ampl_Tot	A2/(A2+A1)
0	273	31.7	12.9	44.6	0.290
5	278	33.9	19.1	53.0	0.361
10	283	35.2	24.8	59.9	0.413
15	288	35.7	29.9	65.6	0.455
20	293	35.6	34.4	70.0	0.491
25	298	35.0	38.4	73.4	0.523
30	303	33.9	41.9	75.8	0.553
35	308	32.5	44.8	77.2	0.580
40	313	30.8	47.2	77.9	0.605
45	318	29.0	49.0	77.9	0.628

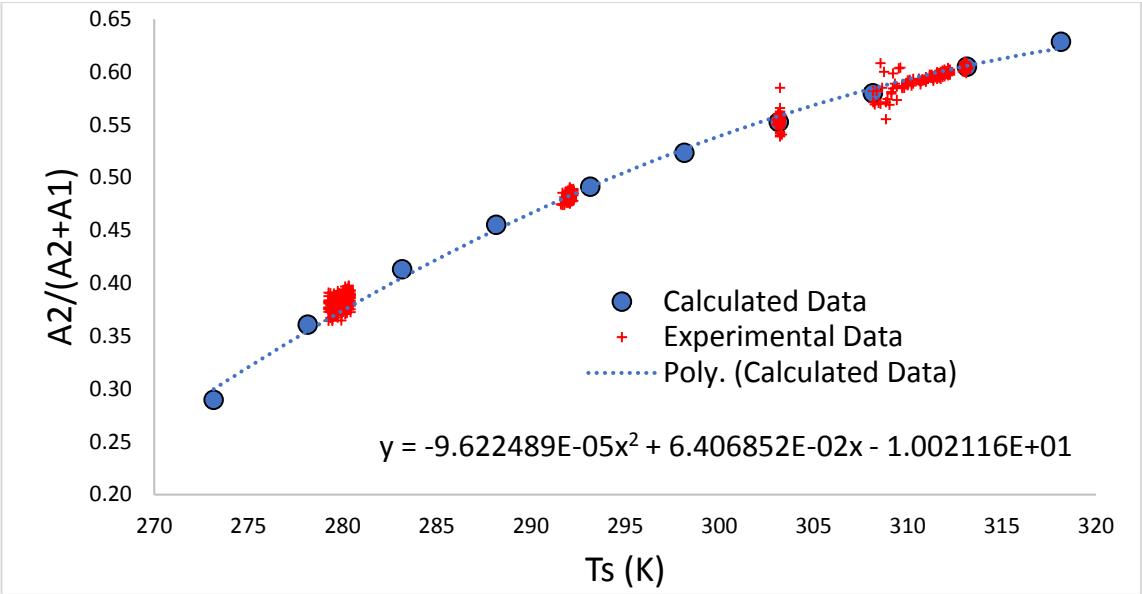

Figure 4 - 4 The calculated and experimental A2/(A2+A1) as a function of the sample temperature in K, with the shaft inside the sample tube. The trendline was added to the calculated data and the equation was displayed in the graph.

The correlation equations for T_{2_1}, T_{2_2}, and A2/(A2+A1) are the ones below, and the unit of T_s for T_{2_1} and T_{2_2} is °C, whereas the unit of T_s for A2/(A2+A1) is K.

$$T_{2\_1} = 5.128886 \times 10^{-4} T_s^2 + 4.551918 \times 10^{-2} T_s + 1.488683 \quad (35)$$

$$T_{2\_2} = 4.612405 \times 10^{-3} T_s^2 + 2.647336 \times 10^{-1} T_s + 4.799398 \quad (36)$$

$$\mathrm{A2/(A2+A1)} = -9.622489 \times 10^{-5} T_s^2 + 6.406852 \times 10^{-2} T_s - 10.02116 \quad (37)$$

According to the equations, the measured T_{2_1}, T_{2_2}, and A2/(A2+A1) of each run could be plugged into the formulas to calculate the corresponding T_s, and the calculated T_s were compared with the measured ones to see the discrepancies. The standard deviations of the differences were then calculated, as shown in **Table 4 - 2**. The function in (37) has a maximum at 59.8 °C, which is outside the range of measured temperatures.

Table 4 - 2 The calculated values of standard deviation (σ), 1/σ and weight by using T_{2_1}, T_{2_2} and A2/(A2+A1) respectively (with shaft).

	T_{2_1}	T_{2_2}	A2/(A2+A1)
Standard Deviation (σ)	0.835	0.286	0.949
1/σ	1.198	3.502	1.053
Weight	0.208	0.609	0.183

The weight values in the table are from each (1/σ) divided by the sum of the three (1/σ). They represent the confidence of each parameter to predict the sample temperature. The greater the weight of the parameter, the more important that parameter is. However, the three weight values should always add up to 1. The equation applied to predict the sample temperature is,

$$T_s = W_{T2\_1} \cdot f_{Ts}(T_{2\_1}) + W_{T2\_2} \cdot f_{Ts}(T_{2\_2}) + W_A \cdot f_{Ts}[\mathrm{A2}/(\mathrm{A2} + \mathrm{A1})] \qquad (38)$$

where W_{T2_1}, W_{T2_2}, and W_A are the corresponding weights, and T_{2_1}, T_{2_2}, and A2/(A2+A1) are the measured values from the NMR instrument.

4.2 Correlation between T_2 and the Sample Temperature without the Shaft

To explore the effect of the shaft insertion, the experiments were also done with all the parameters kept the same as the ones discussed in the last section, except that the sample tube was placed in the NMR instrument without the shaft. The following graphs and tables are obtained by analyzing the data from these shaft-out experiments. The sample volume ratio between the two experiments is the ratio of cross sectional areas, $1 - (4.5/5.7)^2 = 0.377$, *i.e.* the volume of sample with the shaft inserted is 37.7 % of the sample without the shaft. Therefore, the intensity of the signal produced by the sample without the shaft was much

larger than with the shaft. The gain was reduced to bring the intensity to a range like that of the sample with shaft. The thermal conditions of the sample may have also changed slightly, since there was no shaft to act as a heat transfer path to the external environment.

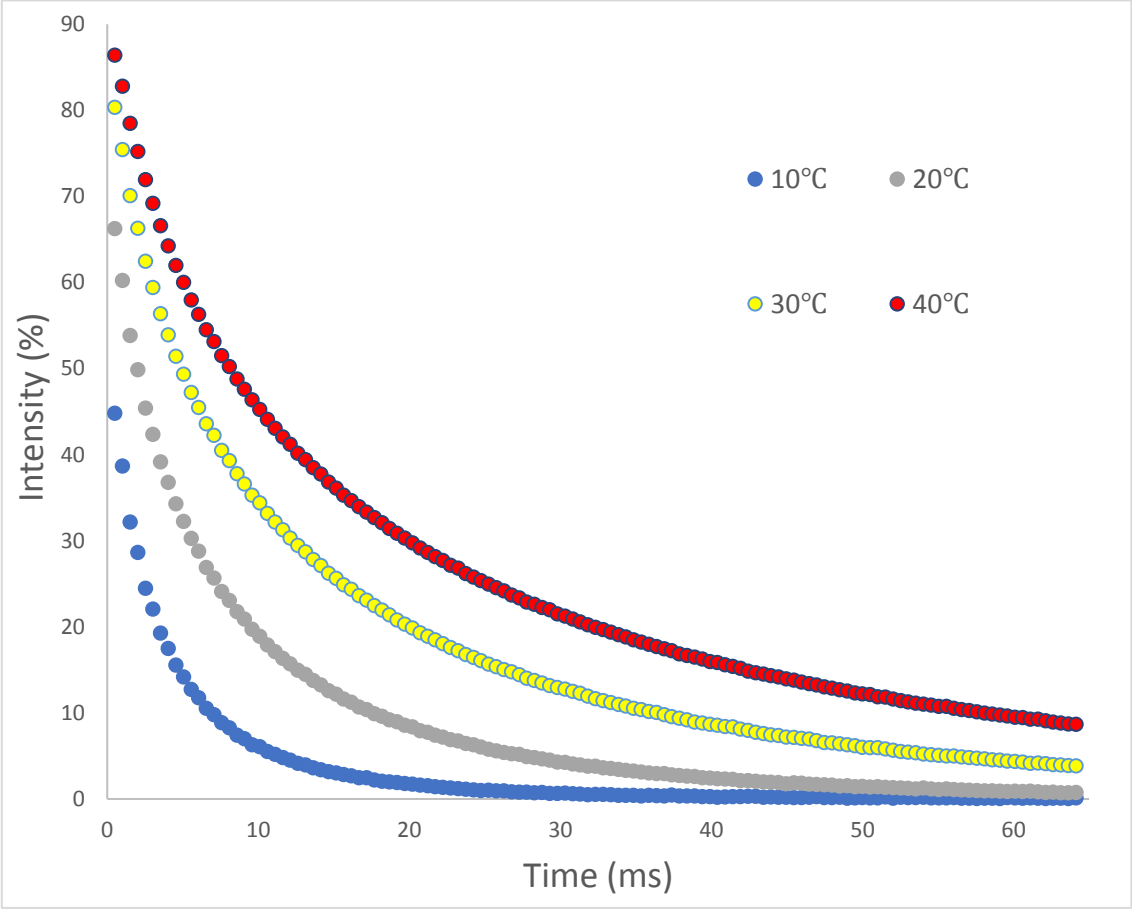

Figure 4 - 5 Intensity vs. time plot at different temperatures (set points), including 10, 20, 30, and 40 °C (without shaft, gain adjusted lower).

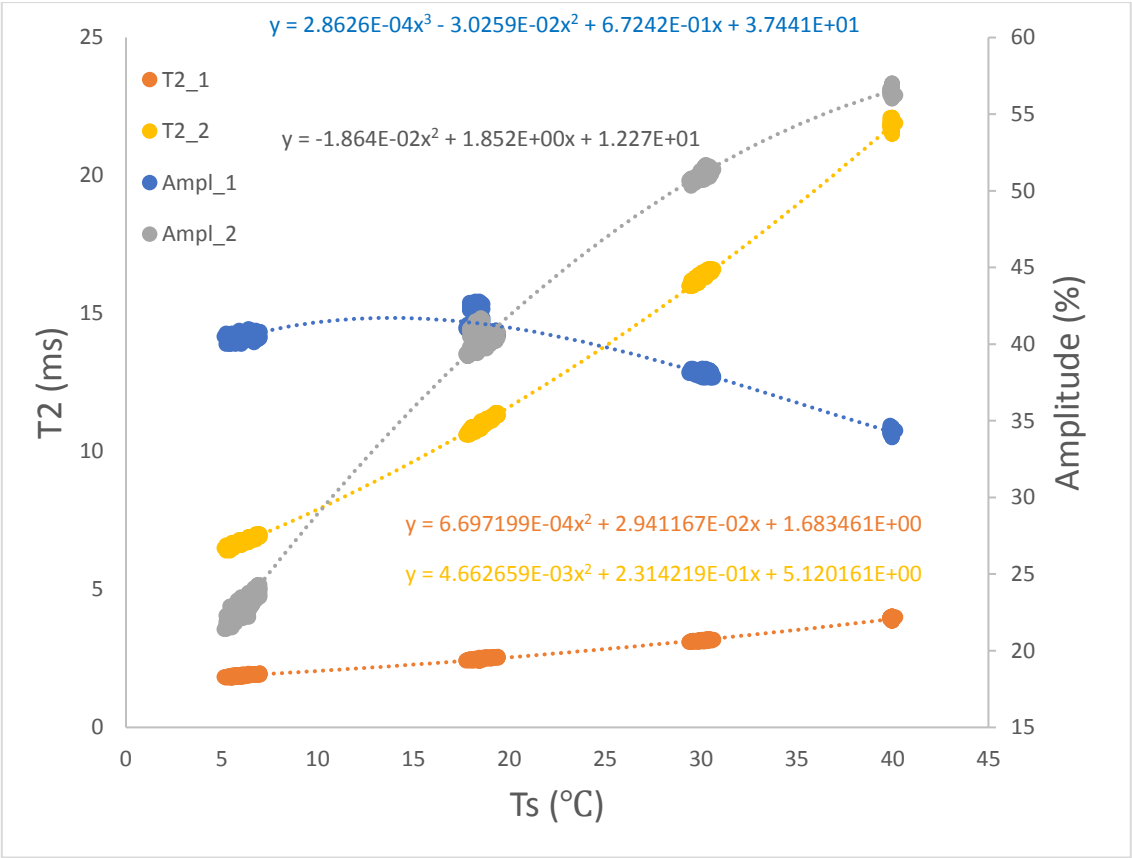

Figure 4 - 6 The measured T_2 relaxation times and amplitudes* as a function of the sample temperature without the shaft, together with the corresponding trendlines. Ampl_1 and Ampl_2 are the amplitudes of component 1 and 2 at time zero, whereas T_{2_1} and T_{2_2} are the relaxation times of component 1 and 2. (Note: the amplitudes are proportional to the amplitude of the reference that was used to calibrate the NMR)

It is apparent that T_{2_1} and T_{2_2} are still following the almost linear trends as the ones in the shaft-out experiments. From the original graph, Amp_1 and Amp_2 measured at 40 °C deviate from the polynomial trendlines (**Figure A - 1** in **Appendix**). However, amplitudes at 40 °C in **Figure 4 - 6** have been slightly adjusted from the original ones to get better trendlines (more details discussed in **Appendix 2**).

Therefore, using the correlations for T_{2_1} and T_{2_2} to estimate the sample temperature is more reliable compared with amplitudes' ones. To alleviate this problem, the ratio A2/(A2+A1) was used, as has been discussed in **Section 4.1**.

Table 4 - 3 The values of A1, A2, and A2/(A2+A1) determined from the correlations (without shaft).

T (℃)	T (K)	A1	A2	Ampl_Tot	A2/(A2+A1)
0	273	37.4	12.3	49.7	0.247
5	278	40.1	21.1	61.1	0.344
10	283	41.4	28.9	70.4	0.411
15	288	41.7	35.9	77.5	0.462
20	293	41.1	41.9	82.9	0.505
25	298	39.8	46.9	86.7	0.541
30	303	38.1	51.1	89.2	0.573
35	308	36.2	54.3	90.4	0.600
40	313	34.2	56.5	90.8	0.623
45	318	32.5	57.9	90.4	0.640

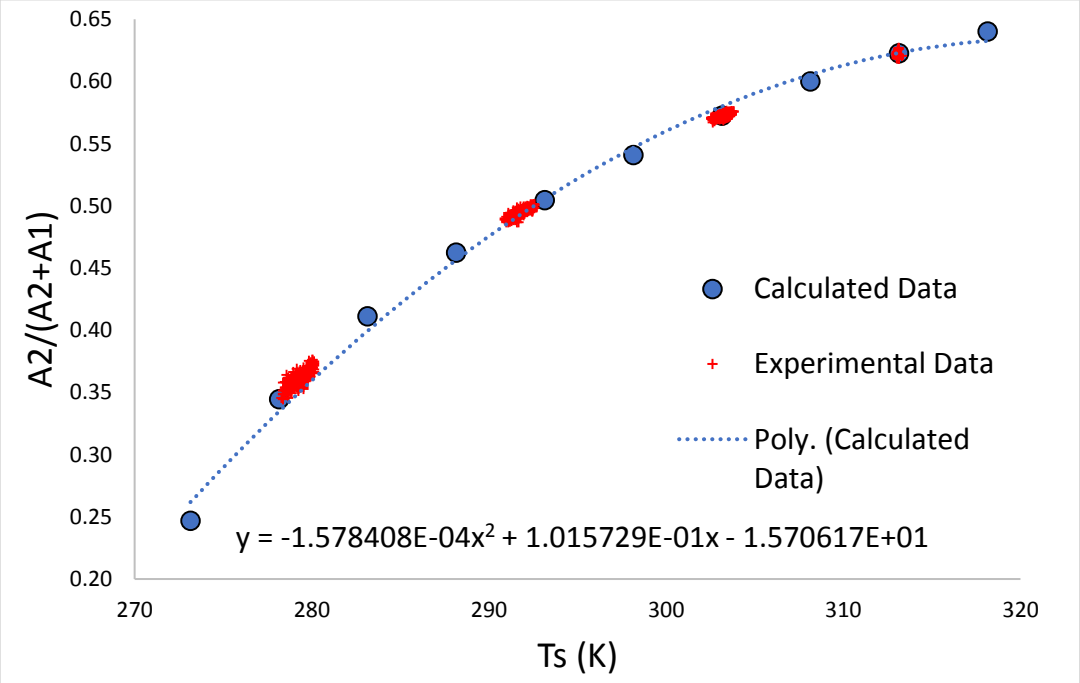

Figure 4 - 7 The calculated and experimental A2/(A2+A1) as a function of the sample temperature in K (without shaft). The trendline was added to the calculated data and the equation was displayed in the graph.

The correlation equations for T_{2_1}, T_{2_2}, and A2/(A2+A1) are the ones below, and the unit of T_s for T_{2_1} and T_{2_2} is °C, whereas the unit of T_s for A2/(A2+A1) is K.

$$T_{2\_1} = 6.697199 \times 10^{-4} T_s^2 + 2.941167 \times 10^{-2} T_s + 1.683461 \quad (39)$$

$$T_{2\_2} = 4.662659 \times 10^{-3} T_s^2 + 2.314219 \times 10^{-1} T_s + 5.120161 \quad (40)$$

$$\mathrm{A2/(A2 + A1)} = -1.578408 \times 10^{-4} T_s^2 + 1.015729 \times 10^{-1} T_s - 15.70617 \quad (41)$$

The standard deviations of the differences were then calculated, as shown in **Table 4 - 4**.

Table 4 - 4 The calculated values of standard deviation (σ), 1/σ, and weight by using T_{2_1}, T_{2_2}, and A2/(A2+A1) respectively (without shaft).

	T_{2_1}	T_{2_2}	A2/(A2+A1)
standard deviation (σ)	0.594	0.204	0.868
1/σ	1.683	4.893	1.152
Weight	0.218	0.633	0.149

The type of equation applied to predict the sample temperature is the same as equation (38).

4.3 Comparison between the Results from the Shaft-in and Shaft-out Experiments

Theoretically, the results from the shaft-in and shaft-out experiments should produce results that are the same or at least very close. This is because T_{2_1}, T_{2_2}, and A2/(A2+A1) are only dependent on the sample, if the 90° - 180° pulse separation is kept the same for all the experiments.

Obviously, both sets of intensities in **Figure 4 - 1** and **Figure 4 - 5** are dropping rapidly before 10ms and they are decreasing with the decrease of the set-point temperature. The trendlines for the T_2 relaxation times and the amplitudes, shown in **Figure 4 - 2** and **Figure 4 - 6**, are also very similar. So, the results from the shaft-in and shaft-out experiments are almost the same when only the graphs are considered. The weight values obtained for the shaft-in and shaft-out experiments are different from each other, as shown in **Table 4 - 5**, though they are in the same order of magnitude and follow the same ranking.

Table 4 - 5 The comparison of weights by using T_{2_1}, T_{2_2}, and A2/(A2+A1) from the shaft-in and shaft-out experiments respectively.

Weight	T_{2_1}	T_{2_2}	A2/(A2+A1)
Shaft-in	0.208	0.609	0.183
Shaft-out	0.218	0.633	0.149
Difference (% sh_in)	4.8	3.9	18.6

The weight factors for the three parameters are in the same range for measurements with and without shaft. In the case of the relaxation times, the weights with shaft are slightly smaller than without shaft. However, their combined differences produce a discrepancy between the weight factors of the amplitude ratio that is larger than the variation for the weights of the relaxation times. Further investigation on these differences was carried out by calculating both T_{shaft_in} and T_{shaft_out} from values of T_{2_1}, T_{2_2}, A1, A2, and T_S, measured from the shaft-in experiments and comparing them with the T_S values under the same conditions (**Table 4 - 6**). The investigation was conducted in duplicate for three different temperature levels, ~ 40, 30, and 20 °C.

Table 4 - 6 The calculated T_{shaft_in} and T_{shaft_out} using the values, T_{2_1}, T_{2_2}, A1, A2, and T_S, measured from the shaft-in experiments.

T_{2_1}	T_{2_2}	A1	A2	T_S (℃)	T_{shaft_in} (℃)	T_{shaft_out} (℃)
4.18	22.90	31.00	46.70	39.87	40.02	40.84
4.15	22.80	30.70	46.80	40.06	39.99	40.76
3.31	17.00	33.50	41.60	30.07	29.97	30.74
3.27	16.90	33.50	42.40	30.17	29.90	30.60
2.55	11.50	35.90	33.00	18.91	18.94	19.45
2.59	11.50	35.90	32.80	19.01	19.03	19.58

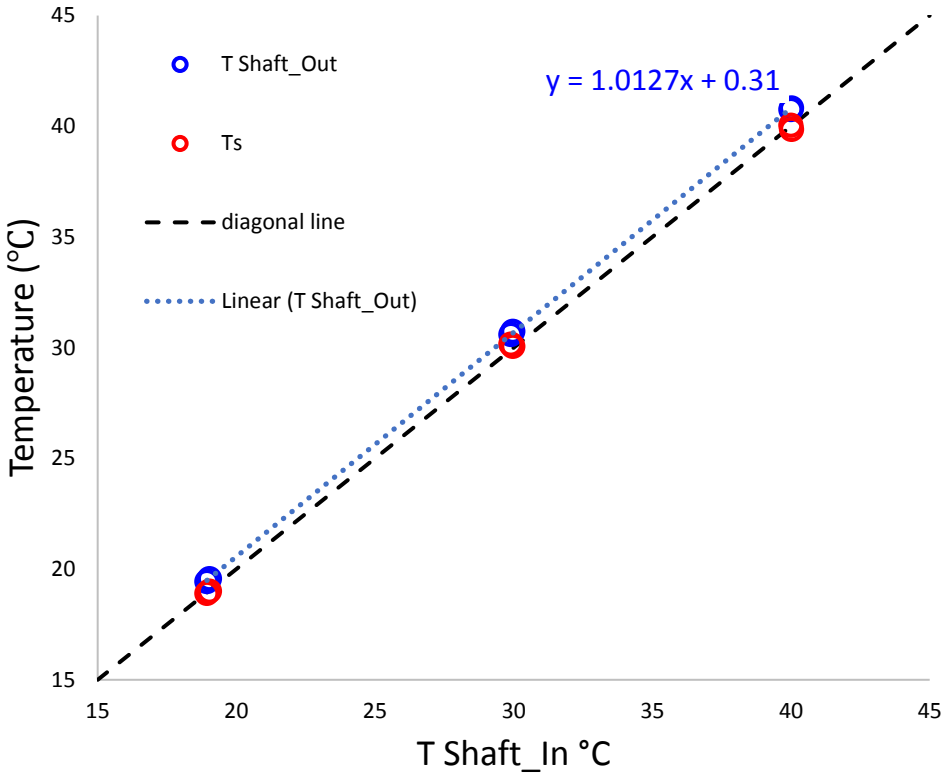

Figure 4 - 8 The T_{shaft_out} and T_S values as a function of the corresponding T_{shaft_in} values (**Table 4 - 6**). The trendline was added to the T_{shaft_out} data and the equation was displayed in the graph.

The values of the temperature estimated using the parameters for shaft-out (T_{shaft_out}), are between 0.51 - 0.82 °C higher than the temperature estimates (T_{shaft_in}) computed using

the parameters for shaft-in (**Table 4 - 6 and Figure 4 - 8**). The predictions derived from T_{shaft_in} and T_{shaft_out} were then compared to the measured values, T_s. The differences between T_{shaft_in} and T_S (0.02 - 0.27 °C) were obviously smaller than the differences between T_{shaft_out} and T_S (0.43 - 0.97 °C). Therefore, the correlations from the shaft-in experiments produce a more reliable estimate of the sample temperature than the estimates using the shaft-out parameters.

In summary, the presence of the shaft will slightly affect the results. The fact is that the shear experiments were conducted with shaft. In the shear experiments, all the parameters were kept the same as in the static shaft-in temperature-calibration experiments. Therefore, the correlations obtained from the shaft-in experiments were chosen and used as the tool to estimate the sample temperature under shear conditions.

The presence of two relaxation times indicates in some cases that two types of proton environments exist, for instance protons with different chemical bonds, or those attached to a surface and those that are free. In the case of the hydrocarbons, the chemical shift between $-CH_2$ and $-CH_3$ protons is too small to be detected by the low field NMR, and the ratio of molecules at surfaces with respect to the bulk is negligible.

However, it may also happen that the proton decay times were determined by two separate interaction effects. Each effect was the result of a different freedom of motion environment. The effect due to the highest motion freedom decays slower than the effect due to the lowest motion freedom. Roughly, it is very likely that the slow decay corresponds to the spin-spin interactions of individual protons within molecules, whereas the fast decay corresponds to the spin-spin interaction of protons from different neighbouring molecules. The Cannon 1000 oil is made up by a light mixture of higher alkanes (more than 9 carbons). Thus, the molecules (carbon backbone) move by reptation, rather slowly compared to the

vibrational freedom of the individual hydrogen atoms. This should preclude a diffusion effect. There is no *a priori* reason why the distribution of spin-spin interactions inside molecules and between molecules should change linearly with each other, or with temperature. At 0 °C, the ratio of T_{2_2}/ T_{2_1} is 3, and it increases to 6 at 55 °C.

The strange response of the distribution of amplitudes to temperature seems to also reflect this strong non-linearity.

4.4 Method Developed to Estimate the Sample Temperature

As discussed in the last section, the data from the shaft-in experiments are more reliable. Therefore, the equations (35), (36), and (37) were used to calculate T_{2_1}, T_{2_2}, and A2/(A2+A1) in the range from 5 °C to 75 °C, which were plotted in **Figure 4 - 9**.

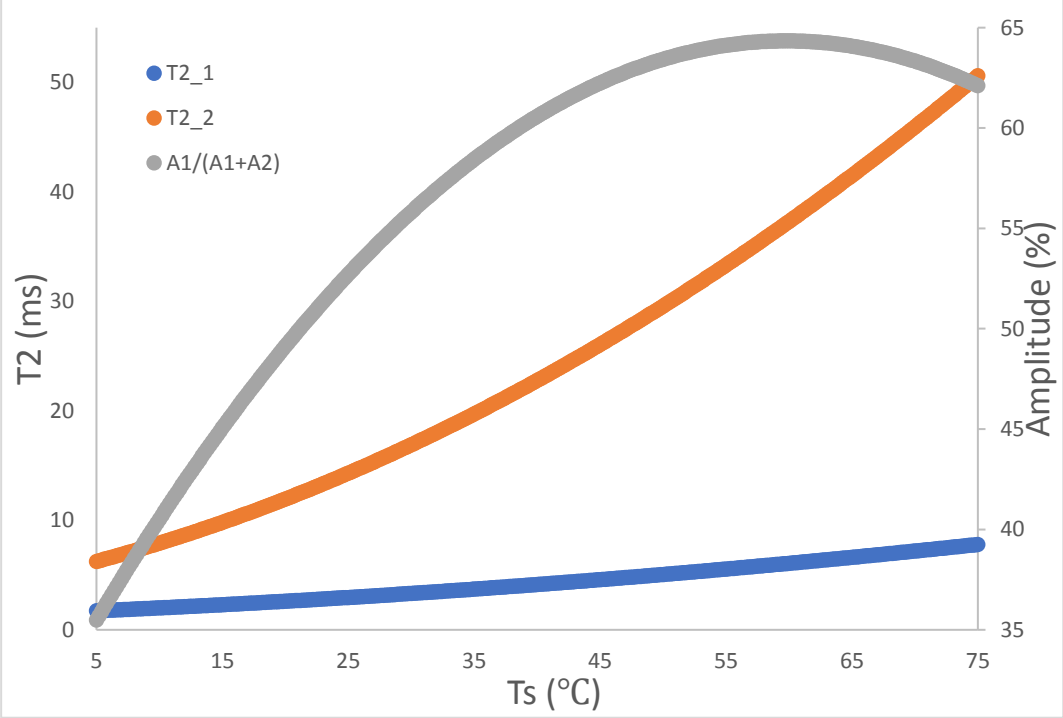

Figure 4 - 9 The plot of calculated T_{2_1}, T_{2_2} and A2/(A2+A1) in the range from 5 °C to 75 °C.

A2/(A2+A1) reaches its maximum value (approximately 64.33%) at about 59.8 °C. That means the sample temperature cannot be estimated if the measured A2/(A2+A1) is higher than 64.33% because it's out of the range of the obtained equation. However, the situation is very likely to happen when the sample temperature approaches 60 °C. The equation is an average, and therefore values somewhat above and below are expected. The confidence interval of the amplitude ratios corresponds to a temperature estimate within ± 0.95 °C. Experimental error, which is unavoidable during experiments, can also affect the amplitude measurement.

To solve this issue, different approaches to estimate the sample temperature will be applied according to some specific conditions. As shown in **Figure 4 - 10**, the trendline obtained for the amplitude is a parabola which reaches the peak at (59.8 °C, 64.34%). When the amplitude ratio, a_r, is larger than the maximum value (64.34%), only the correlations for T_{2_1} and T_{2_2} will be utilized; if it's smaller than 64.34%, the correlation for A2/(A2+A1) will be added to estimate the sample temperature. Section Two in the graph is divided into (a) and (b); because the equation (37) can be treated as a quadratic equation which has two solutions for a given A2/(A2+A1). So, if the estimated sample temperature is smaller than 59.8 °C, the positive root of the quadratic equation will be used to do the calculation; otherwise, the negative root will be used. The logic sequence is represented below,

suppose $T_s' = f\ (T_{2\_1}, T_{2\_2})$

if $a_r > 64.34$

$T_s = T_s'$

else

if $T_s' < 59.8$

$T_s = f\ (T_{2\_1}, T_{2\_2}, a_r)\ \ (+)$

else

$$T_s = f\left(T_{2\_1}, T_{2\_2}, a_r\right) \quad (-)$$

end

end

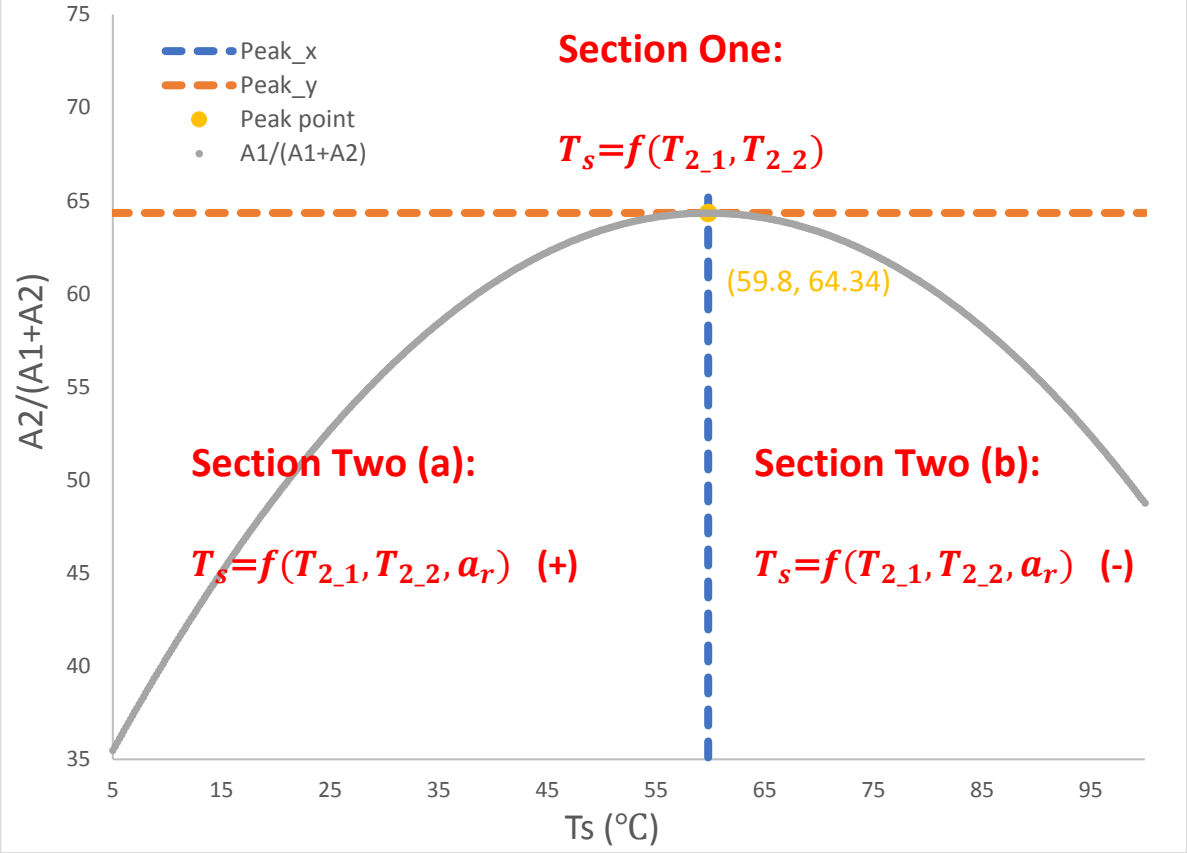

Figure 4 - 10 The diagram of how sections are divided when using the developed method to estimate the sample temperature.

The approach which only uses the correlations for T_{2_1} and T_{2_2} is similar to the one discussed in **Section 4.1**. The measured T_{2_1} and T_{2_2} of each run were plugged into the formulas to calculate the corresponding T_s, and the calculated T_s were compared with the measured ones to see the discrepancies. The standard deviations of the differences were then calculated, as shown in **Table 4 - 7**.

Table 4 - 7 The calculated values of standard deviation (σ), 1/σ and weight by using T_{2_1} and T_{2_2}.

	T_{2_1}	T_{2_2}
standard deviation (σ)	0.835	0.286
1/σ	1.198	3.502
Weight	0.255	0.745

The equation applied to predict the sample temperature is,

$$T_s = 0.255 \cdot f_{Ts}(T_{2\_1}) + 0.745 \cdot f_{Ts}(T_{2\_2}) \quad (42)$$

4.5 Measured Temperature Readings of the Thermistor and the Other Two FOTs

The inlet temperature of the Galden (T_{thmi}) was measured by a thermistor located outside the NMR, right after the active heat exchanger. The FOTs were located at the two flow channels of the thermal unit, one to measure the entrance and one to measure the exit temperature of the Galden. These temperatures are referred to as Ti and To, respectively. The temperature readings were recorded to study heat transferred from the Galden to the sample fluid. However, this approach needs to be somehow modified in the future, because T_{thmi}, Ti and To were all deviating from the reasonable values. This design limitation was very difficult to predict.

During the experiments, the thermistor itself was not touching the Galden flow directly, since it was encased in a brass fitting. The brass fitting, though somewhat insulated, was also exposed to the environment. The thermistor was sealed in the branch of a brass tee, and then was wired to a BNC connector. The Galden fluid was flowing through the

straight portion of the tee. Therefore, the heat transferred to the surrounding and from the sensor to the metal became a cause of temperature deviation.

The reason why Ti and To were deviating from the real values needs more investigation, but it is likely to be due to poor contact with the flowing Galden, and more contact with the external walls of the thermal unit. The measured Ti and To from the static experiments were plotted in **Figure 4 - 11**.

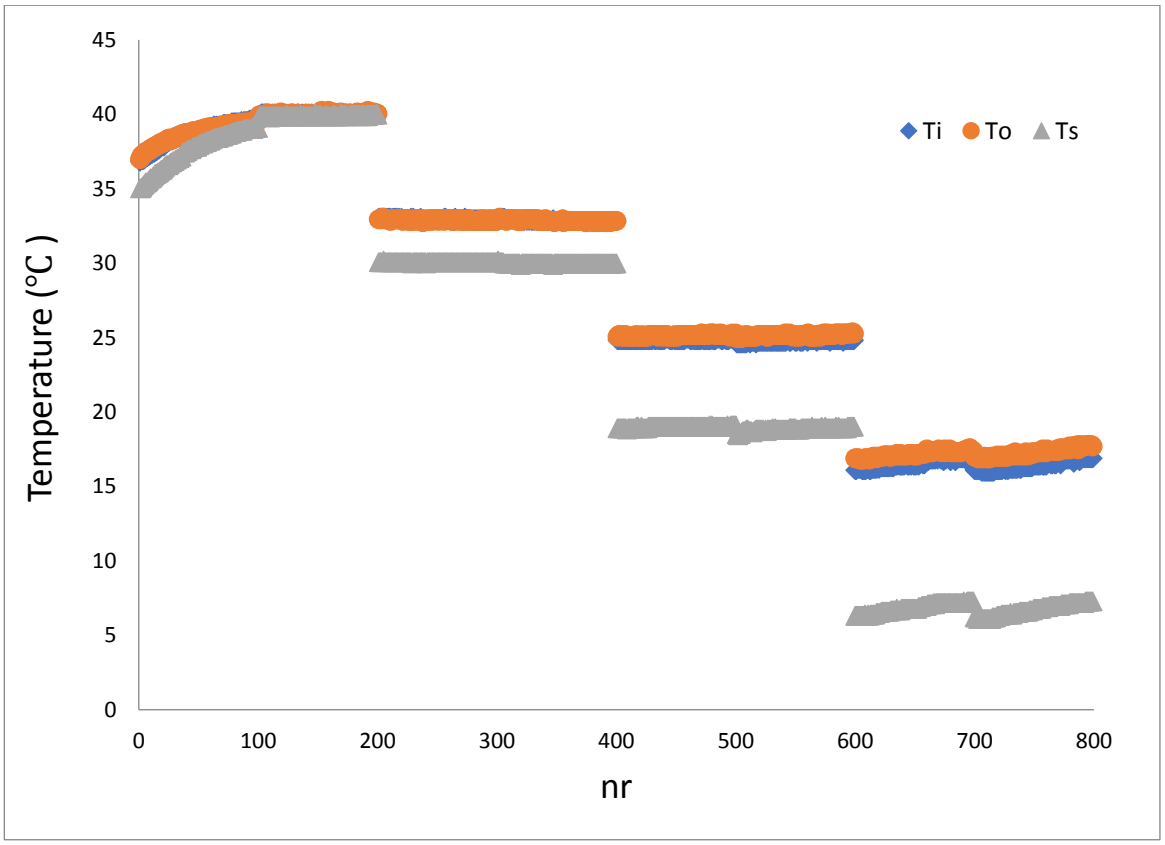

Figure 4 - 11 The plot of Ti, To, and T_s at different temperatures (set points), including 10, 20, 30, and 40 °C.

It shows clearly that all the T_s values, which measured inside the sample, are lower than the corresponding Ti and To values, which is impossible from the experiments' point of view. The sample was cooled by the Galden fluid through the thermal unit, therefore the

temperature of the Galden must be lower than the sample temperature. Remember that the magnet temperature is 40 °C. At low-temperature ranges, the impossibility becomes very clear. A simple experiment was conducted to check the reliability of the values. The sample tube was taken out of the NMR probe, and another calibrated FOT was placed at the bottom of the NMR probe where the sample tube was normally located. The FOT was to measure the surrounding temperatures around the sample tube at 10, 20, 30, and 40 °C. The measured temperatures were very close to the sample temperatures, *i.e.* lower than the corresponding Ti and To values. From this test, it was concluded that the measured T_s values were more reliable, whereas Ti and To could not be trusted.

CHAPTER 5 RESULTS AND DISCUSSION — II — EXPERIMENTS UNDER SHEAR CONDITIONS

Placing a temperature sensor into the narrow gap where the viscous sample is being subjected to shear is often impossible, and it will distort the flow pattern. Furthermore, the FOT is a fragile detector, and will be easily damaged if subjected to the rolling action of the shaft. Therefore, the development of an NMR thermometer has been proposed as an alternative means to estimate the temperature of the liquid under shear flow.

The correlations developed in the previous section were applied to estimate the sample temperature under shear flow, at different rotational speeds of the shaft. The inlet temperature was controlled to ~ 20, 30, and 40 °C. However, the actual temperatures for the ~20 °C controller resulted in temperatures closer to 15 °C. For the sake of uniformity, the nominal value of the temperature setpoint given to the controller is used as a label for the experimental results at each temperature.

The proprietary CPMG pulse sequence of the minispec was run continuously on the NMR, and the values of T_{2_1}, T_{2_2}, A1, and A2 for each run were saved by the minispec software. Then, these data were imported into Excel and plugged into equation (42) & (43) to get the calculated sample temperatures, with the algorithm explained in **Chapter 4**. The f_{Ts} are the quadratic solutions to the second order polynomials.

$$T_s = 0.208 \cdot f_{Ts}(T_{2\_1}) + 0.609 \cdot f_{Ts}(T_{2\_2}) + 0.183 \cdot f_{Ts}[\mathrm{A2}/(\mathrm{A2} + \mathrm{A1})] \qquad (43)$$

5.1 Calculated sample temperatures as function of the rotational speed, grouped by inlet temperatures

Figure 5 - 1 shows the calculated sample temperatures from experiments performed for nominal inlet temperatures (Ti) of 40, 30, and 20 °C. The results are plotted as a function of the rotational speeds: 0.1, 1, 10, 30, and 50 rps. They correspond to Newtonian average shear rates of 2.609, 26.09, 260.9, 782.7, and 1304.5 s^{-1}. The temperature was stabilized for 20 minutes, and then 20 data points were collected under static conditions (cycle 1_static in colour blue). After this, the shaft was set to rotate at a given speed, and 20 data points were collected under shear conditions (cycle 1_shear in colour orange). The shaft was then stopped, and another 20 static points were taken, before the speed setpoint was changed, and the shearing step started. The five speeds with their static intermezzos constituted a cycle. After the end of the cycle, another cycle was run in the same conditions (cycle 2_static in colour grey and cycle 2_shear in colour yellow). In total, 200 data points were collected for each cycle, 100 under the static condition and 100 under different speeds. Two cycles were conducted for each shear experiment. The recycle delay was 2 seconds, and the scans were 8 per point. It took thus 16 seconds to produce one data point. The static time was hence 320 s, and the same was the shearing time. The symbol ‘nr’ stands for the sequence of data points for each cycle in the following figures, where 0 - 20 is at 0.1 rps, 20 - 40 at 1 rps, 40 - 60 at 10 rps, 60 - 80 at 30 rps, and 80 - 100 at 50 rps.

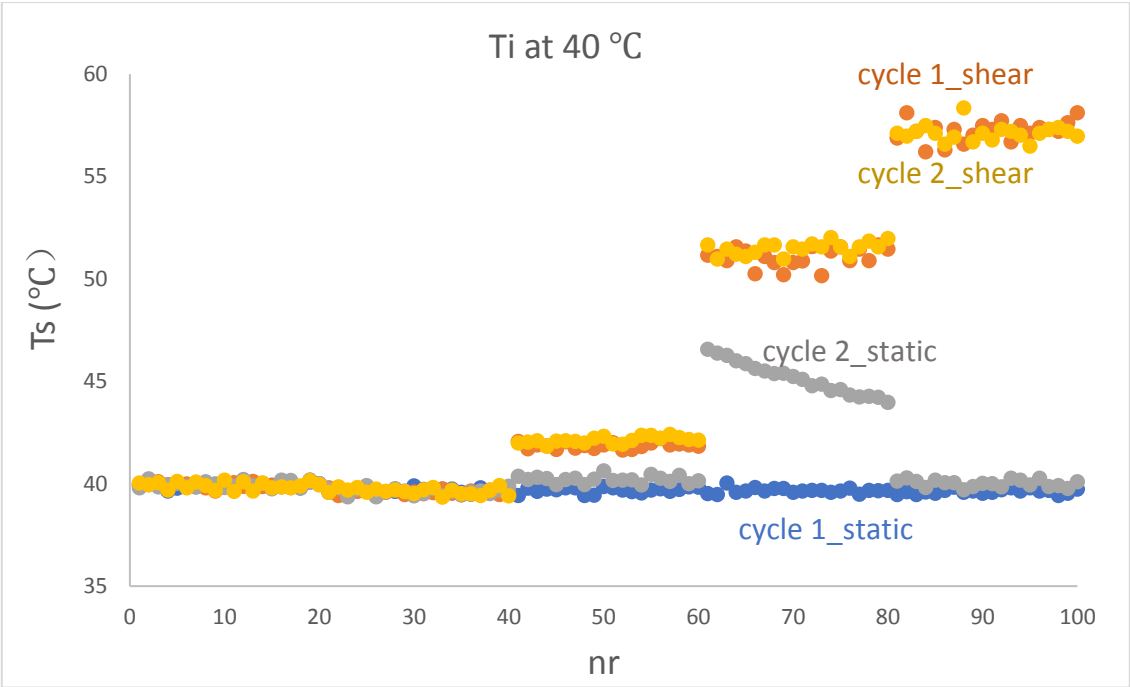
Ti at 40 °C
cycle 1_shear
cycle 2_shear
cycle 2_static
cycle 1_static
Ts (°C)
nr
60
55
50
45
40
35
0
10
20
30
40
50
60
70
80
90
100

(a)

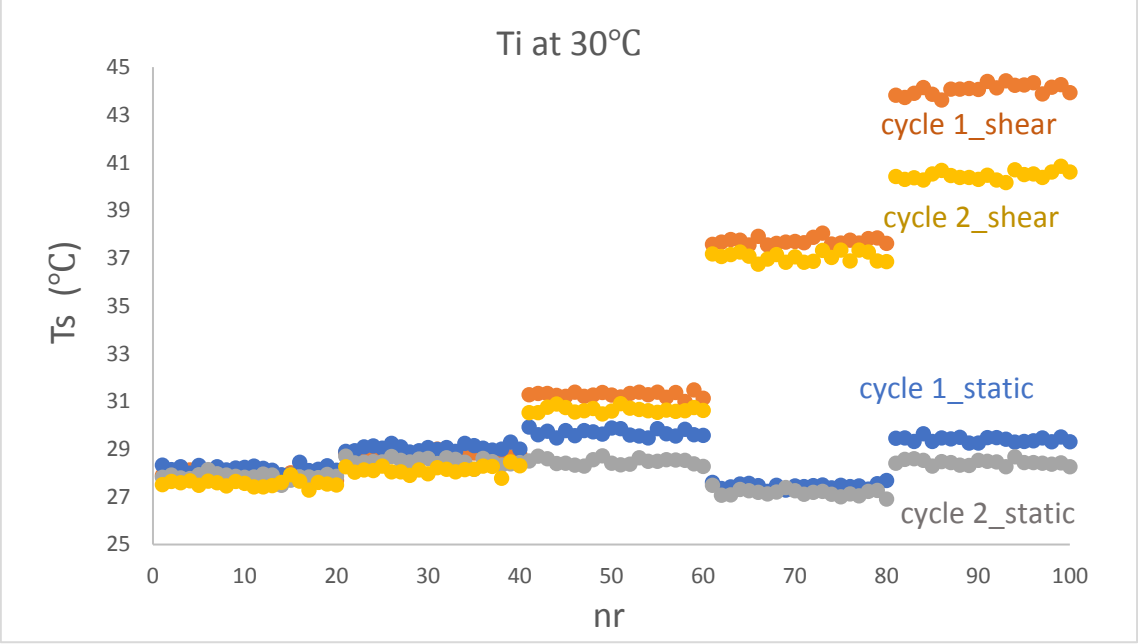
Ti at 30°C
cycle 1_shear
cycle 2_shear
cycle 1_static
cycle 2_static
Ts (°C)
nr
45
43
41
39
37
35
33
31
29
27
25
0
10
20
30
40
50
60
70
80
90
100

(b)

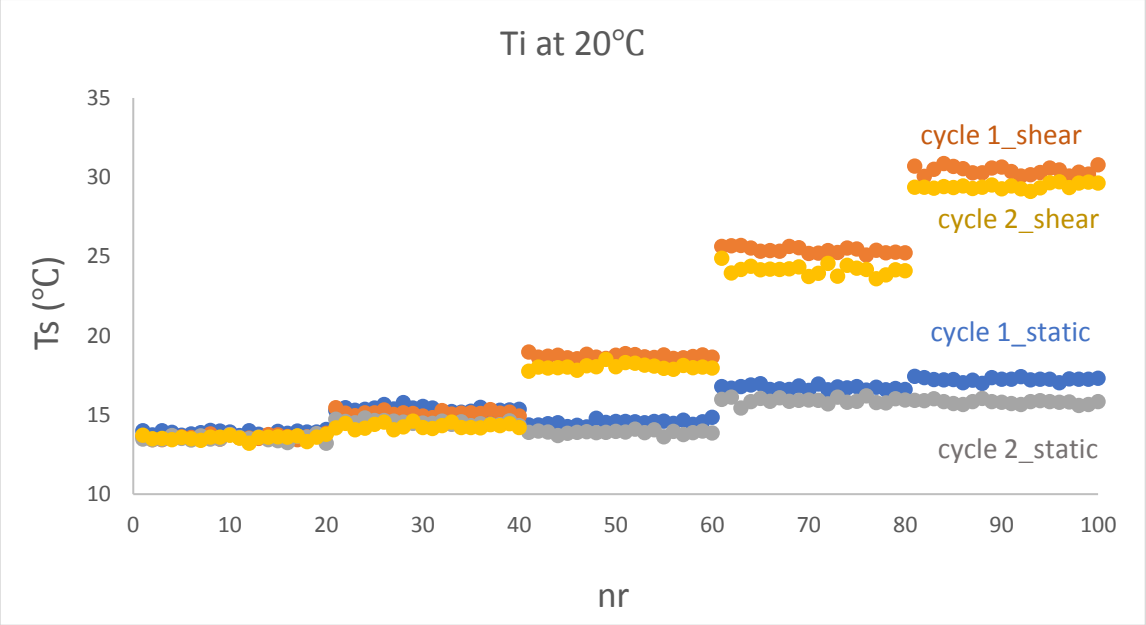

(c)

Figure 5 - 1 The plots of the corresponding sample temperatures at the static condition and at different rotational speeds (0.1, 1, 10, 30, and 50 rps). Ti was controlled to be ~ 40 °C in (a), ~ 30 °C in (b) and ~ 20 °C in (c).

The sample temperatures under the static condition (the static temperatures) were used to check if the heat generated in the last shearing step had already been dissipated, and to compare with the sample temperatures obtained under various rotational speeds (the shear temperatures). The aim was to observe the temperature increase caused by the viscous heat generated due to shearing.

The three plots share the same general qualitative trend of temperature increase with the increase of the rotational speed. To be more specific, the shear temperatures remain essentially the same under the low rotational speeds of 0.1 and 1 rps, with slight discrepancies compared with the corresponding static temperatures. For the discrepancy under 1 rps at 30 °C (Ti), the static temperatures are even higher than the shear temperatures. The reason for that was speculated to be a temperature control mishap.

On the other hand, the differences between the static and shear temperatures are readily observable from 10 to 50 rps; especially for higher rotational speeds, the discrepancies are impressively large (~ 10 °C) in **Figure 5 - 1 (b)** and **(c)** under 30 rps, approaching 14 °C under 50 rps.

These findings, albeit rough, are very promising for the development of an NMR thermometer applicable to viscous complex fluids with similar relaxation times, such as crystallizing fats and oils.

5.2 Calculated sample temperatures as function of the inlet temperatures, grouped by rotational speed

Figure 5 - 2 shows the calculated sample temperatures, rearranged in groups of rotational speeds of 0.1, 1, 10, 30, and 50 rps, as a function of inlet nominal temperatures decreasing from 40 to 30, and to 20 °C. As described in the procedure part, the inlet temperature had to remain stable for 20 min, and 20 data points were collected before any shear step. In total, there were 120 data points for one cycle, 60 of which were presented as cycle n_static (n = 1 or 2) in the following graphs.

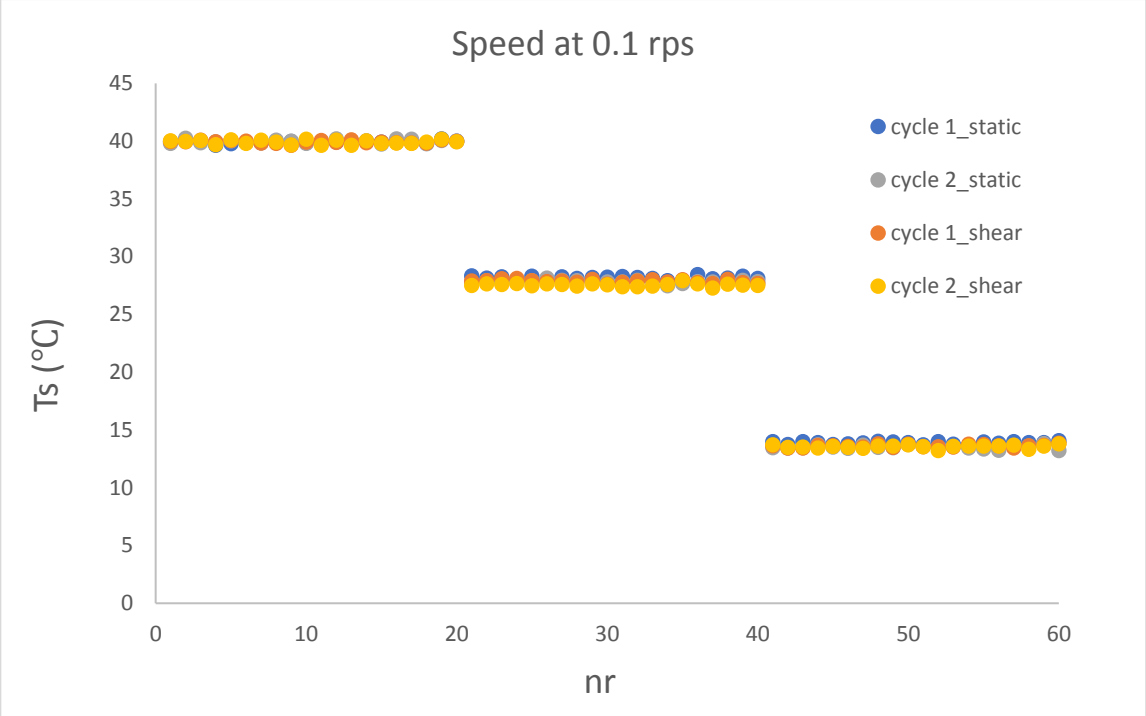
Speed at 0.1 rps
Ts (°C)
nr
cycle 1_static
cycle 2_static
cycle 1_shear
cycle 2_shear
0
5
10
15
20
25
30
35
40
45
0
10
20
30
40
50
60

(a)

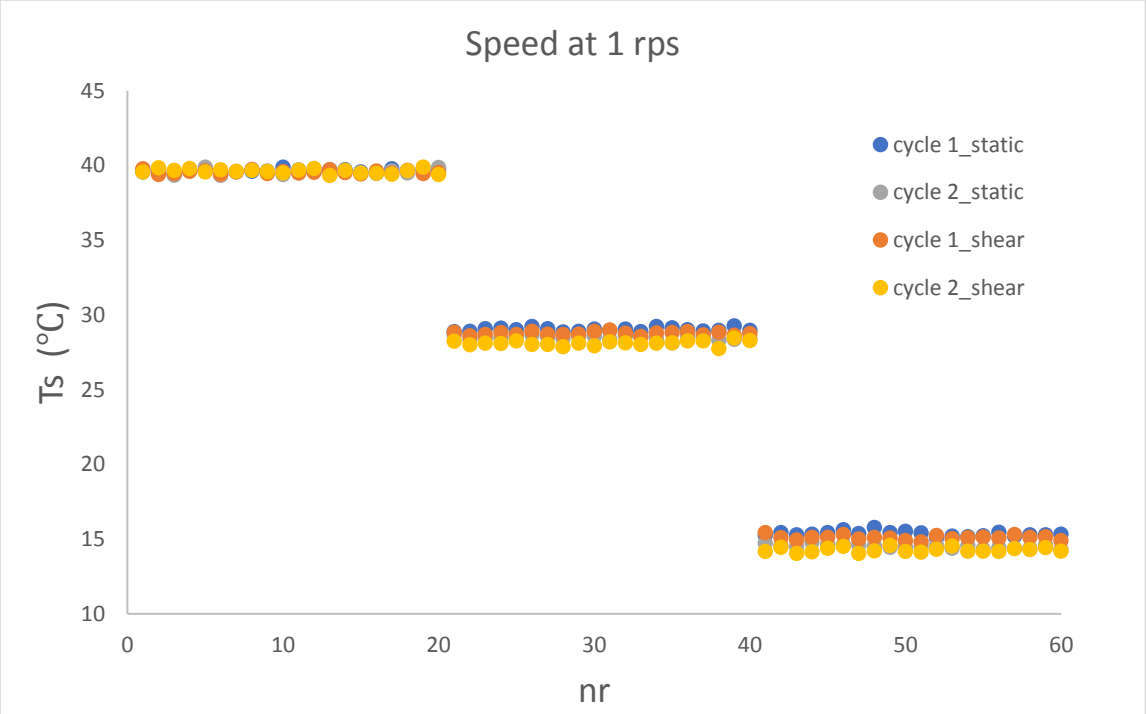
Speed at 1 rps
Ts (°C)
nr
cycle 1_static
cycle 2_static
cycle 1_shear
cycle 2_shear
10
15
20
25
30
35
40
45
0
10
20
30
40
50
60

(b)

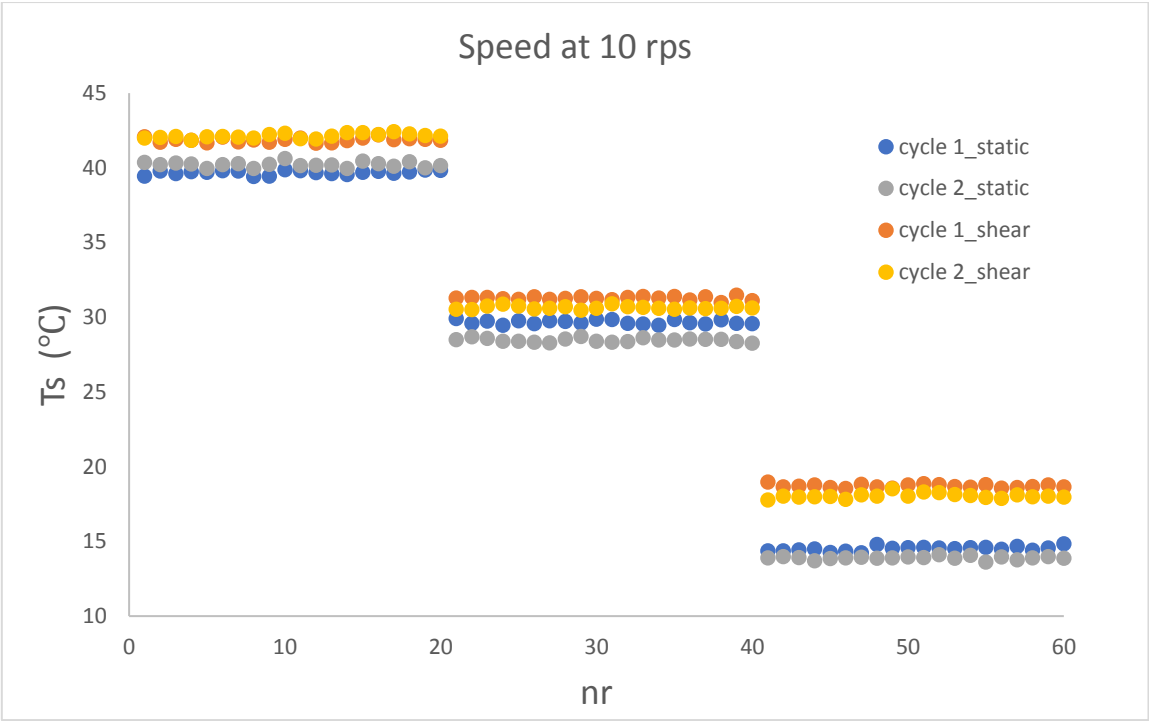
Speed at 10 rps
Ts (°C)
nr
cycle 1_static
cycle 2_static
cycle 1_shear
cycle 2_shear
45
40
35
30
25
20
15
10
0
10
20
30
40
50
60

(c)

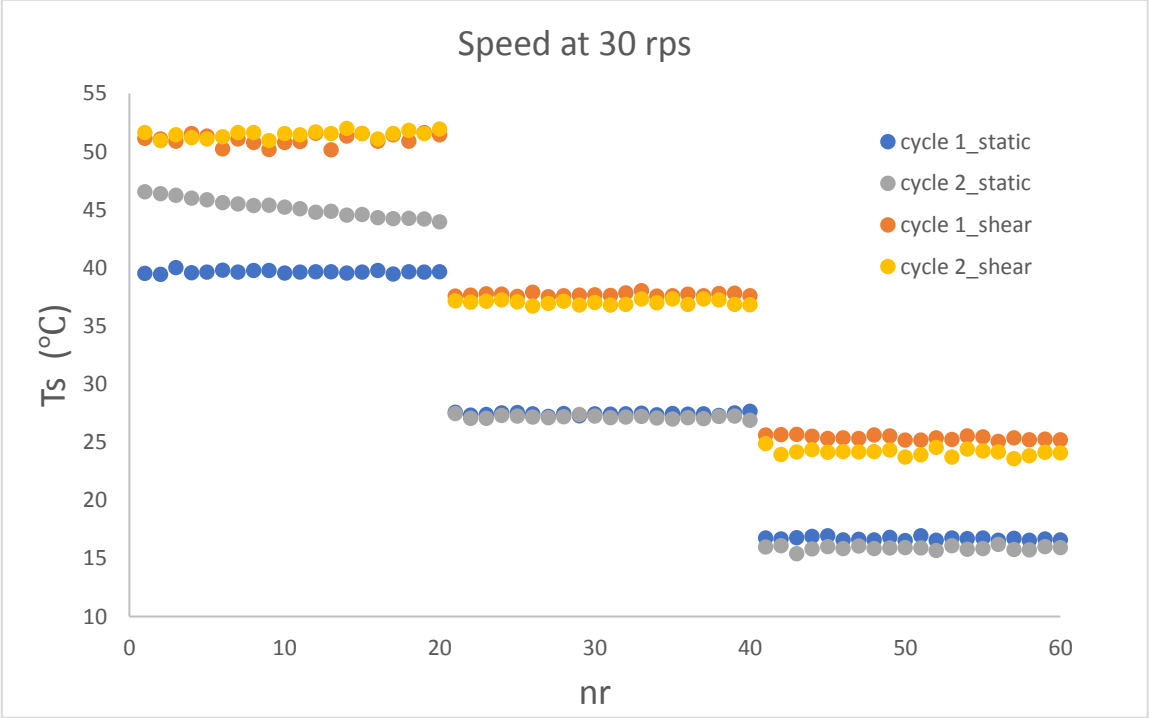
Speed at 30 rps
Ts (°C)
nr
cycle 1_static
cycle 2_static
cycle 1_shear
cycle 2_shear
55
50
45
40
35
30
25
20
15
10
0
10
20
30
40
50
60

(d)

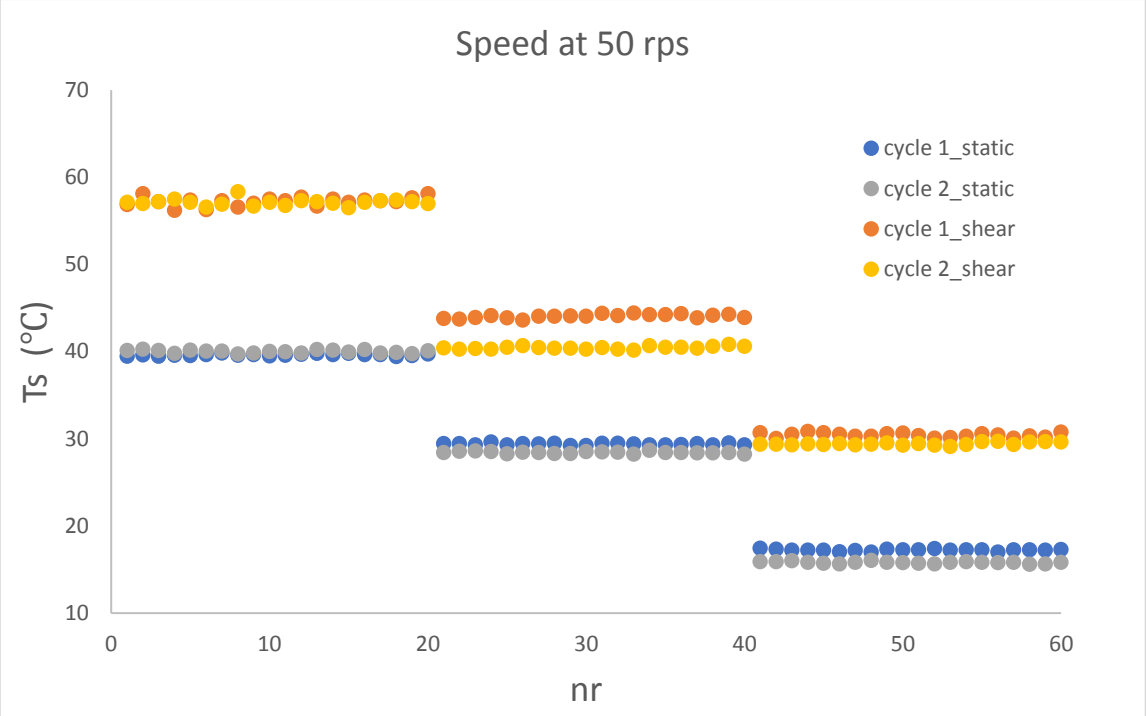

(e)

Figure 5 - 2 The plots of the corresponding sample temperatures under various inlet temperatures (40, 30, and 20 °C). Rotational speed was controlled to be 0.1 rps in (a), 1 rps in (b), 10 rps in (c), 30 rps in (d), and 50 rps in (e).

At lower inlet temperature, the differences between the static and shear temperatures were expected to increase. The calculated temperatures, however, remained practically the same in **Figure 5 - 2 (a)** and **(b)** (0.1 and 1 rps respectively). Under the rotational speed 10 rps, there are slight discrepancies between the temperatures (~ 2 °C) at 40 and 30 °C, and ~ 4 °C difference at 20 °C. At 30 rps, the temperature difference (~ 10 °C) at 30 °C was even larger than that at 20 °C (~ 8.5 °C). The temperature differences at 30 and 20 °C are roughly the same (~ 13.4 °C) under 50 rps. In summary, the temperature differences at the nominal Galden fluid temperatures of 40, 30, and 20 °C, do not clearly follow the change of the inlet temperatures, for a given rotational speed.

5.3 Summary of observations for calculated sample temperatures

To visualize the relationship between the sample temperatures, the rotational speeds, and the inlet temperatures, one average value was calculated for each set of data having the same rotational speed and inlet temperature. These averaged sample temperatures as well as the measured (static) sample temperatures, were plotted against the corresponding rotational speeds, as shown in **Figure 5 - 3**.

At 40, 30, and 20 °C, the change of the shear temperatures is following essentially the same trend; that is, the calculated temperature under shear is increasing while the rotational speed is increasing. However, the slope of the trendline is gentler as the inlet temperature increases. This is likely caused by the higher temperature difference between the room temperature (25 °C) and the sample temperature as temperature increased. Thus, the larger heat transfer rate to the environment produced a lesser increase in the N1000's temperature.

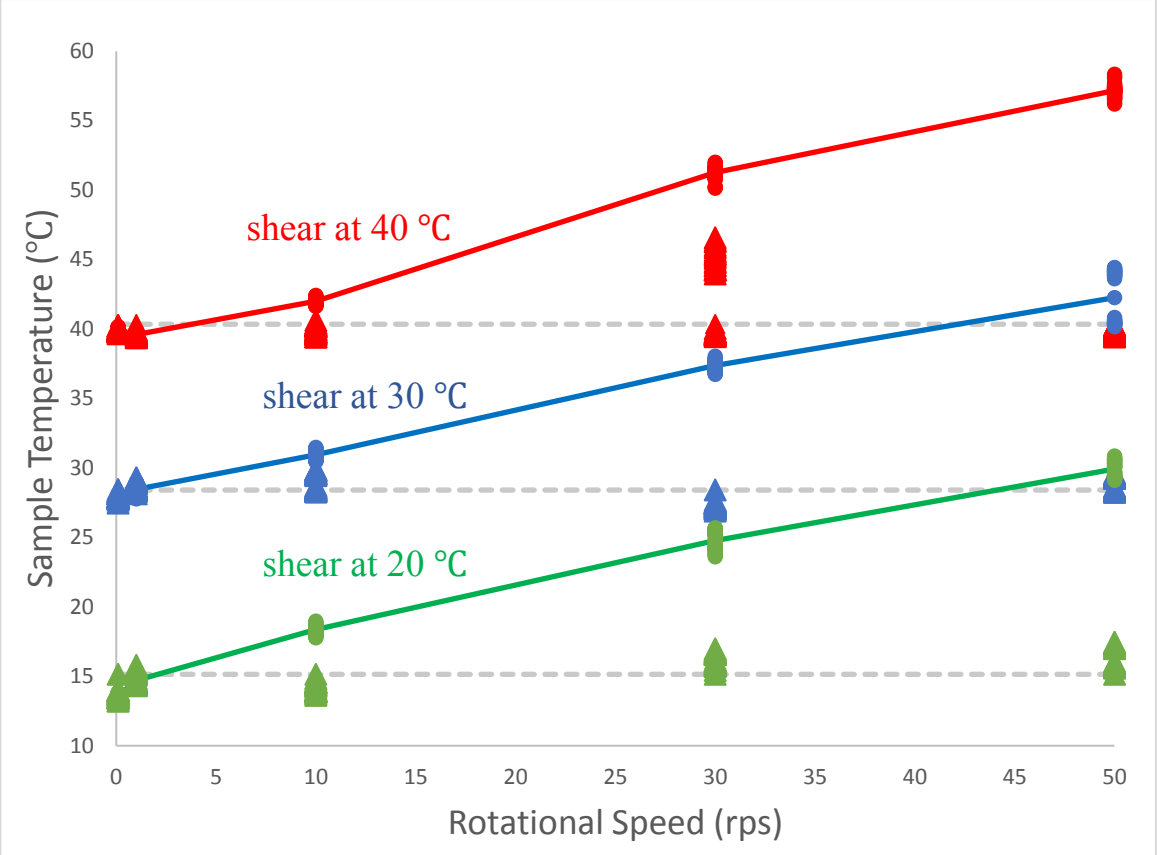

Figure 5 - 3 The plot of all the sample temperatures calculated for static steps or at rotational speeds of 0.1, 1, 10, 30, and 50 rps (the circle markers represent the shear data and the triangle markers the static data). The solid lines represent the averaged sample temperatures under shear conditions, whereas the dotted ones represent the averaged sample temperatures under static conditions.

The temperature differences between the shear and static temperatures were plotted as a function of rotational speed in **Figure 5 - 4**. It is clear that the temperature difference increases as the rotational speed increases, as has been discussed in **Section 5.1**. The temperature differences at 40 °C fit a second order polynomial quite well, yet the ones at 20 and 30 °C are following some weird trends. For example, the increase rate of the temperature difference at 30 °C rises rapidly till the rotational speed reaches 25 rps, and then the increase rate slows down.

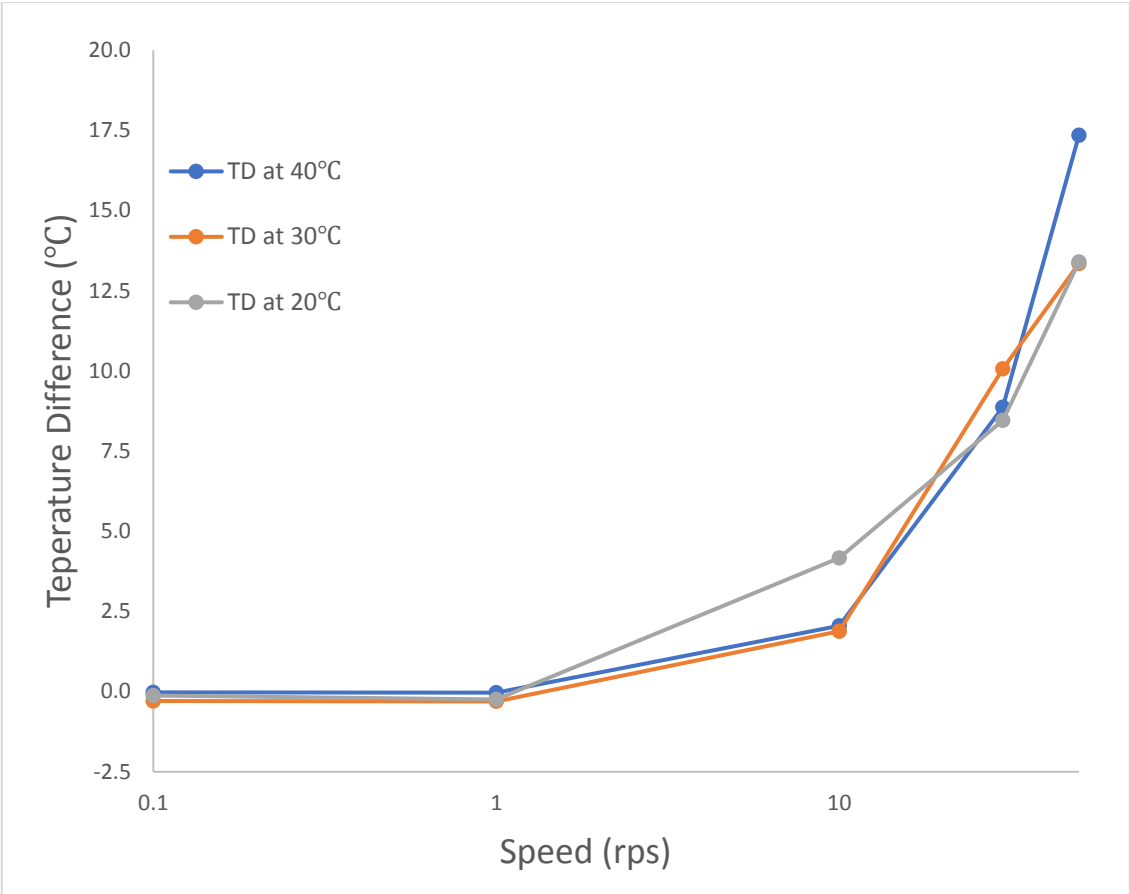

Figure 5 - 4 The plot of the temperature differences between the average shear and static temperatures at rotational speeds of 0.1, 1, 10, 30, and 50 rps.

5.4 Comparison between the experimental results and the predictive empirical equations for the NMR thermometer

All the measured T_2 relaxation times, amplitudes, and calculated sample temperatures from equation (42) & (43) are referred to as "experimental results, ER", which were plotted in **Figure 5 - 5**. The displayed equations of the corresponding empirical equations for T_{2_1}, T_{2_2}, A1, and A2 in **Figure 4 - 2** were also plotted as "expected NMR values, ENV".

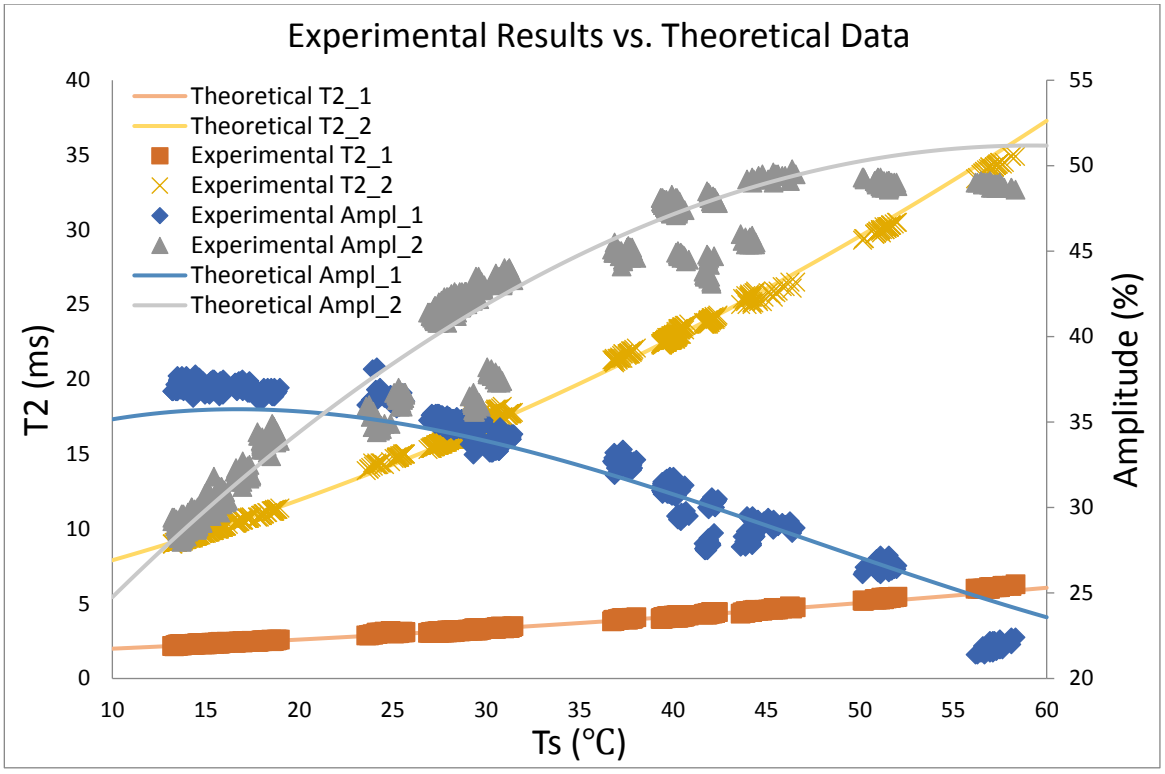

Figure 5 - 5 The plot of all the experimental results and the theoretical data.

The patterns of the experimental results were not identical to the curves plotted from the empirical equations. Thus, this is not simply a back-calculation of data already computed by these equations. Due to their higher statistical weight (hence, better reproducibility), the data points for both T_{2_1} and T_{2_2} are located at or near the corresponding curves. Conversely, the data points for A1 and A2 display clusters that deviate from the curves, especially the points around 24, 30, 42, and 57 °C. As had been estimated earlier for the static measurements, using T_2 values to estimate the sample temperature is much more reliable than using amplitude values. Though the mathematical determination of the four parameters is not independent, the effect of the amplitude values on the parameters of the fit is much weaker than the effect of the decay times.

5.5 Predictions of a simulation by a thermo-rheological mathematical model for heat generation and dissipation, compared to the experimental results

This mathematical model was developed by Dr. Mazzanti and Fan Wang in 2012, and it has already been discussed in the literature review (**Section 2.2.2**). The model was implemented in Matlab® with the code from Fan's research, but with the experimental settings of this work: geometry of the shaft, etc. It was solved using the experimental data of mechanical power P_w for each ν and Ti. P_w was given by the product of the torque τ_s by the angular velocity ώ, as measured by the rheometer.

Table 5 - 1 The mechanical power P_w for each ν and Ti at 20, 30, and 40 °C.

	20 °C	30 °C	40 °C
0.1	7.63E-05	2.81E-05	1.36E-05
1	7.55E-03	3.17E-03	1.85E-03
10	3.77E-01	2.37E-01	1.64E-01
30	9.68E-01	1.09E+00	8.18E-01
50	1.34E+00	1.55E+00	1.56E+00

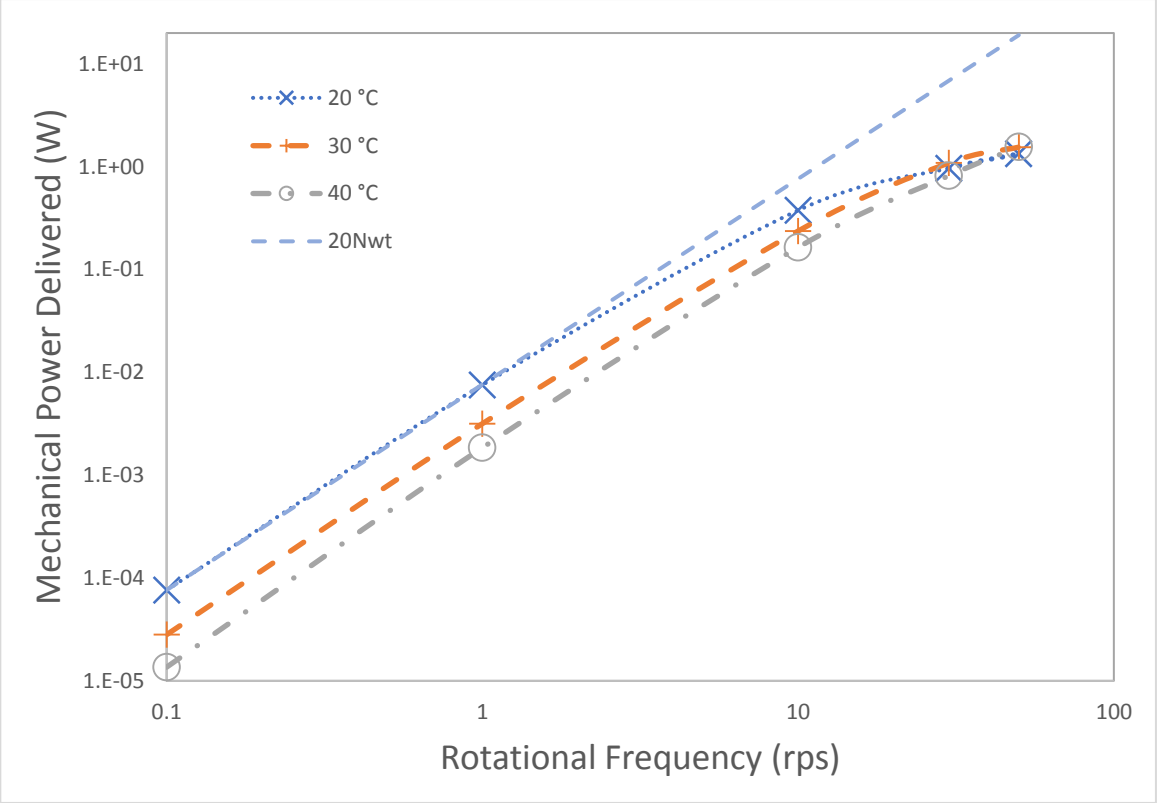

Figure 5 - 6 Mechanical power delivered by the shaft at each process temperature as a function of rotational frequency (0.1, 1, 10, 30, and 50 rps). The blue dash line (20Nwt) stands for the mechanical power delivered for a Newtonian fluid at 20 °C. Error bars of three standard deviations would be much smaller than the symbols used.

The mechanical power delivered at the shaft, as a function of rotational frequency at different Galden temperatures, is summarized in **Figure 5 - 6**. The power generated spanned five orders of magnitude while the rotational frequencies covered three orders of magnitude. The mechanical power delivered by the rheometer is proportional to the square of the rotational frequency for an ideal Newtonian fluid.

The general expression for power (per unit volume) produced by a fluid at a point in the fluid is given by equation (14), reproduced here for convenience.

$$\dot{q}_v = \eta \cdot \dot{\gamma}^2 \tag{14}$$

The volume of the sample is almost constant. The average shear rate under isothermal conditions was presented in equation (23), copied here for convenience

$$\dot{\gamma}_{av} = \frac{-4 \cdot \kappa^2 ln(\kappa)}{(1-\kappa^2)^2} \cdot \dot{\omega} \tag{23}$$

The term that multiplies the angular velocity depends only on the ratio of radiuses, $\kappa = 0.7895$, and it is therefore constant.

$$\dot{\gamma}_{av} = k_\kappa \cdot \dot{\omega}\ , with\ k_\kappa = \frac{-4 \cdot \kappa^2 ln(\kappa)}{(1-\kappa^2)^2} = 4.152 \tag{44}$$

$$\dot{q} = V \cdot \eta \cdot \dot{\gamma}^2 = [V \cdot \eta \cdot (k_\kappa)^2] \cdot \dot{\omega}^2 = [V \cdot \eta \cdot (2\pi \cdot k_\kappa)^2] \cdot \dot{v}^2 \tag{45}$$

At constant temperature, all terms in the square bracket are constant. Therefore, one would expect that a log-log plot of data of power as a function of rotational speed would have a slope of 2:

$$ln(\dot{q}) = ln[const] + 2 \cdot ln(\dot{v}) \tag{46}$$

Even if there was some inaccuracy in the determination of the parameters of κ, η, or the sample volume V, this would not affect the 'slope' of 2, but only the constant 'intercept'.

The slope of the mechanical power for the rotational frequencies of 0.1 to 10 rps is in fact very close to 2, indicating that the viscous heating is negligible in that range.

However, the slope of the mechanical power begins to decrease when the rotational frequency goes above 10 rps. It happens at high shear rates, for the heat produced will increase the sample temperature and decrease the sample viscosity. It will also distort the velocity profile, so the average shear rate no longer can be estimated accurately by equation (23).

The data obtained from the rheometer are used for a simple thermo-rheometric model, which estimated the temperature from the power, using the viscosity and thermal

conductivity of N1000. It can only be applied to a Newtonian fluid, and it assumes the fluid is isothermal.

The power delivered can be used as well as the input for a more complex thermo-rheometric model. This more complex model also estimated the temperature from the power. Additionally, it included the thermal conductivity of N1000, not only its viscosity. The temperature estimated by the model is not directly an average temperature, but rather a temperature profile from the shaft to the inner wall of the glass tube. To calculate the average temperature, the simple method of adding all the data points and then divide the sum by the number of points is not applicable. The sample shape is a hollow cylinder, and therefore the mass of N1000 per radial point increases between the shaft and the wall. Thus, equation (47) was applied to estimate the average temperature.

$$\bar{\theta} = \frac{2}{1-\kappa^2}\int_{\kappa}^{1} r\theta(r)dr \tag{47}$$

where $\bar{\theta}$ is the average non-dimensional temperature.

The temperatures estimated from both simple and complex thermo-rheometric models were summarized and compared in **Table 5 - 2**, **Figure 5 - 7** and **Figure 5 - 8**.

Table 5 - 2 The estimated sample temperatures (°C) at 20, 30, and 40 °C. Tiso stands for the sample temperature from the isothermal model, whereas Tm stands for the sample temperature from the elaborated model.

Rotational Speed (rps)	Tiso (20°C)	Tiso (30°C)	Tiso (40°C)	Tm (20°C)	Tm (30°C)	Tm (40°C)
0.1	15.30	29.22	41.24	15.29	29.22	41.23
1	15.44	27.39	35.91	15.43	27.38	35.90
10	24.85	31.87	37.91	24.53	31.66	37.77
30	45.51	43.31	48.73	44.72	42.42	48.07
50	59.69	56.44	56.39	58.66	55.23	55.17

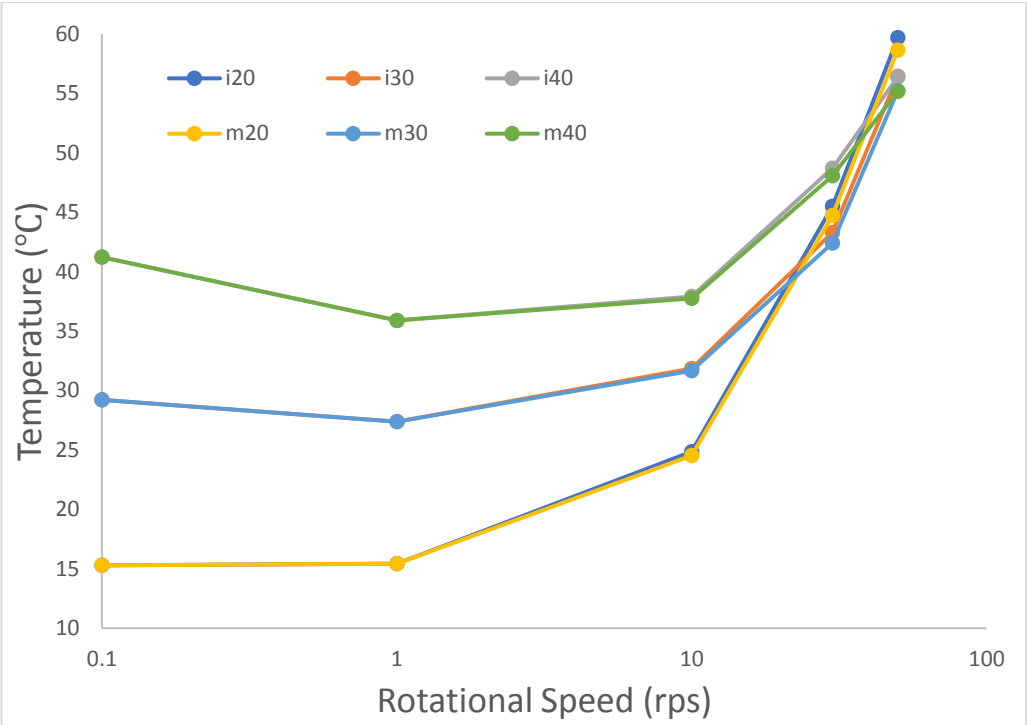

Figure 5 - 7 The estimated sample temperatures (ixx) from the isothermal model and the ones (mxx) from the elaborated model at 20, 30, and 40 °C, plotted as a function of rotational speed.

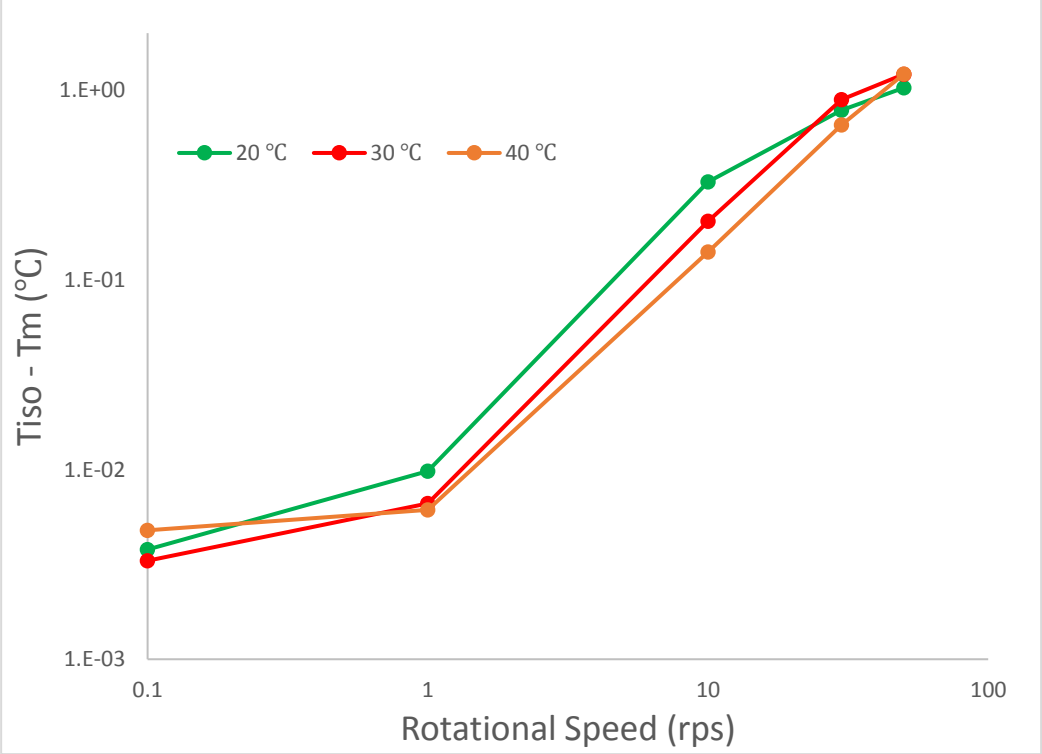

Figure 5 - 8 The temperatures difference (°C) between T_{iso} and Tm at 20, 30, and 40 °C.

Considering the assumption that the fluid is isothermal for the simple thermo-rheometric model, the results obtained are kind of rough. However, even with a rough estimation, the sample temperatures from it are very close to the ones from the elaborated model, with the biggest discrepancy of 1.22 °C. The fact that the results from both models are similar confirms the validity and reliability of the elaborated model.

Besides the estimated sample temperatures, the elaborated model can also be used to estimate the shear rates and the temperatures at the shaft or at the wall, as shown in **Figure 5 - 9** and **Figure 5 -10**. These cannot be obtained by the simple thermo-rheometric model as well as present experimental setup.

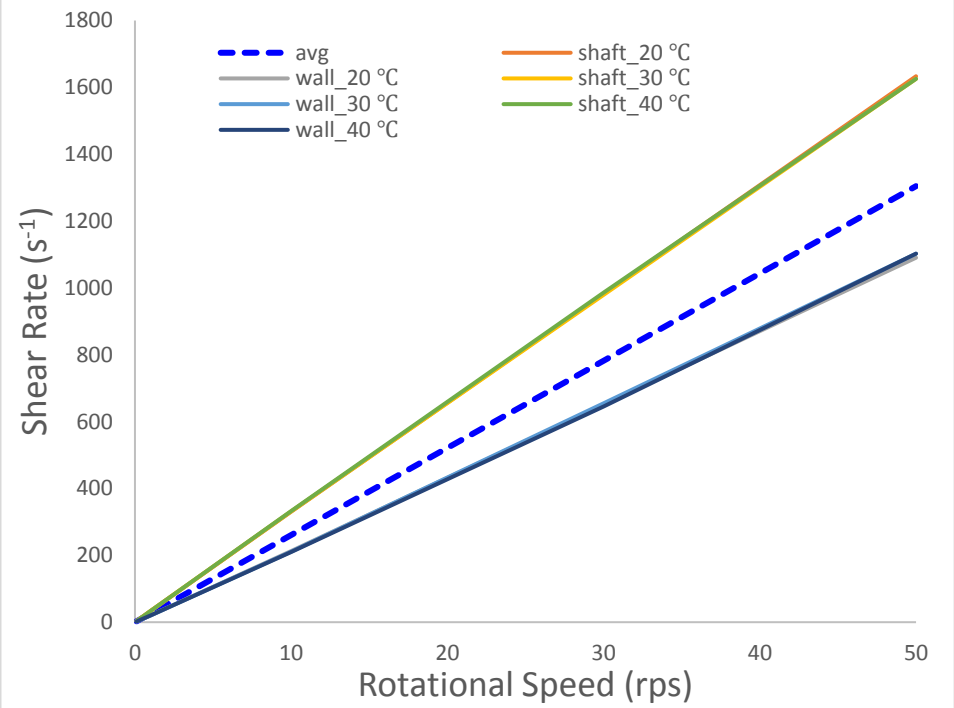

Figure 5 - 9 The shear rates, calculated from the model, at the shaft and at the wall at 20, 30, and 40 °C and the average shear rate calculated from equation (22).

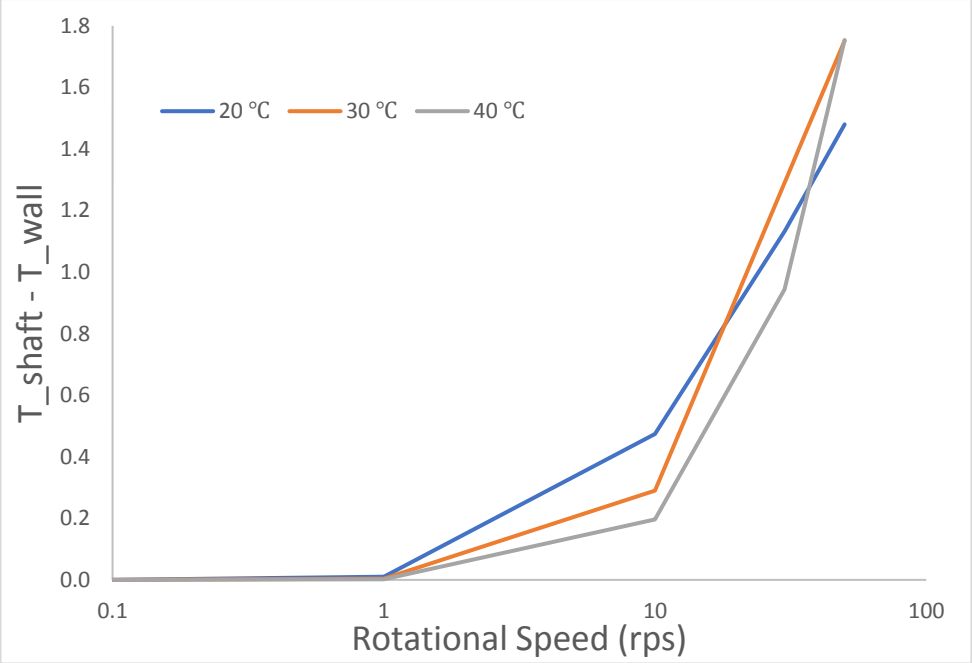

Figure 5 - 10 The temperature differences between at the shaft and at the wall at 20, 30, and 40 °C.

The temperatures estimated from the elaborated model were then compared to those from the experiments, which were summarized in **Table 5 - 3**, **Figure 5 - 11** and **Figure 5 - 12**.

Table 5 - 3 The estimated sample temperatures (°C) from the model and NMR at 20, 30, and 40 °C.

Rotational Speed (rps)	MODEL			NMR		
	20 °C	30 °C	40 °C	20 °C	30 °C	40 °C
0.1	15.29	29.22	41.23	13.58	27.71	39.92
1	15.43	27.38	35.90	14.70	28.45	39.60
10	24.53	31.66	37.77	18.37	30.96	42.00
30	44.72	42.42	48.07	24.77	37.37	51.27
50	58.66	55.23	55.17	29.92	42.26	57.17

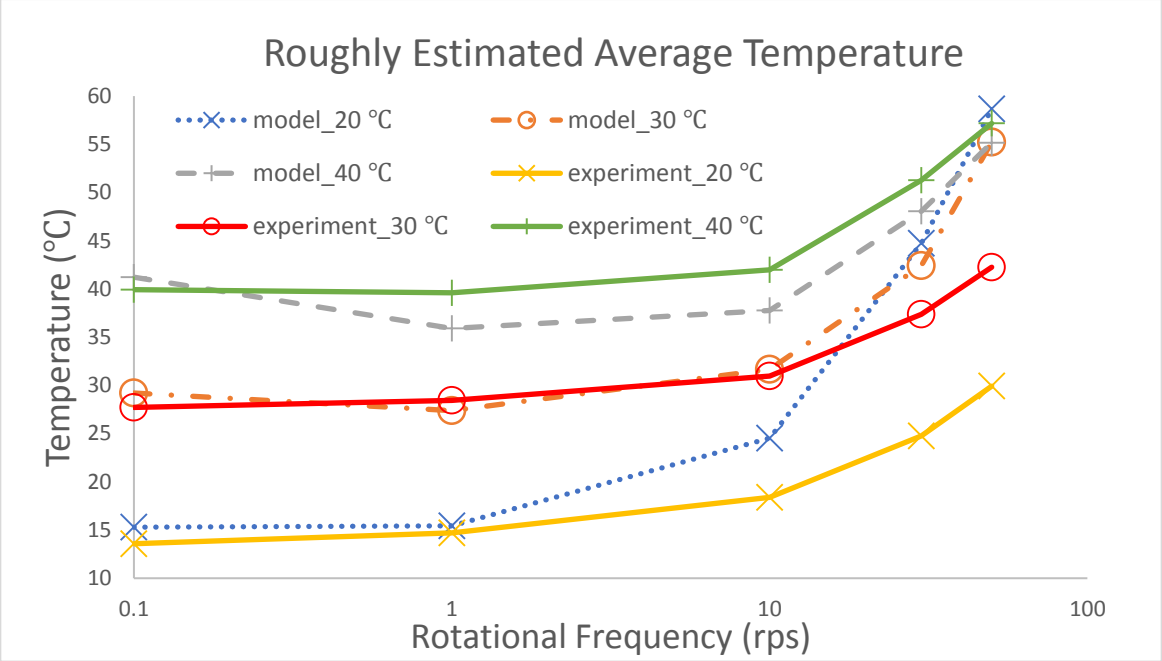

Figure 5 - 11 Model and experimental estimates of average temperature as a function of rotational frequency (0.1, 1, 10, 30, and 50 rps), for the holding temperature examined.

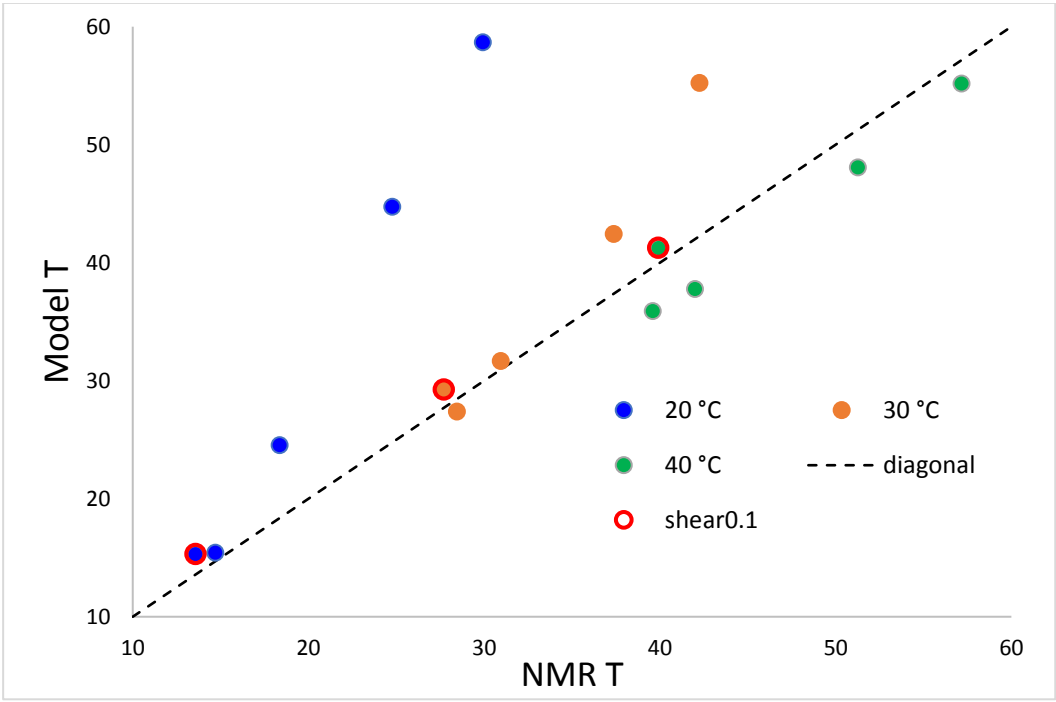

Figure 5 - 12 Model of average temperature as a function of experimental estimates of average temperature, for the holding temperature examined.

The estimated temperatures of the model and experiments are very close to each other for the rotational frequencies of 0.1 and 1 rps. This is significant because the fluid is close to being isothermal. Note that the model does not assume an external fluid temperature. In the isothermal case, the thermal conductivity does not play any significant role. Thus, the model is using the viscosity to determine the temperature. This is a validation for the NMR estimates under those low shear conditions.

At higher rotational speeds, the temperatures calculated from both methods depart from each other. At 40 nominal, the differences are about 4 °C. Within that error, the temperatures calculated from the power by the model follow the temperatures estimated from NMR data.

At 30 and 20 nominal, the differences increase with the shear rates. The sample temperature estimated by the model goes above 55 °C at the nominal Galden temperature holding of 20, 30, and 40 °C, under high shear rate at 50 rps. That is about a 40 °C difference, compared with the highest and lowest shear rates at 20 °C.

The NMR experimental data are more reasonable. The largest temperature difference between the highest and lowest shear rates is about 17 °C, at 40 °C.

From the graph, it's also clear that the trends of the estimated temperatures at 40 °C are consistent. In summary, the estimated temperature of the model is similar to the one of the NMR experiments at 40 °C whereas the temperatures at 20 and 30 °C are deviating.

Two possible reasons for the difference are considered. Firstly, the rheometer may not be carefully calibrated before experiments, which resulted in inaccurate mechanical power recorded. It would noticeably affect the results of the model because the mechanical power is the only parameter measured from the experiments. Secondly, the sample, N1000, was defined as a Newtonian fluid. However, no one could tell if it's still Newtonian fluid

under high shear rates. If it changes to non-Newtonian fluid, the model should be adjusted before using. This would explain the low power at 20 and 30 °C, but would not explain the 'excess' power at 40 °C (**Figure 5 - 6**).

A plot of the ratio of two viscosities was made to try to shed some light on the trend of the differences. First, the viscosity at the shaft was computed from the power measured by the rheometer, using the detailed rheological mathematical model. Then, the viscosity of the N1000 fluid was computed, via the Andrade equation, for the temperature estimated by the T_2 NMR measurements. The ratio of these viscosities was then plotted in **Figure 5 - 13**. The estimated area at the shaft was adjusted from 0.00197 m^2 to 0.00185 m^2, *i.e.* 94%, to place the reference ratio at 0.1 rps and 40 °C at a value of 1.0.

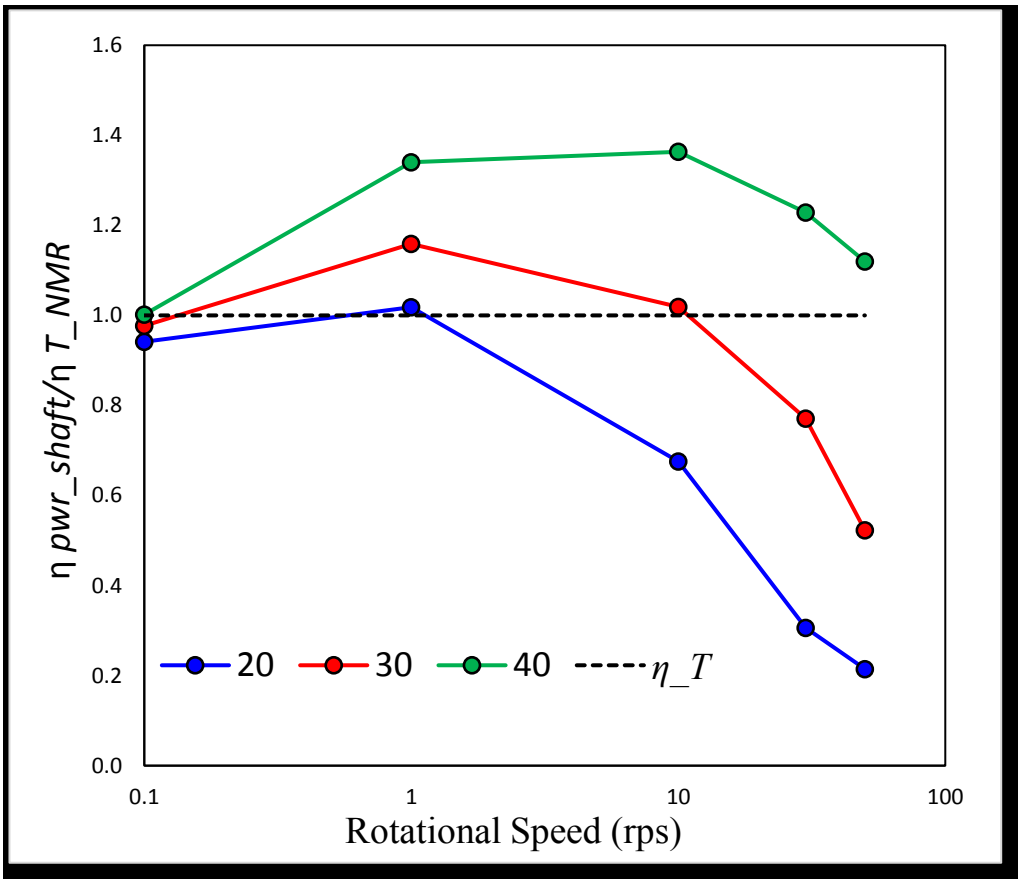

Figure 5 - 13 Ratio of viscosities as a function of rotational speed ***v*** in rps, for the three nominal Galden temperatures. See the text for details.

There is a trend of behavior as the rotational speed and the temperature of the Galden fluid increase. However, the trend is not simple or unidirectional. The ratio increases with the temperature of the Galden. The increase due to temperature becomes generally larger as the shear rate increases. The ratio, at all temperatures, has an initial increase with rotational speed, from 0.1 to 1 or 10 rps. Then the ratio decreases with the increase in shear rate. The decrease is not uniform.

We do not have any solid explanation as to what this general trend means. It needs to be further explored with other fluids, and with an improved design of FOT sensors location in the Galden circulation insert.

CHAPTER 6 CONCLUSION AND FUTURE WORK

The first goal of this work was to investigate the temperature effect on the T_2 relaxation time of a standard Newtonian oil. T_2 was measured for a standard Newtonian oil without shear flow at a range of temperatures. The measurements were conducted in a mini-Couette cell, using a CPMG sequence for the 20 MHz NMR instrument. Two characteristic T_2 values were found to be needed to describe the echo decay. These two T_2 values were ascribed to intra- and inter- molecular interactions of the protons. A mathematical function was then found that successfully described the increase of both T_2 values with temperature. This function also included the temperature dependency of the amplitude ratios of the decay signal.

The second purpose was to use the mathematical function to estimate the temperature from measurements of T_2 as the sample was under shear flow. This would make the T_2 method (measurements + function) an intrinsic thermometer to estimate the temperature of the Newtonian oil in the shear cell. The Rheo-NMR system was used to measure T_2 under three nominal control temperatures and five shear rates. It was found that at high shear rates the values of T_2 increased with respect to the static measurements. Consequently, the temperatures estimated from the function increased as well. This temperature increase was attributed to the viscous heating.

The third purpose was to compare the temperature estimates from the T_2 method with the temperature estimates of the thermo-rheometric model, TRM. Both the T_2 and TRM methods indicated that the temperature of the material increased significantly at high

shear rates. The increase of temperature estimated by both methods was negligible at low shear rates.

However, the extent of the temperature increase estimated for high shear rates was different, depending on the method. As will be discussed in more detail in the following paragraphs, both procedures require further refinement and additional experiments to develop a consistent protocol.

The Cannon 1000 standard Newtonian oil used is described in **Section 3.1**. For the samples under a static environment, both T_{2_1} and T_{2_2} increase when the temperature increases. The temperatures explored ranged from 0 to 40 °C. In this range, the values of T_{2_1} were 1.7 to 4.4 ms, T_{2_2} from 6.4 to 23.0 ms when the shaft was inside the glass tube. The ratio of the amplitude of T_{2_2} over total amplitude, A2/(A2+A1), ranged roughly from 0.3 to 0.6. In this range of temperatures, the functions of T_2 and the amplitude ratio were approximated as 2nd order polynomials of the temperature. Statistical analysis showed that the optimal estimate (minimum variance) of the temperature from the three functions would be obtained with relative weights of 0.183 for A2/(A2+A1), 0.208 for T_{2_1} and 0.609 for T_{2_2}. The standard error of estimation for the temperature would be ± 0.15 °C.

When the shaft was not placed inside the glass tube, the values of T_{2_1} ranged from 1.8 to 4.03 ms, and of T_{2_2} from 6.4 to 22.1 ms. The ratio A2/(A2+A1) remained almost the same as the shaft-in experiments, from 0.3 to 0.6. The optimal estimate of the temperature would be obtained with relative weights of 0.149 for A2/(A2+A1), 0.218 for T_{2_1} and 0.633 for T_{2_2}. The measurements with and without the shaft were close enough to indicate that the shaft had no significant effect on the estimates, other than an increase in the variance, due to the smaller sample volume. The shaft, however, had an effect on the temperature,

and it thus seemed reasonable to choose the shaft-in correlations for predicting temperatures.

The correlations obtained from the shaft-in experiments are more reliable to predict shaft-in temperatures, compared with the ones from the shaft-out experiments. This can be observed from the differences between the predicted sample temperatures and the measured sample temperatures (0.02 - 0.27 °C difference between T_{shaft_in} and T_S, 0.43 – 0.97 °C differences between T_{shaft_out} and T_S). The correlations from the shaft-in experiments were therefore used as the function to estimate the sample temperature under shear conditions.

For the shear experiments, all the parameters were kept the same as the shaft-in experiments in the static experiments. The shaft position was also maintained at 467 mm because the presence of the shaft, which has been discussed in **Section 4.3,** did affect the results. Rheo-NMR experiments were then conducted at rotational speeds of 0.1, 1, 10, 30, and 50 revolutions per second. They correspond to nominal shear rates of 2.609, 26.09, 260.9, 782.7, and 1304.5 s^{-1}. The nominal temperature of the medium was set between 20 and 40 °C. The temperatures were effectively around 14, 28 and 40 °C.

The predictions of a simple thermo-rheometric model (TRM), which estimated the temperature from the power by using the viscosity of N1000, were compared to the predictions of an elaborated TRM (including thermal conductivity) at different shear rates and temperatures. The elaborated TRM was developed to describe the energy generation and transport due to viscous heating of a Newtonian fluid. The estimated temperatures from each method are very close, with only 1.22 °C difference (biggest) at the Galden temperature of 40 °C under 50 rps. The elaborated TRM was thus found to be reliable and consistent with the simple TRM.

The main question of the research was whether the temperature estimates from T_2 data would be comparable to the predictions from the TRM, at different shear rates and temperatures. At low shear rates, when the fluid could be considered isothermal, the deviation was small and could be easily corrected by a linear calibration (**Figure 5 - 12**). However, at higher shear rates the estimated temperatures differ considerably. The differences between the temperature estimated from the TRM and from the NMR T_2, at the Galden temperature of 40 °C, are about 4 °C, regardless of shear rate. At 20 and 30 °C, however, the differences increase with the shear rates. Under the highest shear rate (50 rps), the sample temperature estimated by the model goes above 55 °C at the Galden temperature of 20, 30, and 40 °C. That is about a 40 °C difference, compared with the highest and lowest shear rates at 20 °C. In the estimates using the NMR T_2 data, the largest temperature difference between the highest and lowest shear rates is about 17 °C, at 40 °C. The temperatures estimated from the NMR T_2 measurements seem more reasonable than the ones estimated from the TRM. As indicated in the discussion, a possible reason could be that the 'standard' is only Newtonian under small shear rates and becomes shear-thinning at high shear rates. This would explain the low power at 20 and 30 nominal °C, but would not explain the 'excess' power at 40 °C. More work is needed to understand the differences, including experiments with other Newtonian standards.

From the NMR T_2 experiments, it is clear that the T_2 relaxation times increase with temperature. In order to get a better understanding of the temperature effect on T_2, deeper study on a wider range of temperatures must be done in the future. The application of this intrinsic thermometric method needs further refining as well, yet it offers us for the first time in the field of crystallization of fats and waxes under shear flow, a possibility to have

a close estimate of the real temperature of the actual temperature of the process that we are observing.

For future work, a non-Newtonian fluid or some other more complex fluids, such as a mixture of dodecane and paraffin wax, may be used to run the experiments. By using various fluids, the feasibility and reliability of the model can be tested. Also, the rheometer needs to be carefully calibrated before experiments in the future. The data recorded by the rheometer can be applied to the simple thermo-rheometric model as a rough reference of the sample temperature, if its apparent viscosity is known. However, in crystallizing suspensions the apparent viscosity is not known ‘a priori’ as a function of temperature, shear rate, solid fraction, and particle shape and size distribution. Thus, being able to monitor the temperature of the liquid portion using an intrinsic method is still a very desirable target.

BIBLIOGRAPHY

A. Costa, & G. Macedonio. (2003). Viscous heating in fluids with temperature-dependent viscosity: Implications for magma flows. Nonlinear Processes in Geophysics, 10(6), 545-555.

B J Ackerson. (1990). Shear induced order of hard sphere suspensions. Journal of Physics: Condensed Matter, 2(S), SA389-SA392.

Bagueira de Vasconcelos Azered, Colnago, & Engelsberg. (2000). Quantitative analysis using steady-state free precession nuclear magnetic resonance. Analytical Chemistry, 72(11), 2401-5.

Balci, Metin. (2005). Basic 1H- and 13C-NMR Spectroscopy. London: Elsevier Science.

Bernstein, M., King, Kevin Franklin, & Zhou, Xiaohong Joe. (2004). Handbook of MRI pulse sequences. Amsterdam; Boston: Academic Press.

Bird, R., Stewart, Warren E., & Lightfoot, Edwin N. (2002). Transport phenomena (2nd ed.). New York; Toronto: J. Wiley.

Blaak, R., Auer, S., Frenkel, D., Löwen, H., & Molecular Simulations. (2004). Crystal nucleation of colloidal suspensions under shear. Physical Review Letters, 93(6), 068303.

Britton, M., & Callaghan, P. (2000). NMR VELOCIMETRY STUDY OF THE TEMPERATURE DEPENDENT RHEOLOGY OF BUTTER, SEMISOFT BUTTER AND MARGARINE. Journal of Texture Studies, 31(3), 245-255.

Britton, M., Callaghan, P., Kilfoil, T., Mair, L., & Owens, R. (1998). NMR velocimetry and spectroscopy at microscopic resolution in small rheometric devices. Applied Magnetic Resonance, 15(3), 287-301.

Burton, R. A. (2000). Viscous Heating in Laminar Couette Flow. Heat, Bearings, and Lubrication, Springer New York**:** 12-20.

Callaghan, P. (1993). Principles of nuclear magnetic resonance microscopy. Oxford: Clarendon Press.

Carosio, Bernardes, Andrade, Moraes, Tosin, & Colnago. (2016). Measuring thermal properties of oilseeds using time domain nuclear magnetic resonance spectroscopy. Journal of Food Engineering, 173, 143-149.

Demirel, Y. (2000). Thermodynamic analysis of thermomechanical coupling in Couette flow. International Journal of Heat and Mass Transfer, 43(22), 4205-4212.

Deng, X. (2014). Effect of Temperature on the Wide Angle X-Ray Diffraction of Nanocrystalline Triacylglycerols, Dalhousie University. **Master of Science**.

E. N. Da C. Andrade. (1930). The Viscosity of Liquids. Nature, 125(3148), 309-310.

Farrar, T., & Becker, Edwin D. (1971). Pulse and Fourier transform NMR; introduction to theory and methods. New York: Academic Press.

Feuge, R., Landmann, W., Mitcham, D., & Lovegren, N. (1962). Tempering triglycerides by mechanical working. Journal of the American Oil Chemists' Society, 39(7), 310-313.

Fujii, N. and S. Uyeda (1974). "Thermal Instabilities during Flow of Magma in Volcanic Conduits." Journal of Geophysical Research **79**(23): 3367-3369.

Garbolino, C., Ziegler, G., & Coupland, J. (2000). Ultrasonic determination of the effect of shear on lipid crystallization. Journal of the American Oil Chemists' Society, 77(2), 157-162.

Gavis, J. and R. L. Laurence (1968). "Viscous heating in plane and circular flow between moving surfaces." Industrial & Engineering Chemistry Fundamentals **7**(2): 232-239.

Guthausen, Zimmer, Blümler, & Blümich. (1998). Analysis of Polymer Materials by Surface NMR via the MOUSE. Journal of Magnetic Resonance, 130(1), 1-7.

Guthausen G., Todt H., Burk W., Schmalbein D., Kamlowski A. (2008) Time-Domain NMR in Quality Control: More Advanced Methods. In: Webb G.A. (eds) Modern Magnetic Resonance. Springer, Dordrecht

Hansen, & Yuen. (1996). Potential role played by viscous heating in thermal-chemical convection in the outer core. Geochimica Et Cosmochimica Acta, 60(7), 1113-1123.

Haw, M. D., Poon, W. C. K., & Pusey, P. N. (1998). "Direct Observation of Oscillatory-Shear-Induced Order in Colloidal Suspensions." Physical Review E **57**(6): 6859.

Hetsroni, Mosyak, Pogrebnyak, & Yarin. (2005). Fluid flow in micro-channels. International Journal of Heat and Mass Transfer, 48(10), 1982-1998.

Hornak, J. P. (1997). "The Basics of NMR." from http://www.cis.rit.edu/htbooks/nmr/inside.htm.

Kantzas, A., Bryan, J., Taheri, S. Fundamentals of Fluid Flow in Porous Media. PERM Inc. TIPM LABORATORY.

Kim, B., Beskok, H., & Cagin, A. (2010). Viscous heating in nanoscale shear driven liquid flows. Microfluidics and Nanofluidics, 9(1), 31-40.

Kuang, L. (2016). The method of calculation the oil saturation of the tight oil reservoir. China.

Larsen, Yuen, Smedsmo, & Malevsky. (1997). Generation of fast timescale phenomena in thermo-mechanical processes. Physics of the Earth and Planetary Interiors, 102(3), 213-222.

Li, M. (2011). RHEO-NMR and Synchrotron X-ray diffraction characterization of nanostructure of triglycerides crystallizing from solutions, Dalhousie University.

M. Ronczka, & M. Müller-Petke. (2012). Optimization of CPMG sequences to measure NMR transverse relaxation time T2 in borehole applications. Geoscientific Instrumentation,1(2), 197-208.

Mallock, A. (1888). Determination of the Viscosity of Water. Proceedings of the Royal Society of London, 45, 126-132.

Mallock, A. (1896). Experiments on Fluid Viscosity. Philosophical Transactions of the Royal Society of London. Series A, Containing Papers of a Mathematical or Physical Character, 187, 41-56.

Mazzanti, G., Welch, S. E., Sirota, E. B., Marangoni, A. G., & Idziak, S. H. J. (2005). Crystallization of bulk fats under shear. Soft Materials Structure and Dynamics. N.Y., Marcel Dekker, Inc. Chapter 3.

Mazzanti,G. ;Marangoni, A. ;Idziak, S. (2005). Modeling Phase Transitions During the Crystallization of a Multicomponent Fat Under Shear. Phys. Rev. E, 71, Phys. Rev. E, 2005, Vol.71.

Mazzanti, G. and E. M. Mudge (2008). Development of a rheo-NMR system to study the crystallization of bulk lipids under shear flow. Magnetic Resonance in Food Science, Royal Chemical Society**:** 89-96.

Mazzanti, G., Mudge, E., & Anom, E. (2008). In Situ Rheo-NMR Measurements of Solid Fat Content. Journal of the American Oil Chemists' Society, 85(5), 405-412.

Mossaz, S., Colombet, D., Ledoux, G., & Ayela, F. (2015). Role of the thermal entrance length on the viscous heating in microchannels. Microfluidics and Nanofluidics, 19(6), 1325-1333.

Mudge, E. (2009). Rheo-NMR Measurements of Cocoa Butter Crystallized Under. Crystal Growth and Design, 9(7), Crystal Growth and Design, 2009, Vol.9(7).

Okubo, & Ishiki. (1999). Kinetic Analyses of Colloidal Crystallization in a Sinusoidal Electric Field as Studied by Reflection Spectroscopy. Journal of Colloid and Interface Science, 211(1), 151-159.

Palberg, T., Mönch, Schwarz, & Leiderer. (1995). Grain size control in polycrystalline colloidal solids. The Journal of Chemical Physics, 102(12), 5082-5087.

Pantokratoras, A. (2007). "Classical Plane Couette Flow with Viscous Dissipation and Variable Fluid Properties." Journal of Thermophysics and Heat Transfer **21**(2): 437-442.

Papathanasiou, T. (1998). Explicit Corrections for the Effect of Viscous Heating in Circular Couette Viscometers. International Journal of Thermophysics, 19(1), 71-88.

Peng, Y., Dong, H., & Tang, X. (2010). Noninvasive Temperature Measurement Using MRI Based on T2 Relaxation Time. Bioinformatics and Biomedical Engineering (iCBBE), 2010 4th International Conference on, 1-3.

Rao, M. (2014). Rheology of fluid, semisolid, and solid foods: Principles and applications (Third ed., Food engineering series). New York: Imprint: Springer.

Roberts, G., & European Biophysical Societies Association, issuing body. (2013). Encyclopedia of biophysics. Heidelberg: Springer.

Shaw, H. R. (1969). "Rheology of Basalt in the Melting Range." J Petrology **10**(3): 510-535.

Sun, Z., PANG, M., YU, Y., YANG, P., & YU, W. (2011). "Effect of Superplasticizer on Transverse Relaxation Time Curve of Cement Paste." Kuei Suan Jen Hsueh Pao/ Journal of the Chinese Ceramic Society.

Syrjälä, S. and J. Aho (2007). "Evaluation of the Effect of Viscous Heating in Capillary Rheometry of Polymer Melts." Annual Transactions of the Nordic Rheology Society **15**.

Thomas Elder, L. G. T., Nicole Labbé (2007). "Low-Field, Time-Domain NMR and its Application to Wood Science and Technology." from http://www.swst.org/meetings/AM07/elder.pdf.

Tinsley, F.C., Taicher, G.Z., & Heiman, M.L. (2004). Evaluation of a quantitative magnetic resonance method for mouse whole body composition analysis. Obesity Research, 12(1), 150-160.

Todt, Guthausen, Burk, Schmalbein, & Kamlowski. (2006). Water/moisture and fat analysis by time-domain NMR. Food Chemistry,96(3), 436-440.

Venâncio, Engelsberg, Azeredo, Alem, & Colnago. (2005). Fast and simultaneous measurement of longitudinal and transverse NMR relaxation times in a single continuous wave free precession experiment. Journal of Magnetic Resonance, 173(1), 34-39.

Venâncio, Engelsberg, Azeredo, & Colnago. (2006). Thermal diffusivity and nuclear spin relaxation: A continuous wave free precession NMR study. Journal of Magnetic Resonance,181(1), 29-34.

Wang, F. C., Johson, M. B., Mazzanti, G. (2012). Viscous heating in a mini-Couette cell used in Rheo-XRD and Rheo-NMR research.

White, F. (2006). Viscous fluid flow (3rd ed., McGraw-Hill series in mechanical engineering). New York; Toronto: McGraw-Hill Higher Education.

Whitehead, A., & Russell, Bertrand. (1927). Principia mathematica (2d ed.). Cambridge (Eng.): University Press.

Wright, A., Hartel, R., Narine, S., & Marangoni, A. (2000). The effect of minor components on milk fat crystallization. Journal of the American Oil Chemists' Society, 77(5), 463-475.

Zega, J., & Kobayashi, Riki. (1991). Spin-lattice Relaxation in Normal Alkanes at Elevated Pressures, ProQuest Dissertations and Theses.

APPENDIX

Figure A - 1 is the original graph of the relaxation times and amplitudes measured from the shaft-out experiments. Amplitudes at 40 °C are in the original positions, and they are biased from the trends. Part of the Ampl_2 values decreases at 40 °C which seems to be unreasonable considering the increasing trend of Ampl_2 from low to high temperature. One possibility is that the equipment error occurred while running the experiment. To solve this issue, all the data points from that experiment were enlarged by a specific ratio (1.1). The calibrated graph is shown as **Figure 4 - 7**.

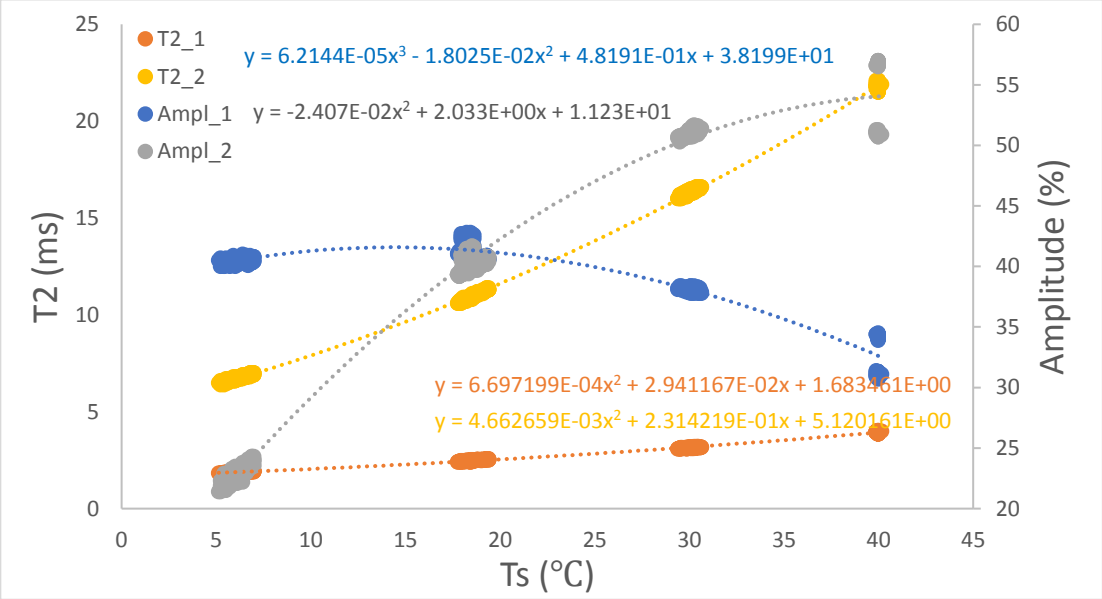

Figure A - 1 The measured T_2 relaxation times and amplitudes* as a function of the sample temperature without the shaft, together with the corresponding trendlines. Ampl_1 and Ampl_2 are the amplitudes of component 1 and 2 at time zero, whereas T_{2_1} and T_{2_2} are the relaxation times of component 1 and 2. (Note: the amplitudes are proportional to the amplitude of the reference that was used to calibrate the NMR)

The following tables, graph, and equations are based on the original data, and they are displayed as reference.

Table A - 1 The values of A1, A2, and A2/(A2+A1) determined from the correlations (without shaft).

T (℃)	T (K)	A1	A2	Ampl_Tot	A2/(A2+A1)
0	273	38.2	11.2	49.4	0.227
5	278	40.2	20.8	61.0	0.341
10	283	41.3	29.2	70.4	0.414
15	288	41.6	36.3	77.9	0.466
20	293	41.1	42.3	83.4	0.507
25	298	40.0	47.0	87.0	0.541
30	303	38.1	50.6	88.7	0.570
35	308	35.6	52.9	88.5	0.597
40	313	32.6	54.0	86.7	0.624
45	318	29.0	54.0	83.0	0.650

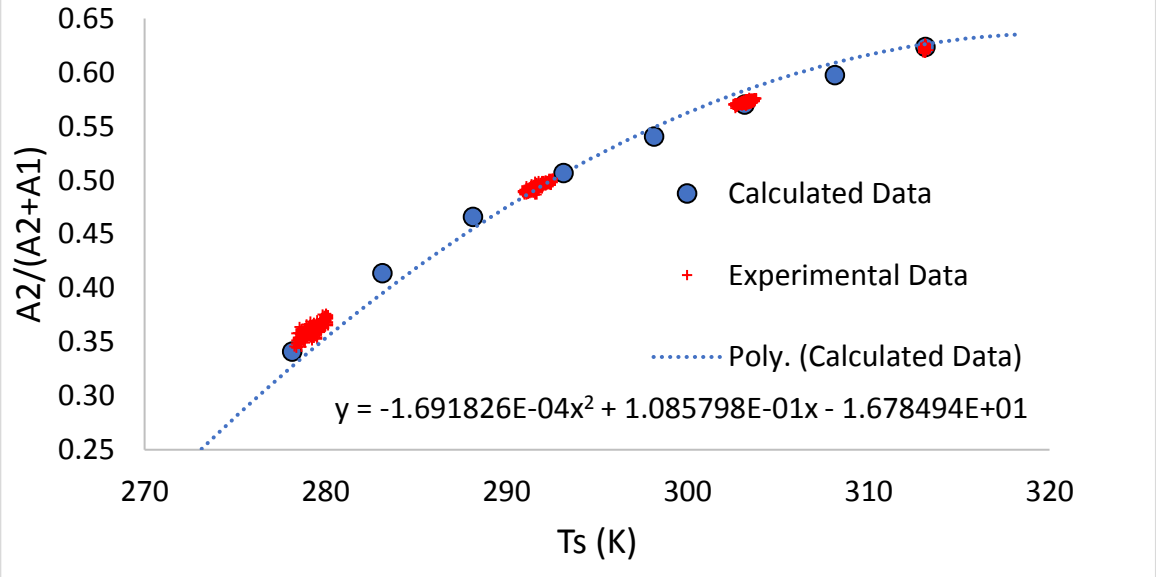

Figure A - 2 The calculated and experimental A2/(A2+A1) as a function of the sample temperature in K (without shaft). The trendline was added to the calculated data and the equation was displayed in the graph.

The correlation equations for T_{2_1}, T_{2_2}, and A2/(A2+A1) are the ones below, and the unit of T_s for T_{2_1} and T_{2_2} is °C, whereas the unit of T_s for A2/(A2+A1) is K.

$$T_{2\_1} = 6.697199 \times 10^{-4} T_s^2 + 2.941167 \times 10^{-2} T_s + 1.683461$$

$$T_{2\_2} = 4.662659 \times 10^{-3} T_s^2 + 2.314219 \times 10^{-1} T_s + 5.120161$$

$$\mathrm{A2}/(\mathrm{A2} + \mathrm{A1}) = -1.691826 \times 10^{-4} T_s^2 + 1.085798 \times 10^{-1} T_s - 16.78494$$

Table A - 2 The calculated values of standard deviation (σ), 1/σ, and weight by using T_{2_1}, T_{2_2}, and A2/(A2+A1) respectively (without shaft).

	T_{2_1}	T_{2_2}	A2/(A2+A1)
standard deviation (σ)	0.594	0.204	1.231
1/σ	1.683	4.893	0.812
Weight	0.228	0.662	0.110